DEVELOPMENT OF HIGH-PERFORMANCE CARBON FIBERS: ACCELERATING PARADIGM SHIFTS

A Dissertation
Presented to
The Academic Faculty

by

Narayan Satish Shirolkar

In Partial Fulfillment
of the Requirements for the Degree
Doctor of Philosophy in the
School of Materials Science and Engineering

Georgia Institute of Technology
December 2021

DEVELOPMENT OF HIGH-PERFORMANCE CARBON FIBERS: ACCELERATING PARADIGM SHIFTS

Approved by:

Dr. Satish Kumar, Advisor
School of Materials Science and Engineering
Georgia Institute of Technology

Dr. Jonathan Colton
School of Mechanical Engineering
Georgia Institute of Technology

Dr. Natalie Stingelin
School of Materials Science and Engineering
Georgia Institute of Technology

Dr. Meisha Shofner
School of Materials Science and Engineering
Georgia Institute of Technology

Dr. Kyriaki Kalaitzidou
School of Mechanical Engineering
Georgia Institute of Technology

Date Approved: August 9, 2021

To my parents

ACKNOWLEDGMENTS

First and foremost, I would like to express my deepest gratitude to my advisor, Dr. Satish Kumar, for inviting me to join his group. I really appreciate his guidance and support over the last five years. I am particularly grateful to him for not only supporting but actively encouraging my extracurricular pursuits with student government and beyond. I have been fortunate to have worked with a fantastic team of researchers in the Kumar group and thank them for the insightful discussions and fun social interactions, specifically Dr. Edward DiLoreto, Dr. Mohammad Kirmani, Dr. Pedro Arias-Monje, Dr. Mingxuan Lu, Dr. Prabhakar Gulgunje, Dr. Kishor Gupta, Dr. Jeffrey Luo, Adam Maffe, Jyotsna Ramachandran. I would also like to acknowledge, Dr. Shruti Venkatram, Dr. Clive Lu, Dr. Huibin Chang, and Dr. Po-Hsiang Wang for training on various equipment. Thanks to Casey Smith and Dr. Jony Bodiuzzaman for accommodating my last-minute characterization requests that helped me put together the final pieces of data in this dissertation.

I would like to thank my dissertation committee - Dr. Natalie Stingelin, Dr. Meisha Shofner, Dr. Kyriaki Kalaitzidou, and Dr. Jonathan Colton – for their time and valuable inputs.

I am glad to have worked with fantastic collaborators across the country. Thanks to Dr. Tom Tsotsis at The Boeing Co., for supporting the hollow carbon fiber research. Dr. Dhriti Nepal and Dr. Andrew Sharits were great hosts to me at AFRL, Dayton, OH and helped with nano-CT characterization of hollow carbon fibers. I thank Dr. Mu-Ping Nieh

and Dr. Kuo-chih Shih for their help with small angle X-Ray studies, Dr. Richard Liang and Dr. Jin Gyu Park for their support in capturing analyzing TEM images of carbon fibers. The synchrotron tomography at Brookhaven National Laboratory was made possible by Dr. Wah-Keat Lee, Dr. Xianghui Xiao, and Dr. Mingyuan Ge, and I am grateful for all their help analyzing these fibers and working with me remotely during the pandemic. A huge thank you to Prachi Patwardhan (Georgia Tech), Dr. Aowabin Rahman (University of Utah), and Dr. Ashley Spear (University of Utah). Without them, the machine learning study would not have been possible. I need to give a shout-out to Dr. James Collins and Dr. Richard Neu (Georgia Tech MPCF), the GTRI machine shop, the GT Invention Studio, and collaborators at University of Southern Mississippi for all their help in hollow carbon fiber composite sample preparation and testing. Finally, I would like to acknowledge the technical staff at the Institute for Electronics and Nanotechnology for training and providing access to state-of-the-art characterization equipment.

Some of the most defining experiences I have had at Georgia Tech have been through my involvement with various student organizations on campus. I am grateful for all the great friendships I have built through the MSE GSAG and GT Student Ambassadors. I would be remiss to not acknowledge the GT Graduate Student Government Association (SGA), an organization that has had an immeasurable contribution in developing me as a leader and helping me figure out my next step after PhD. It has been an absolute honor serving as the graduate student body president and I am grateful to Tech's amazing graduate student body, and all the faculty and administrators that I had a chance to work with in this role. I want to express my heartfelt gratitude to Dean John Stein (SGA advisor) for being an amazing mentor, a great sounding board for my ideas, and helping me become

an effective student leader. I am grateful for the lifelong friendships I have built through SGA – Pooja Juvekar, Will Sealy, Aroua Gharbi, Drew Cox, Troy Batugal, and Venkatesh Muppaneni – individuals who embody *Progress and Service.* I am privileged to call them my friends.

Finally, I thank my friends in Atlanta who have made my Georgia Tech experience fun and exhilarating. Thanks to Nithin, Sang, Saurabh, and Venk for helping me with consulting case-prep. I had an enviable support system in Aditi, Harshit, and Jyotsna, who not only tolerated my incessant blabbering, but also supported me in every way possible over the past 5 years. I thank them for encouraging me to run for SGA president and serving alongside to put together one hell of an event with the Grad Gala. I will forever cherish our times together.

I would also like to thank my family for their constant encouragement. Last but certainly not the least, thanks to my parents, for their affection and encouragement, but most importantly, for helping me realize my potential and inspiring me to reach for the stars. I consider myself extremely privileged to have born to parents with advanced degrees and I am grateful for everything that they have done for me.

TABLE OF CONTENTS

LIST OF TABLES

LIST OF FIGURES

SUMMARY

This work details the development of three technological pathways to accelerate paradigm shifts in the way carbon fibers are developed and manufactured. The first two, viz. hollow carbon fibers and small diameter carbon fibers, provide a comprehensive understanding of the process, structure, and property relationship for these continuous carbon fibers. The third pathway provides insights into the challenges and opportunities to employ machine learning models to predict carbon fiber properties by leveraging experimental data and accelerate the improvement in tensile properties in a cost-efficient manner.

Multifilament continuous hollow carbon fiber tows with a honeycomb cross-section have been produced using a gel-spun bicomponent islands-in-a-sea precursor with polyacrylonitrile (PAN) as the sea component and polymethylmethacrylate (PMMA) as the sacrificial island component. Over 80% improvement in tensile strength has been achieved for these fibers compared to the previously reported batch processed hollow carbon fibers, along with a manufacturing scale up from single filament to 740 filament tow. The effect of precursor and carbon fiber manufacturing parameters on the structure and tensile properties of the hollow carbon fibers has been studied. Furthermore, mechanical properties of hollow carbon fiber-epoxy composites have been tested and compared with commercial aerospace grade carbon fiber composites. The effect of adhesion between the fiber and epoxy matrix, alignment of fibers in the composite along the testing direction, and various testing environments, on the composite mechanical properties has been explored. The properties of hollow carbon fibers and their composites

show great promise to replace conventional aerospace grade carbon fibers in the foreseeable future.

Continuous multifilament carbon fiber tows with 2-3μm fiber diameter have been developed from a PAN (island) - PMMA (sea) bicomponent precursor. These small diameter carbon fibers have tensile strength as high as 5.1 GPa and tensile modulus as high as 434 GPa in different trials. The size of the defects in these fibers is estimated to be in the range of 35-70 nm. The role of smaller diameter in improving the tensile properties of these fibers is explored and the nano scale defects in these fibers have been characterized.

Finally, the efficacy of four supervised machine learning techniques, in establishing a mathematical relationship to model the continuous stabilization and carbonization process and predicting the tensile strength and modulus of the fibers, based on the manufacturing process parameters, has been investigated. The data set consisted of 600 data points with 31 features each. The results indicate that machine learning can be used to approximate the underlying function describing the effect of the manufacturing process parameters on the carbon fiber tensile properties

This thesis develops a comprehensive understanding of the three technologies that can each accelerate the development high performance structural carbon fibers. Pursuing these studies separately or in conjunction with each other will likely bring about a paradigm shift in the way high performance carbon fibers and composites are developed.

CHAPTER 1. INTRODUCTION

Polyacrylonitrile (PAN) based carbon fibers are used in structural applications owing to their high tensile strength (3-7 GPa) and tensile modulus (230- 600 GPa). These applications include aerospace, sporting goods, energy harvesting (e.g. wind turbines), and automotive, to name a few. However, in the past three decades, the improvement in the carbon fiber tensile properties has been incremental. The commercially used high strength carbon fibers today, such as IM7 (tensile strength: 5.5 GPa, tensile modulus: 276 GPa) by Hexcel [1] and T800 (Tensile strength: 5.9 GPa, Tensile Modulus: 294 GPa) by Toray, were first produced more than three decades ago [2]. The recently developed T1100G carbon fiber has a tensile strength of 7 GPa and tensile modulus of 324 GPa [3], although, the strength is less than 10% of the theoretical strength of carbon fibers (~100 GPa) [4, 5] and the modulus is ~33% of the theoretical value for graphite (1060 GPa) [6]. There is room to further improve the tensile properties of carbon fibers.

1.1 Accelerated development of high-performance structural carbon fibers: why does it matter?

The aerospace industry was one of the early adopters of carbon fibers and today, carbon fibers are prevalent in lightweight structural components in aircrafts and space vehicles. Carbon fiber composites make up to 50% of the weight of modern aircrafts such as Boeing 787 and Airbus A350 [7, 8]. Every kilogram of jet fuel burnt contributes to 3.16 kg of carbon dioxide (CO_2) [9]. At 1 billion tons of CO_2/year, the aviation industry today is responsible for 3% of global CO_2 emissions. The United Nations' Sustainable

Development Goals (SDG) have set a target to cut down global emissions by 50% from the 2010 levels by 2030 and achieve net zero emissions by 2050, to reverse the global warming trends [10]. For the aviation industry, this would mean cutting down emissions by 500 Mt by 2030. One of the ways to reduce carbon emissions would be to increase fuel efficiency in terms of payload, by making lighter and stronger aircraft structures that can carry the same payload. In other words, less fuel would be required to carry the same weight of passengers or freight. To put it in perspective, let us assume an improvement in carbon fiber tensile modulus by 40%. Assuming 60% fibers by volume in composites, this would result in a composite modulus improvement of 24%. For an aircraft with 50% carbon fiber composites by weight, this would mean a net increase of 12% in the payload capacity. In other words, ~10% less fuel would be required to carry the same payload as before. Assuming that all aircrafts in the future are made up of at least 50% carbon fiber composites by weight, this would reduce global aviation emissions by ~10% or 100M tons. We acknowledge that reducing aircraft structural weight alone will not achieve net zero carbon emissions until sustainable alternatives to jet fuel are used for propulsion. However, it can certainly help significantly reduce these emissions in the near future. Therefore, improving tensile properties of carbon fibers could have major implications in shaping the future of flight.

Carbon fiber manufacturing is a cost and time intensive process. Extensive adoption of carbon fibers in other high volume structural applications (e.g. automotive) remains cost prohibitive. Therefore, accelerating the development of high-performance structural carbon fibers while reducing the cost of development is of great interest. To achieve these

goals, it is important to understand the fiber manufacturing process which is described in the following section.

1.2 Carbon fiber manufacturing

This section focuses on the different steps involved in the carbon fiber manufacturing process, from the development of precursor fibers to carbon fiber manufacturing via continuous stabilization and carbonization.

1.2.1 Polyacrylonitrile

PAN is a synthetic, semi-crystalline polymer that is predominantly used as a precursor in carbon fibers manufactured worldwide [11]. Figure 1.1 shows the chemical structure of PAN [12]. Although it is a thermoplastic, unlike most of the thermoplastic polymers, it degrades before melting unless heated at a very high rate [13]. PAN fibers were first spun in the 1940s when DuPont discovered the use of dimethyl formamide (DMF) as a possible solvent. Over the next 10 or so years, a wide range of organic solvents were found to be potentially useful for PAN fiber spinning. Some of the early reports can be found in the work published by Houtz et al. in the 1950s [2, 14]. PAN fibers were commercialized under the name “Orlon” by DuPont in 1950. The theoretical carbon yield of PAN is 68% but the experimental carbon yield is 50-55% [2, 15]. The continuous carbon backbone and the placement of the nitrile group in PAN is favorable for the cyclization reaction during stabilization and ultimately to produce continuous high-performance carbon fibers. This will be discussed in detail in the later section.

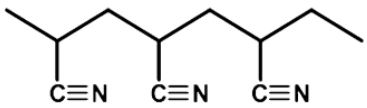

Figure 1.1 Chemical Structure of PAN [12]

Acrylonitrile is made from propylene and ammonia, and therefore, the cost of propylene dictates the production cost of PAN. The chemicals used make up to 45% of the PAN production costs [2].

As stated earlier, PAN is the predominantly used precursor for making carbon fibers. However, the use of homopolymer PAN for commercial production of high-performance carbon fibers has not been reported so far. The oxidation stage of carbon fiber production involves sudden and rapid evolution of heat and is difficult to control. This rapid evolution of heat can cause chain scission and therefore create defects in the resultant carbon fiber, resulting in poor tensile properties of the carbon fibers [16]. This exothermic reaction can be controlled by the use of comonomers such as itaconic acid (IA), methacrylic acid (MAA), methacrylate (MA), vinyl esters etc. The effect of comonomers will be further discussed in later section.

1.2.2 PAN fiber spinning

Broadly speaking, there are two main ways of fiber spinning viz. melt spinning, and solution spinning. Solution spinning can be further classified as wet spinning, dry-jet wet spinning, dry spinning, electrospinning, and gel spinning [17-20]. Due to the difficulty in melting PAN under normal conditions, melt spinning is not commercially used to spin

PAN fibers. There are reports of plasticized PAN being melt-spun but this method is yet to become commercially feasible [13, 18]. Wet spinning is the widely used spinning process for PAN fibers, but dry-jet wet spinning has also been of interest. It is hypothesized that higher orientation of molecular chains is achieved due to the air gap between the spinneret and the coagulation bath, prior to coagulation, in the dry-jet wet spinning process [2]. Schematic diagram of the dry-jet wet spinning process is shown in Figure 1.2 [21]. The polymer concentration used in the dope depends on the molecular weight of the polymer as well as the desired viscosity of the dope. Solvents such as DMF, dimethylsulfoxide (DMSO), dimethylacetamide (DMAc) have been used in solution spinning of PAN fibers.

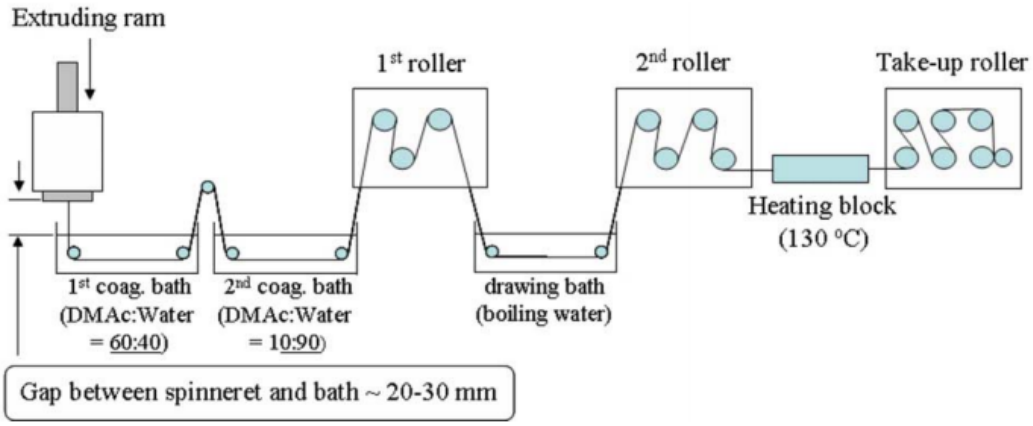

Figure 1.2 Schematic diagram of the typical dry-jet wet spinning process [24]

Gel spinning of ultra-high molecular weight polyethylene (UHMWPE) fibers was first reported by Smith et al. in 1980 [17]. It was reported that gel spinning can lead to high strength fibers. The formation of small crystals in the solution and higher level of entanglements leads to a physically cross-linked "gel" structure upon coagulation. There is a reduction in the number of molecular chain ends per unit length when an ultra-high molecular weight polymer is used. Chain end is a site for a defect, which ultimately limits the tensile strength of the carbon fibers [22]. However, due to the higher level of

entanglements, a lower concentration of the dope, as compared to conventional solution spinning, has to be used in order to spin these fibers. This process requires more solvent and hence is more expensive than conventional solution spinning. At the same time, higher orientation, reduction in number of defects and the subsequent improvement in carbon fiber properties using gel spun PAN fibers can outweigh the higher costs associated with the solvents. Gel spinning is similar to dry-jet wet spinning. A high molecular weight, low concentration polymer solution is extruded through a spinneret in air, followed by coagulation in either a non-solvent or solvent/non-solvent coagulation bath. The as-spun fiber spools may be stored in the non-solvent bath until they are used for further drawing, depending on the polymer solution and spinning conditions. The as-spun fibers are drawn in either a single stage hot drawing or a multi-stage process with cold drawing followed by hot drawing.

Different kinds of fiber geometries can be obtained. Depending on the application, bicomponent fibers with different geometries can be spun. Bicomponent geometries are particularly useful in producing multifunctional fibers combining properties of two different materials. Earlier reports on bicomponent fibers are found for melt spinning [23-25]. However, more recently, bicomponent fibers have been spun using solution spinning as well. For example, bicomponent fibers with a sheath-core geometry (Figure 1.3b) were produced by Chien et al. [26]. The sheath component was PAN while PAN-carbon nanotubes (CNTs) constituted the core component. Using this geometry, fibers with enhanced thermal and electrical conductivities were produced. In another study, Chae et al. [27] produced PAN and PAN/CNT based carbon fibers with a diameter as small as 1 μm. This was facilitated by the use of an islands-in-a-sea bicomponent geometry (Figure

1.3 c), where polymethylmethacrylate (PMMA) was used as the sacrificial "sea" component and the PAN or PAN/CNT formed the islands. PMMA leaves no carbon residue upon degrading [28] and therefore is sacrificed during the stabilization and carbonization process, leaving behind the small diameter PAN or PAN/CNT based carbon fibers. In another work, bicomponent precursor fibers, with a PAN sea and PMMA islands were formed [29]. The PMMA was sacrificed during carbonization to produce a hollow carbon fiber with a honeycomb cross section. This will be further discussed in the subsequent chapter. Some representative bicomponent fiber geometries are shown in Figure 1.3[30].

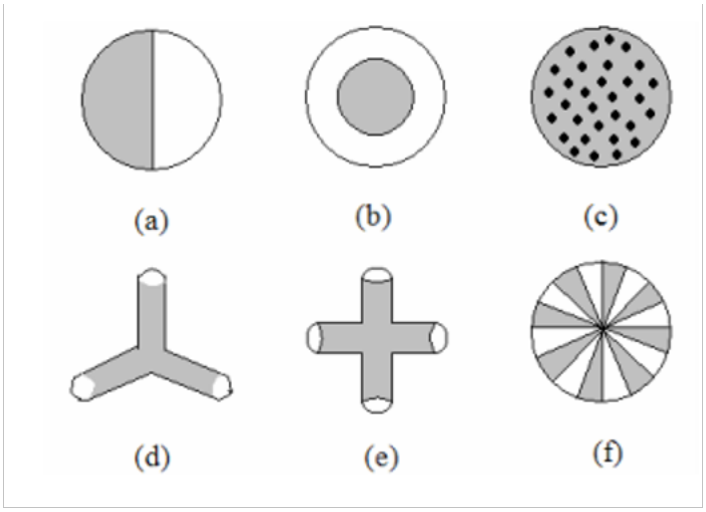

Figure 1.3 Different geometries for bicomponent fibers (a) side by side, (b) core-sheath (c) islands-in-a-sea, (d) tipped trilobal, (e) tipped cross, and (f) segmented pie [29]

Using a single component, for example PAN, alternative geometries such as a film with near rectangular cross-sectional shape can be extruded using solution spinning. Polymeric films are generally produced using blowing [31-33], melt processing [18], casting [34-38], electrospinning [39-41]etc. There are few reports of polymer solutions being extruded through a rectangular slit and then subjected to roll-to-roll processing in a

manner similar to solution spun fiber processing [42]. However, the roll-to-roll film processing method seems to be used more often while processing polymer melts.

1.2.3 Carbon fibers – history of development and state of the art

Carbon fibers were first produced from ordinary cotton threads by Thomas Edison in 1879 [43]. These carbon fibers were used as the filament in the first incandescent lamp. Carbon fiber research did not pick up pace until the 1950s when Houtz et al. produced oxidized PAN fibers [2, 14]. These fibers upon burning in a Bunsen burner flame lost ~30% of its weight but did not volatilize. At that time, it was not understood that the PAN fibers had carbonized under the flame. In 1960, Roger Bacon reported graphite whiskers with a tensile strength of 20 GPa and tensile modulus of 700 GPa [44]. These whiskers were grown in a dc arc under high pressure (92 atm) at a temperature of 3900 °K. In 1961, Shindo et al. produced the first PAN based carbon fiber at the Industrial Research Institute in Osaka [45]. Since then carbon fibers have emerged as a high performance material with unique combination of mechanical, thermal and electrical properties [6, 46].

Carbon fibers can be produced from a range of precursors including PAN, mesophase pitch, cellulose etc. PAN and pitch are the mainly used precursors today. Almost 90% of the carbon fibers commercially produced carbon fibers are made from a PAN precursor, since the chemical structure of PAN, with a continuous carbon backbone and pendant nitrile groups, yield high strength and intermediate modulus carbon fibers. While pitch based carbon fibers can yield a tensile modulus as high as 900 GPa, which is almost 90% of the theoretical value, the tensile strength values are low at ~ 3 GPa. PAN based carbon fibers on the other hand can yield a good combination of tensile strength (3-

7 GPa) and tensile modulus (230 – 600 GPa). However, the higher tensile modulus carbon fibers (400 - 600 GPa) have a tensile strength lower than 4 GPa [6, 46]. The following section focuses on the carbon fiber manufacturing process via stabilization and carbonization of the PAN precursor.

1.2.4 Stabilization and carbonization of the PAN precursor

Production of carbon fibers from PAN precursors involves two main steps: (i) Stabilization at 200 – 300 °C and (ii) carbonization at 500 – 2000 °C. The stabilization step involves oxidation of the PAN precursor, cyclization, and crosslinking to form a stabilized ladder polymer. The density of the fiber increases during this process. The stabilization of PAN is carried out in air. As stated earlier, the presence of comonomers such as IA [47-50] , MA [51-53], MAA [49, 54-56] etc. aids the stabilization process by preventing localized heating of the polymer as well as broadening the temperature range over which oxidation takes place. This is believed to prevent chain scission that occurs in homopolymer PAN due to the sudden and rapid exothermic reaction. After decades of study, the exact mechanism of the stabilization process is still not known. In general, it is accepted that the following four reactions take place: cyclization, dehydrogenation, oxidation, and crosslinking. As the stabilization reaction proceeds, a color change from white to golden brown to black is observed in the PAN fibers. The cyclization can be distinguished from the rest of the reactions by running a sample in a differential scanning calorimeter (DSC) under a non-oxidative atmosphere. The generally accepted mechanism of PAN stabilization and carbonization is shown in Figure 1.4 [57]. Tension is applied during stabilization. During the oxidation process, oxygen diffusion plays an important

role. Ideally, it is desired that the oxygen diffusion throughout the fiber cross-section be uniform. However, in reality the outer part of the cross section is oxidized first and forms a barrier slowing down further oxygen diffusion. This causes formation of a skin-core structure in the fiber, which is a source of heterogeneity in the fiber cross-section. It is thus important to carefully control the stabilization temperature, as well as the residence time and tension in the fiber. It has been observed that the depth of the skin in the skin-core structure can be as high as ~ 1 μm. If a smaller diameter precursor was stabilized, the oxygen diffusion through the fiber would have a lower diffusion gradient, which would lead to a more uniform microstructure in the resultant carbon fiber. On the other hand, to achieve uniform heating of the fiber during stabilization, alternative approaches have been suggested. One such approach involves the use of PAN/CNT precursor and heating of these fibers by applying an electric current [58]. Other routes such as microwave heating [59] and plasma-assisted thermal treatment [60-62] are being explored but are yet to be commercialized.

The carbonization step involves dehydrogenation and denitrogenation as shown in Figure 1.4. The hydrogen and nitrogen are usually removed in the form of HCN, H_2, N_2, and NH_3. The oxygen is removed in the form of CO and to some extent as H_2O and CO_2 [2]. Carbonization is usually done in nitrogen atmosphere. There are two temperature ranges at which carbonization is carried out: the low temperature carbonization is carried out at 500-800 °C, and the high temperature carbonization is carried out above 1000 °C. The desired tensile properties of the carbon fiber dictate the choice of temperature for high temperature carbonization. Improvement in tensile strength is achieved by carbonizing at 1300-1500 °C. In order to achieve a very high tensile modulus, carbonization temperature

is usually greater than 2000 °C. The degree of graphitization increases beyond 2000 °C and therefore yields a higher modulus [63]. It is important to note that the fibers are under tension during stabilization and carbonization and the applied tension plays an important role in the tensile modulus of the resultant carbon fiber. The tensile strength is limited by the size and number of defects that are present in the precursor or the ones that are introduced during the stabilization and carbonization process.

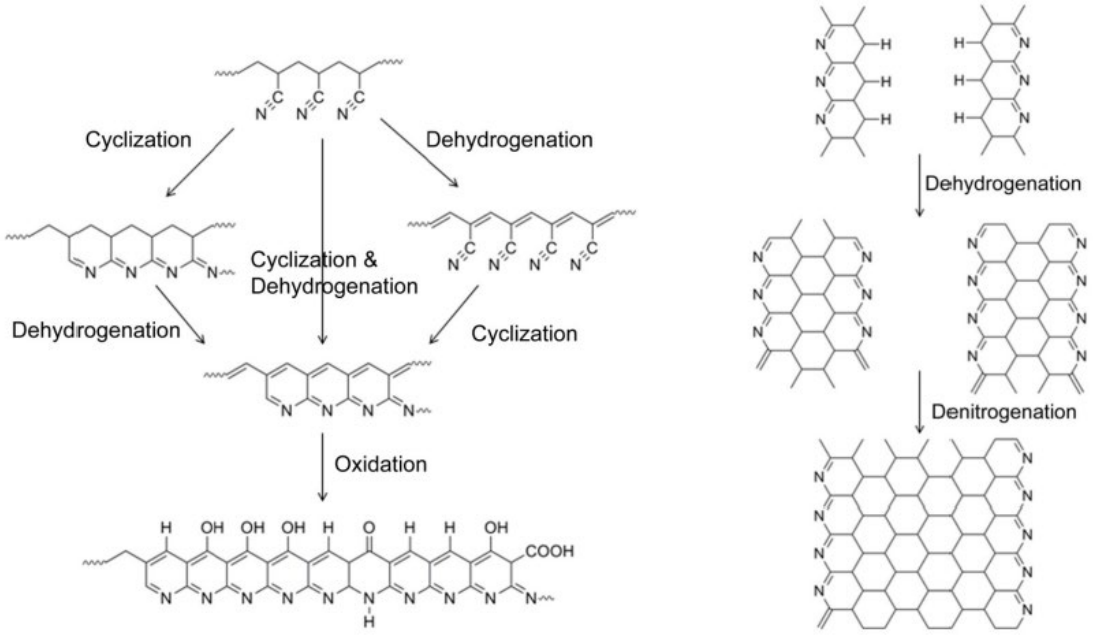

Figure 1.4 Schematic of PAN stabilization (left) and carbonization (right) [4]

1.2.5 Surface treatment and sizing

Carbon fibers with a combination of high tensile strength and modulus cannot just be used by themselves in real life applications and are thus incorporated in a matrix material to form composites. If the adhesion between the fibers and the polymer matrix is not strong, the load transfer from the fibers to the matrix will not be effective. For this purpose, carbon fibers are surface treated and sized before they are used in composite manufacturing.

Oxidative surface treatments involve the passage of carbon fibers through an acidic bath e.g. HNO_3 while an electric current is applied. This is known as anodic oxidation. The surface of the carbon fibers is treated with oxygen, and to some extent, nitrogen. This prepares the surface of the fibers to be treated with a sizing agent. The fibers are washed and dried after surface treatment to remove any unwanted ions from the carbon fiber surface. The fibers are then sized using a sizing agent which can be applied using a polymer solution, electrodeposition of a polymer, electropolymerization etc. The sizing agent is known to aid wetting out the fibers in resin matrices, and increase the ease of handling the fibers during subsequent processing [2]. Since the sizing agent is an important factor in the interphase between the fiber and the matrix, it is necessary to optimize the intake of sizing agent by the fibers.

1.3 Thesis outline

This thesis aims to provide detailed insights into two realms of carbon fiber development. The first explores the development of high strength and high modulus carbon fibers using bicomponent precursors. The second explores the use of machine learning techniques to understand the effect of manufacturing process parameters and predict carbon fiber mechanical properties in a cost and time effective manner.

CHAPTER 2 details the development of continuous, multichannel, hollow carbon fibers with a high modulus from a PAN:PMMA bicomponent precursor. The effect of precursor and carbon fiber manufacturing parameters on the structure and tensile properties of the hollow carbon fibers has been studied. CHAPTER 3 describes the manufacturing of hollow carbon fiber composites with an epoxy matrix and the mechanical performance of these

composites compared to commercial aerospace grade carbon fiber composites. The development of 2-3μm diameter continuous carbon fibers from a PMMA:PAN bicomponent precursor is detailed in CHAPTER 4. The role of smaller diameter in improving the tensile properties of these fibers is explored and the nano scale defects in these fibers have been characterized.

CHAPTER 5 describes an investigation into the efficacy of supervised machine learning techniques in establishing a mathematical relationship to model the continuous stabilization and carbonization process and prediction of the tensile strength and modulus of the fibers based on the manufacturing process parameters.

In CHAPTER 6, the key takeaways of this thesis are summarized, and recommendations are provided to accelerate the development of carbon fibers.

CHAPTER 2. MULTICHANNEL HOLLOW CARBON FIBERS: PROCESSING, STRUCTURE, AND PORPERTIES

This chapter is adapted from a publication in Carbon.

Shirolkar et al., *Multichannel hollow carbon fibers: Processing, structure, and properties.* Carbon, 174 (2021): 730-740.

2.1 Background

As discussed in CHAPTER 1, the full extent of potential weight savings using carbon fiber composites is yet to be realized. One could take multiple different approaches to further improve the specific tensile properties of the composites. One approach is the use of stronger nano-fillers such as carbon nanotubes (CNTs), boron nitride nanotubes etc. in the fibers to improve their tensile properties [64, 65]. While CNTs have a tensile strength and modulus values closer to the theoretical values (~70 GPa and ~1000 GPa respectively), these are not translated to larger enough length scales to be used in place of carbon fibers. At the same time effective load transfer between the polymer-CNT interface continues to be a challenge [66, 67]. This along with the significantly higher production costs compared to carbon fibers currently limit the applications of CNT based composites. An alternative to this is to achieve structural enhancement in carbon fibers through the use of alternative geometries.

The process of making a continuous, multicellular, hollow carbon fibers was patented by Tsotsis et al. in 2012 [68]. The development of hollow carbon fibers with a

honeycomb structure from a gel-spun bicomponent PAN-PMMA precursor with an islands-in-a-sea geometry has been reported earlier [29]. The specific tensile modulus reported for these hollow carbon fibers (~210 N/tex) was up to 30% higher than that of IM7 carbon fibers (155 N/tex). The higher tensile modulus was attributed to the increased molecular orientation at the outer surface as well as the additional surface of the hollow channels. Raman spectra of these fibers indicated a higher level of graphitic ordering near the hollow channels and the fiber surface, which resulted in a higher modulus. However, the tensile strength of these fibers was 1.6 GPa, significantly lower than that of IM7 fibers (5.6 GPa). These hollow carbon fibers were batch processed. The bicomponent precursor fiber was first stabilized in a batch furnace followed by batch carbonization. Tension was applied during stabilization and carbonization by suspending weights from either ends of the fibers. The strain therefore could not be controlled during stabilization and carbonization. Continuous processing of these hollow carbon fibers can overcome this limitation and improve their tensile strength.

The schematic in Figure 2.1 shows the potential weight savings in composites manufactured using of low-density carbon fibers. A 20% reduction in composite density, from 1.55 g/cm^3 to 1.19 g/cm^3, could lead to significant fuel and costs savings for the aerospace industry. To put it into perspective, this could translate to over 20,000 lb weight reduction for the Boeing 787 Dreamliner. However, the tensile properties of the hollow carbon fibers need to be higher than conventional carbon fibers to realize the weight savings in composites without reducing their load-bearing capabilities. In this chapter, we report over 80% improvement in the tensile strength of hollow carbon fibers, from 1.6 GPa to up to 3.0 GPa, with their tensile modulus in the range of 202-234 GPa. In addition,

multifilament continuous hollow carbon tows have been produced successfully with consistent tensile properties over different trials while maintaining microstructural attributes. Based on the tensile properties, the size of strength limiting defects present in the hollow carbon fibers has been calculated.

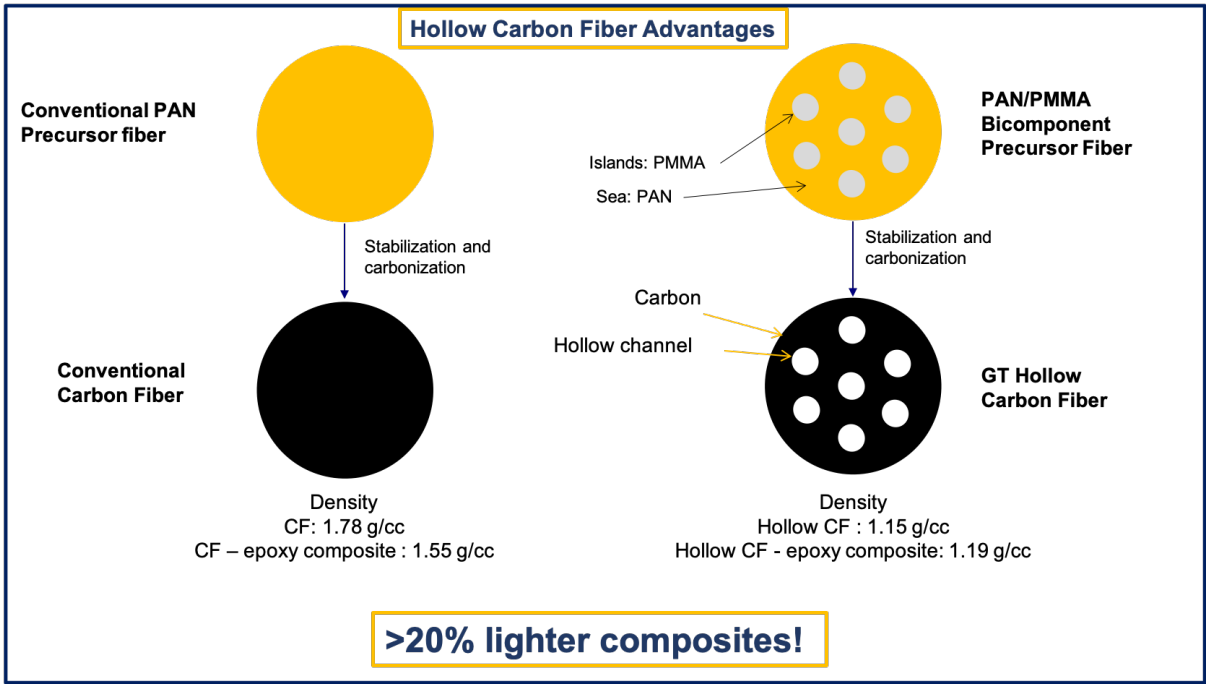

Figure 2.1 Comparison of the hollow carbon fiber manufacturing process compared to conventional solid carbon fibers. The solid carbon fiber used for comparison is IM7 with a density of 1.78 g/cm3. The hollow carbon fiber density is calculated assuming 30% hollow fraction in the carbon fiber cross-section. The density of the hollow carbon fiber can be controlled by controlling the size of the hollow channels. The composite density is calculated using epoxy density of 1.21 g/cm^3 and assuming 60% volume fiber loading. It is important to note that the tensile properties of the hollow carbon fibers need to be higher than that of solid carbon fibers to realize the target weight savings in composite materials while maintaining their load bearing capabilities.

2.2 Materials

Polyacrylonitrile-co-methacrylic acid (PAN-co-MAA) (96:4 by molecular weight) with a viscosity average molecular weight of 247,000 g/mol was obtained from Japan

Exlan Co. Ltd, Japan. Poly (methyl methacrylate) (PMMA) with a viscosity average molecular weight of 350,000 g/mol was obtained from Sigma Aldrich. Dimethylacetamide (DMAc) was used as the solvent for both PAN and PMMA polymers, and was obtained from Sigma Aldrich. Methanol was obtained from VWR. Spin finish SF-LUROL CF-14676 from Goulston Technologies, North Carolina and sizing EP834 from Michelman Inc, Ohio was used. EPON Resin 862, and EPIKURE curing agent was obtained from Miller-Stephenson.

2.3 Fiber Processing

Bi-component fiber spinning system supplied by Hills Inc., Melbourne, FL, was used for the manufacture of precursor fibers. Fiber spinning equipment consisted of two reservoirs [65], one for the PAN solution to be fed as the sea component, and the other for the PMMA solution to be fed as the island component. The solids content for the PAN solution was in the range of 14-15 g/100 mL DMAc, and the solids content for the PMMA solution was in the range of 38-40 g/100 mL DMAc for different trials. Gel spinning of fibers was carried out using 20-hole and 74-hole spinnerets in different trials, with each hole having a diameter of 200 μm. The air gap between the spinneret and the coagulation bath was 19 mm. Two coagulation baths were used for gelation of the spun filaments, with the first bath containing 80/20 methanol/DMAc, followed by a second bath of 100 % methanol, both maintained at room temperature. The as-spun fiber tows were collected at a spin draw ratio (SDR) of 2.3. The as-spun fiber spools were drawn using a multistage drawing process depicted elsewhere (Figure A.1) [65], and the spin finish was applied during the process. Continuous stabilization and carbonization line (Figure A.2) built by

Harper International, Buffalo, NY, was used to stabilize and carbonize the precursor. Stabilization was carried out at temperatures between 180-250 ºC and carbonization temperature was as high as 1450 ºC. Stabilization and carbonization were carried out while maintaining the fiber tow under tension. In trials T3, T4, and T5, the hollow carbon fiber tow was surface treated using an electrolytic bath of nitric acid, and sized using an aqueous solution of the sizing agent. Solution preparation, spinning, drawing, and carbonization facilities are all housed in a class 1000 cleanroom environment.

2.4 Characterization

2.4.1 Precursor Characterization

Tensile strength of the PAN-PMMA bicomponent precursor filaments was tested using a single filament testing machine (FAVIMAT+, Measured Solutions Inc.). The precursor fiber tensile testing protocol is described by Lyon et al. [69]. Optical micrographs of the bicomponent precursor fiber tow cross-section were captured using a Leica optical microscope.

2.4.2 Hollow Carbon Fiber Characterization

The bulk density of the fibers was measured using a Micromeritics AccuPyc II 1340 gas pycnometer. The Scanning electron microscope (SEM) used to capture hollow carbon fiber cross sections was Hitachi SU8230 at an accelerating voltage of 5 kV. Individual fiber cross-sections were measured using ImageJ for every trial and at least 25 images were used to calculate the average diameter of the fibers. The “outer” diameter of the hollow carbon fiber was calculated using the area of the entire hollow carbon fiber cross-section, including

the hollow channels. The “effective” diameter of the hollow carbon fiber was calculated using the area of the solid cross section of the fiber. The solid cross-sectional area was calculated by subtracting the area of the seven hollow channels from the area of the entire fiber cross-section. Individual hollow carbon fiber filaments were mounted on paper tabs and were tensile tested using an RSA III solids analyzer. Tests were conducted using four different gauge lengths viz. 50.8 mm, 25.4 mm, 12.7 mm, and 6.4 mm, and the strain rate used was 0.1%/s. 25 samples were tested for each measurement. The average tensile moduli values were plotted as a function of inverse gauge length (Figure A.3), to obtain the compliance corrected modulus. The tensile properties from the single filament tests were measured at a gauge length of 12.7 mm.

Wide-Angle X-ray diffraction (WAXD) was used to characterize the structure of the bicomponent precursor and hollow carbon fibers. WAXD of the fibers was carried out using Rigaku Micromax– 007 (Cu K_α, λ = 1.542 A°, 65 mA, 45 kV). X-Ray exposure time was 30 min for each sample. The diffraction patterns were analyzed using AreaMax and MDI Jade 9.1 software. From the WAXD patterns of hollow carbon fibers, crystallite size L_{002} and L_{100} was calculated using Scherrer equation with K = 0.9 [70]. The orientation factor was determined from the (002) azimuthal scans at 2θ=17° for precursor, and 2θ=26° for carbon fibers using the procedure previously described by Sreekumar et al. [71]. Raman spectra were collected on a Horiba Scientific Xplora confocal micro-Raman system (laser wavelength = 785 nm).

Surface treated and sized, 740-filament carbon fiber tows from trial T5 were impregnated in epoxy and cured at 180 °C for 3 hours. The composite strands were

mounted on a 6-inch paper tab to prepare samples for tensile testing. Composite strands mounted on paper tabs are shown in Figure A.5. Fiber loading of strands from each spool was calculated from the measured linear density of the fiber tow from each spool. The tensile specimens were tested using an INSTRON (Load cell: 500 N, Testing speed: 300 mm/min). A total of 47 strands were tested as per ASTM D4018 [72].

The high-resolution X-Ray computed tomography (nano-CT) of individual hollow carbon fiber filaments was conducted using ZEISS Xradia 810 Ultra (5.4 keV, quasi-monochromatic) at the Air Force Research Laboratory, Dayton, OH. 701 projections were collected with high resolution field of view (16 μm), feature resolution of 50 nm, using Zernike phase contrast, and dwell time of 250 s. ORS Dragonfly was used to visualize the sample.

For the transmission electron microscopy (TEM), samples were prepared using dual-beam Thermofisher Scientific Helios G4 UC FIB/SEM. Carbon fibers were fixed with diluted resin on the substrate and a 1μm thick Pt protection layer was deposited perpendicular to the fiber axis. Thin lamellae were in-situ lifted out using a manipulator and mounted on the TEM grid. Additional thinning was performed at 5 kV for TEM observation. High resolution TEM images were taken using the JEOL JEM-ARM200cF with an accelerating voltage of either 80 kV or 200 kV.

Small-angle X-ray scattering (SAXS) measurements were conducted by using a Bruker NanoSTAR instrument with a sample-to-detector distance of 67.5 cm. Cu-K_α X-ray with the wavelength (λ) of 1.5418 Å was used. This instrument setting covers a scattering vector, q (defined as $\frac{4\pi}{\lambda} sin\frac{\theta}{2}$, where θ is the scattering angle), ranging from 0.014

to 0.35 $Å^{-1}$. The 2-D intensity data were collected by a MikroGap VÅNTEC-2000 detector with a pixel size of 67 μm. Scattering and transmittance of all samples were measured under vacuum separately. The 2D raw data were corrected by the sample transmission, empty beam scattering and transmission. The corrected data were then sector averaged (as indicated in Figure A.6), yielding the 1-D profiles, which were best fitted using long rectangular prism with the constrained dimensions based on the analysis of graphite crystals. We also simulated the 2D scattering pattern using the form factor of a long rectangular prism with preferred orientation in space to mimic the experimental patterns (Figure A.7). The 2D scattering patterns were "simulated" (not "fitted") results using SasView 4.2.2 software [73].

2.5 Results and Discussion

An optical micrograph of the 20-filament as-spun bicomponent fiber tow is shown in Figure 2.2. 19 out of 20 filaments have an average diameter of 42 μm. As is evident from Figure 2.2, only one filament has a significantly smaller diameter than the rest of the tow. However, the distribution of the PMMA islands within the fibers is uniform throughout the tow, and the islands were contained within the PAN sea in every single fiber. The uniformity of island distribution is maintained in the carbonized fiber tow. SEM images of hollow carbon fiber cross-sections from the 100-filament tow is shown in

Figure 2.3.

The average diameter of carbon fibers from each trial was used to calculate the tensile strength and modulus of fibers from different trials. Table 2.1 lists the precursor fiber drawing conditions and tensile properties, and these properties are compared to that

of single component, gel spun control PAN precursor produced at Georgia Tech. The tensile modulus of the bicomponent precursor is lower than that of the solid PAN precursors produced using gel spinning [6, 74]. This is expected given that the total draw ratio for the bicomponent precursors was in the range of 18-22 compared to a TDR of 25 in the case of control PAN precursor. The difference in drawability of PAN and PMMA limits the drawability of the bicomponent precursor. Additionally, PMMA has a significantly lower tensile modulus (2.9 GPa) compared to PAN (15-21 GPa) and therefore the reported tensile modulus for the PAN-PMMA bicomponent precursor is lower than that of the control PAN precursor. The structural parameters of the precursor fibers calculated from the WAXD patterns are listed in Table 2.2. The WAXD integrated pattern for precursor T5 is shown in Figure 2.4.

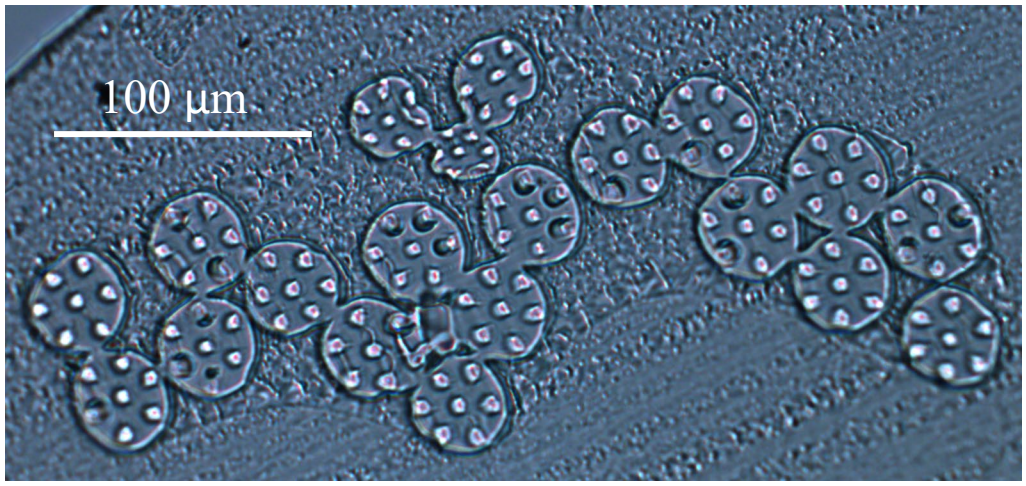

Figure 2.2 Optical micrograph of the 20 filament bicomponent precursor tow cross-section.

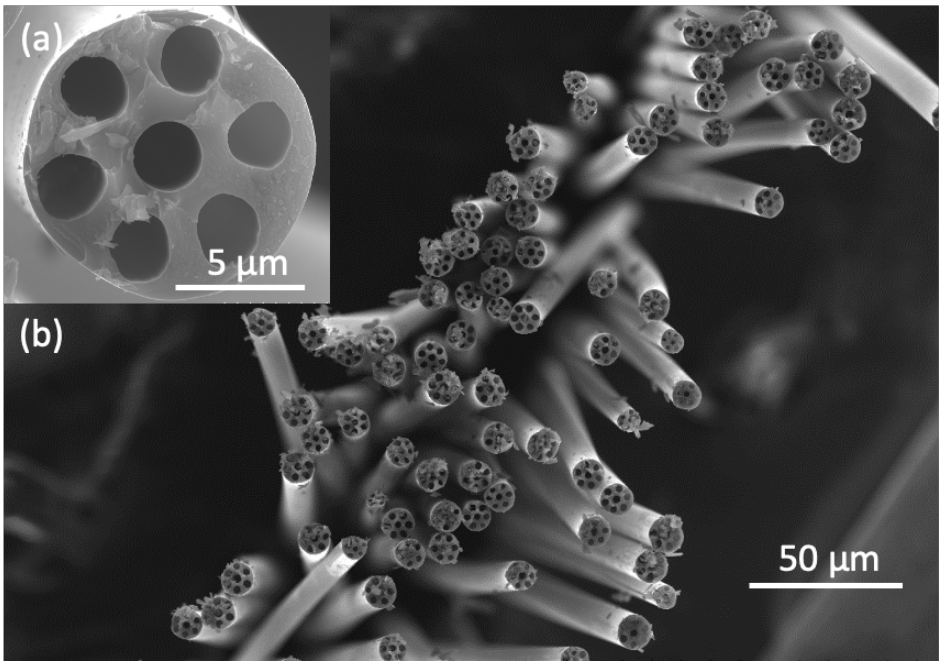

Figure 2.3 (a) SEM micrograph of individual hollow carbon fiber filament cross-section, (b) SEM image of a part of the 100 filament hollow carbon fiber tow.

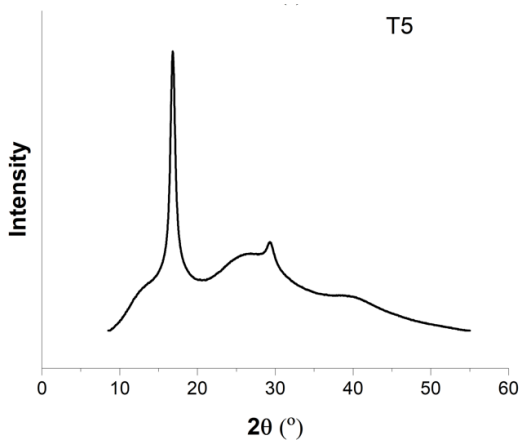

Figure 2.4 WAXD integrated scans of bicomponent precursor fibers from trial T5.

Table 2.1 Precursor fiber drawing conditions and tensile properties

Trial #	Spin Draw Ratio (SDR)	Post Spin Draw Ratio (PSDR)	Total Draw Ratio (TDR)	Fiber Diameter (µm)	Tensile Strength (GPa)	Tensile Modulus (GPa)
T1	2.3	6.1	14.0	16.3 ± 1.7	0.6 ± 0.07	14.0 ± 0.7
T2	2.3	5.6	12.9	18.1 ± 1.9	0.6 ± 0.04	12.9 ± 0.5
T3	2.3	8.2	18.9	16.6 ± 0.7	0.5 ± 0.1	12.2 ± 0.9
T4	2.3	7.6	17.5	16.7 ± 0.7	0.6 ± 0.04	12.4 ± 0.5
T5	2.3	6.2	14.3	16.9 ± 0.6	0.6 ± 0.05	12.0 ± 0.7
GT control PAN [6]	3.0	8.2	24.6	11.0 ± 0.8	1 ± 0.1	20.7 ± 1.1

The continuous stabilization and carbonization conditions for different trials are listed in Table 2.3. The strain in stabilization was varied between 9-12%. The range for low temperature (LT) carbonization strain was between 4-8%. During high temperature (HT) carbonization, the carbon fibers undergo shrinkage. Therefore, in the HT carbonization stage a negative strain in the range of -4.6% to -2 % can maintain tension in the fiber tow at 1450ºC. The stabilization residence time was between 200-305 min, and the carbonization residence time was in the range of 22-32 minutes for different trials. The 740 filament hollow carbon spools produced in trial T5 are shown in Figure A.4.

Table 2.2 PAN Structural parameters of precursor fibers from WAXD

Trial #	$L_{(200, 110)}$ (nm)	$d_{17°}/d_{30°}$ (equatorial)	$f_{200, Azi}$
T1	14.4	1.73	0.82
T2	13.4	1.73	0.83
T3	13.4	1.73	0.81
T4	13.7	1.74	0.82
T5	12.7	1.73	0.81

Table 2.3 Summary of continuous stabilization and carbonization processing parameters

Trial #	Stabilization			LT carbonization		HT carbonization		Total Carbonization Time (min)
	Residence Time (min)	Strain (%)	Temperature (°C)	Strain (%)	Temperature (°C)	Strain (%)	Temperature (°C)	
T1-1	305	12	180-250	8	500-675	-4.63	1450	33
T1-2	290	9	180-250	6	500-675	-4.48	1400	33
T2-1	261	9	180-250	6	500-675	-4.25	1450	29
T3-1	261	9	200-250	6	500-675	-3.02	1400	29
T4-1	200	9.9	200-250	4	500-675	-2.02	1400	22
T5-1	291	9.9	180-250	8	500-675	-4.40	1400	32

The tensile properties corresponding to the stabilization and carbonization conditions for the carbonization trials are summarized in Table 2.4. The hollow channel volume fraction in different trials varied from 28% to 40%. This was due to the different solution processing conditions, PAN and PMMA solution concentrations, and the post spin draw ratio used in different trials. The desired hollow channel volume fraction in the hollow carbon fibers can be controlled by changing these parameters. The effective tensile strength is calculated using the area of the solid cross-section of the hollow carbon fibers. This area was calculated from the SEM micrographs of individual hollow carbon fibers from the multifilament tow. The tensile strength based on the outer diameter considers the hollow portion of the carbon fiber as well, and is therefore lower than the "effective" tensile strength. To be able to replace the conventional carbon fibers in structural components, it is important that both the specific tensile strength and specific tensile modulus of the hollow carbon fibers be higher than conventional carbon fibers.

The tensile strength of the hollow carbon fibers is in the range of 2.3 – 3.0 GPa, and the tensile modulus is in the range of 202 - 234 GPa. The tensile modulus has been corrected for compliance. The tensile strength (trial T1-2) reported here is 80% higher than reported for batch carbonized hollow carbon fibers, with tensile modulus comparable to the batch carbonized hollow carbon fibers [29]. Table 2.5 compares the specific tensile properties of the hollow carbon fibers to that of commercial carbon fibers such as T300 and IM7. The density of the solid cross section of the hollow carbon fibers was measured to be 1.8 g/cm^3. The density of the hollow carbon fiber including the hollow channels was calculated to be 1.15 g/cm^3 using the 36% hollow channel volume fraction for fibers in trial T1-2 (Table 2.4). The specific tensile modulus is over 40% higher than T300 and 20%

higher than IM7 carbon fibers. The specific tensile strength falls in between T300 and IM7 carbon fibers, based on the current processing conditions. Therefore, the continuous hollow carbon fibers are superior to T300 in both tensile strength as well as modulus.

Table 2.4 Summary of tensile properties of continuous hollow carbon fibers produced in different trials

Trial #	Tow Size #filaments	Fiber Diameter (μm)		Tensile Strength (GPa)		Tensile Modulus (GPa)		Strain to Failure (%)	Hollow Channel Volume Fraction (%)
		Effective	Outer	Effective	Outer	Effective	Outer		
T1-1	100	7.6	9.5	4.3 ± 1.0	2.8	339 ± 30	217	1.3 ± 0.3	36
T1-2	100	7.9	9.7	4.6 ± 1.2	3.0	333 ± 22	221	1.2 ± 0.2	36
T2-1	100	9.1	11.7	4.0 ± 0.8	2.5	370 ± 78	226	1.2 ± 0.2	39
T3-1	222	8.2	9.8	4.1 ± 0.6	2.9	326 ± 27	228	1.3 ± 0.3	30
T4-1	222	8.2	9.8	3.8 ± 1.3	2.7	335 ± 58	234	1.2 ± 0.4	28
T5-1	740	9.2	11.2	3.5 ± 0.6	2.3	300 ± 30	202	1.2 ± 0.2	33

Table 2.5 Comparison of specific tensile properties of commercial and hollow carbon fibers

	T300 [75]	**GT Hollow Carbon Fibers (T1-2)**	**IM7 [1]**
Density (g/cm^3)	1.76	1.15	1.78
Specific tensile strength (N/tex)	2.0	2.6	3.1
Specific tensile modulus (N/tex)	131	192	155

Hollow carbon fiber tows from trials T3-1, T4-1, and T5-1 were surface treated and sized. Fiber tows from trial T5-1 were impregnated with epoxy to prepare composite strands for tensile testing as detailed earlier. The tensile results from individual filament tests and the composite strand tests indicate that the 25 individual filaments tests are representative of the tensile properties of the entire tow. These results are summarized in Table A.1.

WAXD and Raman analysis summarized in Table 2.6 provides insights into the structure of the hollow carbon fibers. The L_{002} crystallite size of the continuous hollow carbon fibers was higher than the batch carbonized hollow carbon fibers. The FWHM at $2\theta \sim 26^{o}$ for hollow carbon fibers in trial T1-2 is lower than the batch carbonized fibers and comparable to IM7 carbon fibers. The similarity of crystallite size as well as d-spacing in trials T1 and T5 seems to indicate that the scale up from 100-filament to 740 filament tow has not affected the structure of the hollow carbon fibers. The integrated WAXD patterns for hollow carbon fibers trials T5-1 is shown in Figure 2.5.

The Raman I_G/I_D ratio indicates a higher level of graphitic order at the surface of the hollow carbon fibers as compared to IM7 carbon fibers. The difference between the I_G/I_D ratio in fibers from trial T1-2 and T5-1 is within the standard deviation observed from multiple measurements. These results indicate that the inherent structure of the hollow carbon fibers is similar or better than that of IM7 carbon fibers and has resulted in a higher tensile modulus.

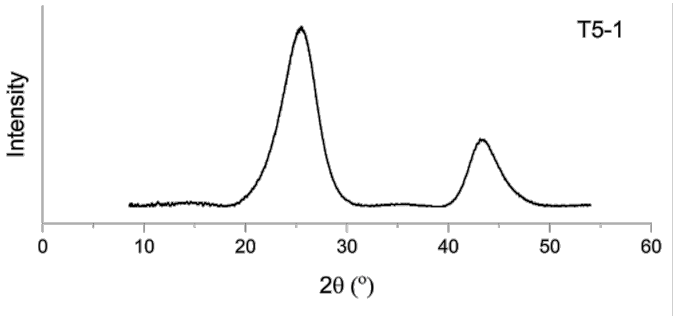

Figure 2.5 WAXD integrated scans of hollow carbon fibers produced from trial T5-1 (740 filament tow)

The tensile strength is limited by the size of the largest defect present in the carbon fibers. Using Griffith's equation for brittle fracture (Equation 1) [76], the size of the largest defect in the fibers can be estimated. In Equation 1, σ is the tensile strength, E is the tensile modulus, c is the size of the largest defect, and γ_a is the apparent surface energy (4.2 J/m^2 for graphite). Using this equation, we calculated the size of the largest defect in the hollow carbon fibers and listed in Table 2.7. It is important to note, to calculate the size of the largest defect in the solid cross section of the fiber we need to use the tensile strength and tensile moduli values based on the effective diameter.

$$\sigma = \sqrt{\frac{2E\gamma_a}{\pi c}} \quad (1)$$

Table 2.6 Structural parameters of hollow carbon fibers

Trial #	**L_{002} (nm)**	**L_{10} (nm)**	**$d_{(002)}$ (Å)**	**$FWHM_{Azi,\ 002}$ (°)**	**$f_{(002),\ azi}$**	**Raman I_G/I_D**
Trial T1-2	1.8	2.6	3.48	30.7	0.83	0.49
Trial T5-1	1.9	2.6	3.53	32.3	0.82	0.53
Batch carbonized hollow carbon fiber [29]	1.3	2.1	3.52	33.2	0.80	N/A
GT Control carbon fibers [6]	1.9	2.5	3.44	23.1	N/A	0.46
IM7 [6]	1.6	2.1	3.48	30.3	0.83	0.43

Table 2.7 Hollow carbon fiber defect size calculation based on Griffith's equation

Trial #	Tensile Strength (GPa)		Tensile Modulus (GPa)		Size of Largest Defect (nm)
	Effective	Outer	Effective	Outer	
T1-1	4.3	2.8	339	217	49
T1-2	4.6	3.0	333	221	42
T2-1	4.0	2.5	370	226	62
T3-1	4.1	2.9	326	228	52
T4-1	3.8	2.7	335	234	62
T5-1	3.5	2.3	300	202	66
GT Control Carbon Fiber [6]	5.5		350		31
IM7 [1]	5.5		276		24

For hollow carbon fibers, with tensile strength of 3.5 – 4.7 GPa, and tensile modulus of 300 – 370 GPa, based on the effective diameter, the size of the largest defect can be estimated to be ~ 40 – 65 nm. Applying the same calculation, the estimated size of the defects in IM7 carbon fibers is ~ 24 nm, and that in GT control carbon fibers is ~31 nm. Therefore, in order to match or exceed the tensile strength of IM7 carbon fibers, the size of the defects in hollow carbon fibers needs to be restricted to less than 25 nm. These defects could arise due to multiple factors. The entanglements in the polymer will introduce inherently present defects with a minimum size of 2 nm [6]. Entanglement of more than two molecules will create defects larger than 2 nm. The defects near the surface are likely to be formed during fiber spinning, drawing, stabilization and carbonization. It is therefore

critical to understand the processing stage at which these defects are being introduced and modify that processing stage to prevent the formation of the defects.

The TEM images at different locations on the hollow carbon fiber cross section are shown in Figure 2.6. The TEM images of a commercial high-performance PAN based carbon fiber, and GT control carbon fiber are included in Figure 2.7 for comparison. The TEM images of hollow carbon fiber cross sections from Figure 2.8 reveal defects near the surface of the hollow carbon fibers. These defects are present in the outer 160 nm region near the fiber edge and their size is in the range of 5-20 nm. The number of these surface defects are significantly higher compared to those seen on the surface of GT control carbon fibers in Figure 2.9. In the solid carbon fibers, the surface defects seem to be present in the first 40 nm region from the fiber surface, and the size of the largest defect is 10 nm. There are no large defects (>10 nm) visible in the inner cross section of the hollow carbon fiber specimen. The surface defects in the hollow carbon fibers are smaller than the calculated defect size from Table 2.7. It may be possible that the defects near the surface region being close to each other, may collectively act as a larger size defect in the range of 40-60 nm, and could be limiting the tensile strength. The surface defects in the GT control carbon fibers are smaller than the calculated value as well, however, these defects are more infrequent compared to that in hollow carbon fibers, and therefore these defects are less likely to collectively form a larger defect than in hollow carbon fibers. That may be one explanation for the higher tensile strength in the GT control carbon fibers than the hollow carbon fibers. There could be other strength limiting defects present elsewhere in the cross section as well. Therefore, it is important to analyze the fiber structure over a larger length scale (>10 μm). A representative image of a hollow carbon fiber filament captured using

X-Ray nano-CT is shown in Figure 2.10. The tomograms allow 3D visualization of hollow carbon fibers over significantly larger length scales (>10 μm), and allow imaging of thousands of cross sections in a much shorter time compared to SEM and TEM. Further characterization using this technique at a higher resolution could lead to a better understanding of the shape and size of defects present in carbon fibers. This could help in identifying and modifying the process in which the strength limiting defects are being introduced and reduce their size to increase the fiber tensile strength.

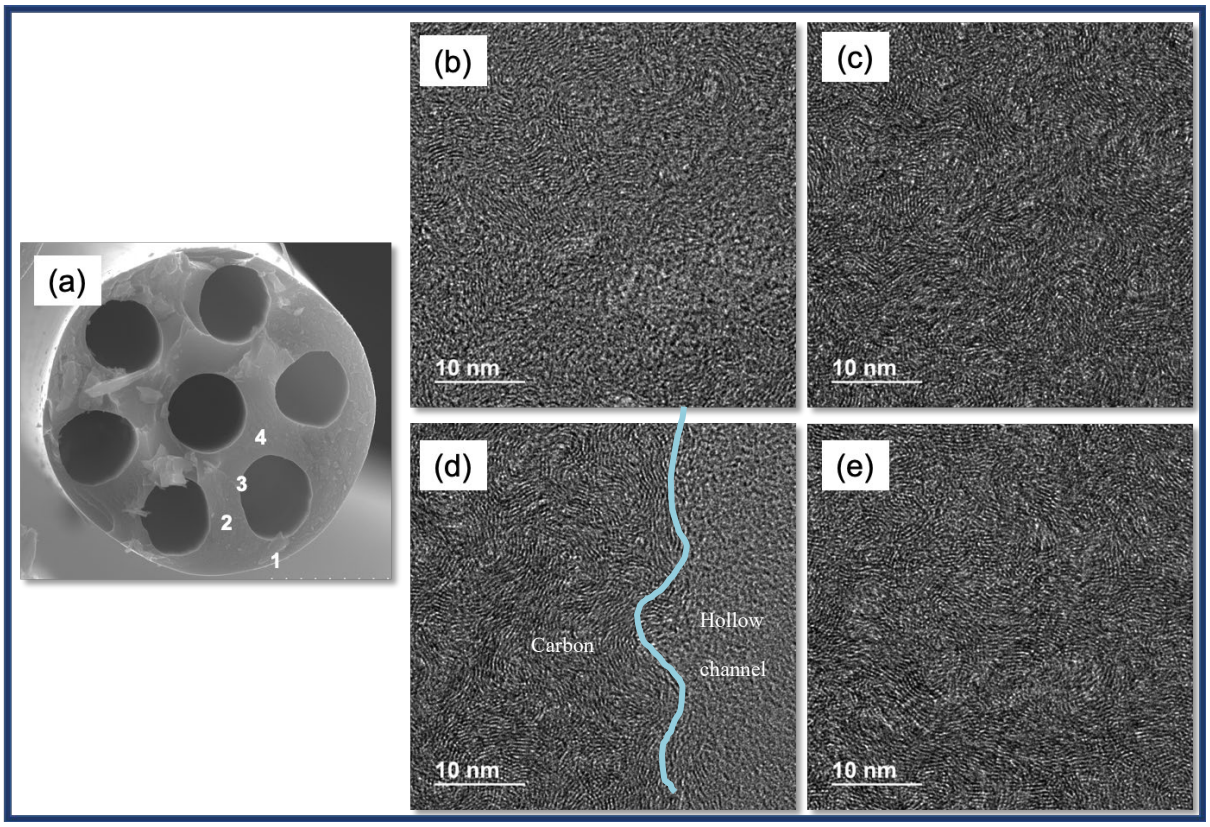

Figure 2.6 Transmission electron micrographs of the hollow carbon fiber cross section at different locations on the fiber cross sections (b-e). (a) SEM image of hollow carbon fiber. TEM images of the fiber at (b) location 1 near the fiber edge, (c) location 2 between the hollow channels, (d) location 3 near the inner wall of the hollow channel, and (e) location 4 between the hollow channels.

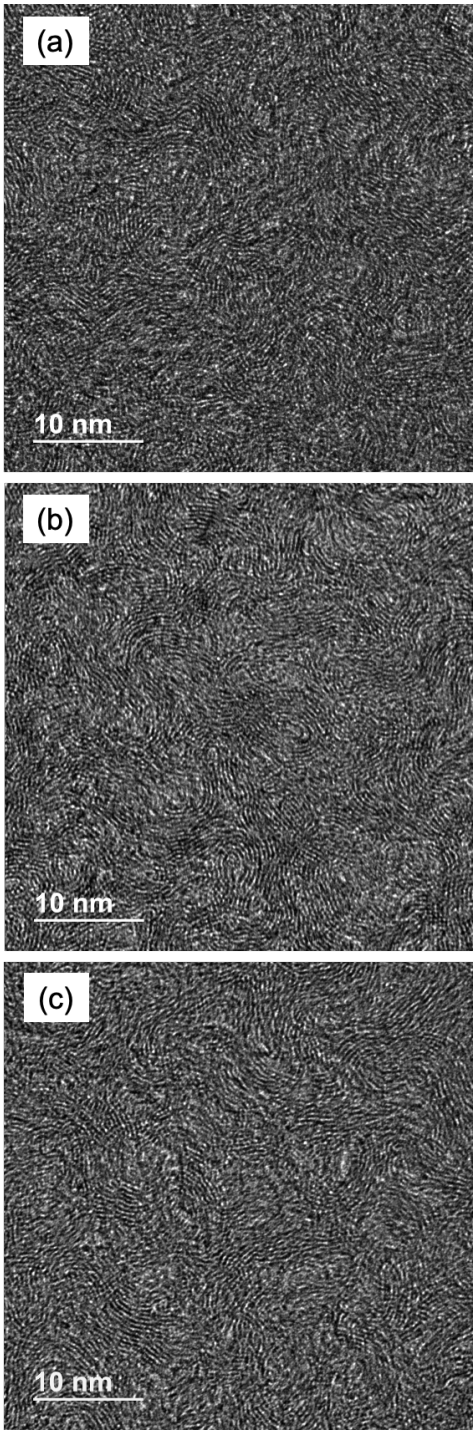

Figure 2.7 Comparison of the carbon fiber structure from TEM micrographs from (a) Hollow carbon fiber, (b) GT control carbon fiber, (c) Commercial high-performance PAN based carbon fiber.

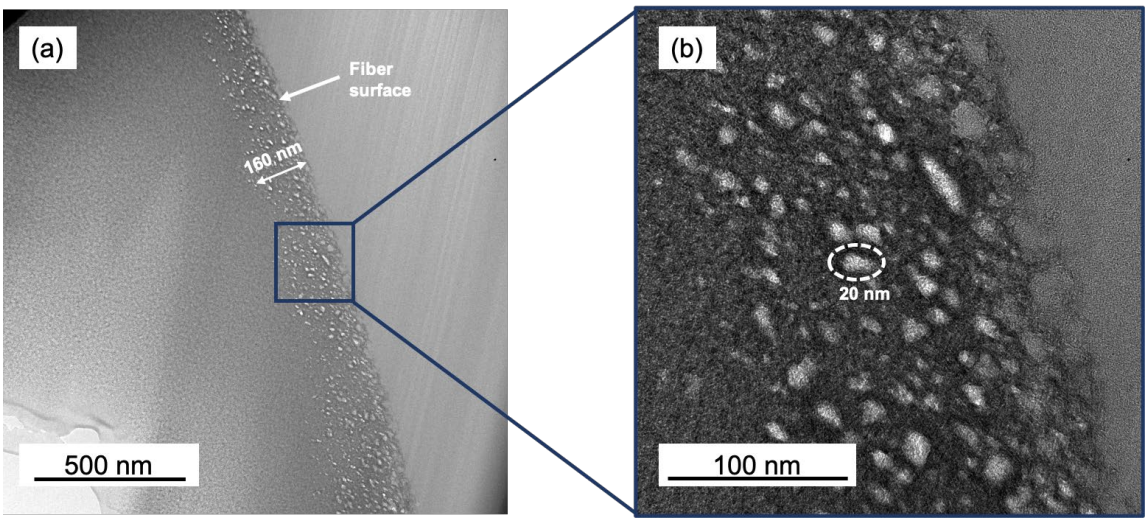

Figure 2.8 (a) TEM image of the hollow carbon fiber surface indicates presence of defects or voids on the fiber surface. These defects are present in the first 160 nm from the fiber surface. There are no large (>10 nm) defects visible further inside the fiber cross-section. (b) The larger defects are in the close to 20 nm.

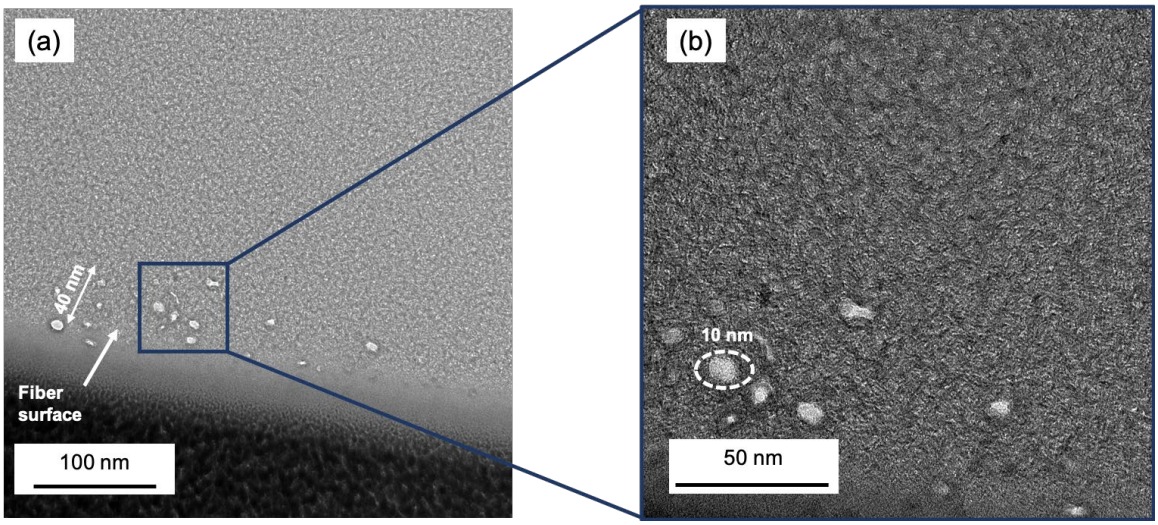

Figure 2.9 (a) TEM image of the GT control carbon fiber surface. Fewer defects near the surface as compared to the hollow carbon fibers. The defects are only visible in the first 40 nm from the fiber surface. (b) Largest defect size near the surface was measured to be 10 nm.

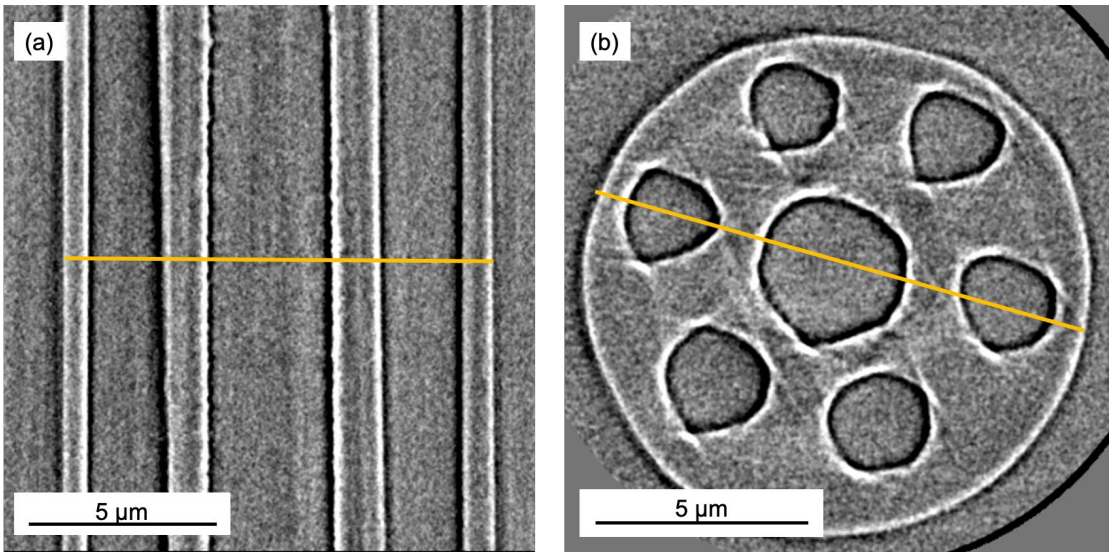

Figure 2.10 (a) X-Ray nano-CT image of the hollow carbon fiber channels, and (b) the cross-section of the hollow carbon fiber. The gold line in (b) indicates the transverse plane which is shown in (a).

SAXS measurements were performed to obtain the detailed orientation information of graphitic planes in the hollow carbon fibers. Figure A.6 shows the 2D scattering pattern for sample T5-1, T1-2 and GT control carbon fibers. All samples show a highly anisotropic butterfly-like scattering pattern with high intensity vertically (Y-axis), as the fiber axis was placed horizontal (X-axis), and perpendicular to the incident X-ray beam (Z-axis). According to Babnet's principle, the SAXS pattern can be contributed by either the graphite crystals or microvoids [77, 78]. In this study, we simulated the multi-layer graphite as a solid rectangular slab with an approximated cross-section of 2 nm x 2 nm based on the WAXD results (Table 2.6) with a length > 100 nm, which is an arbitrary value because the dimension is beyond the SAXS limit, as indicated in Figure A.7(b). It should be noted that the rectangles could represent elongated microvoids [77]; however, the uniform cross-sectional dimension would not be expected. The internal structure of the rectangular slab is too small to be resolved by the maximal attainable high-q limit and its electron density

is, therefore, assumed to be uniform. The 2D simulation on the XY-plane was performed under the assumption that the slab's long axis mainly aligned along the fiber axis (X-axis) with the other two short axes randomly oriented about X-axis, while the slab is allowed to rotate by ±10° about the incident beam (Z-axis) and Y axes, respectively, yielding the "fan" patterns along Y-axis in the 2D scattering pattern. The fact that the simulated 2D scattering pattern resembles the experimental data well (Figure A.6) confirms the morphology and the orientation of graphite or microvoids. We acknowledge that the 2-D simulation is based on scattering from dilute system, while the comparison of the orientation of the slab in different samples remains valid even under a concentrated condition. An azimuthal integration in the q range between 0.1 and 0.16 $Å^{-1}$ from the 2D scattering pattern (Figure A.8) was performed. The outcome shows that sample C has the smallest full-width-half-maximum (FWHM), indicating a narrower orientational distribution of the slabs among the three fibers. Another SAXS analysis is to focus on the intensity decay along the detector Y-axis (sector I in Figure A.6) which is mainly contributed from the scattering intensity along the radial direction (e.g., cross-section) of the elongated slab due to the preferred orientation. The reduced 1-D SAXS data from the sector average of this region (Figure 2.11) exhibit a general feature of a power-law decay ($0.014\ Å^{-1} < q < 0.02\ Å^{-1}$) followed by a smooth transition ($0.02\ Å^{-1} < q < 0.04\ Å^{-1}$) and then another power law decay ($q > 0.02\ Å^{-1}$). Firstly, the fact that the three sets of SAXS data exhibit a similar pattern for $q > 0.07\ Å^{-1}$, which can be best fitted using a long slab with a cross-sectional dimension of (1.0 ~ 1.2 nm) x (1.4 ~ 1.7 nm), agrees with the morphology suggested by 2D simulation results and the WAXD analysis. This outcome indicates that all three samples have similar dimensions of crystalline domains or microvoids.

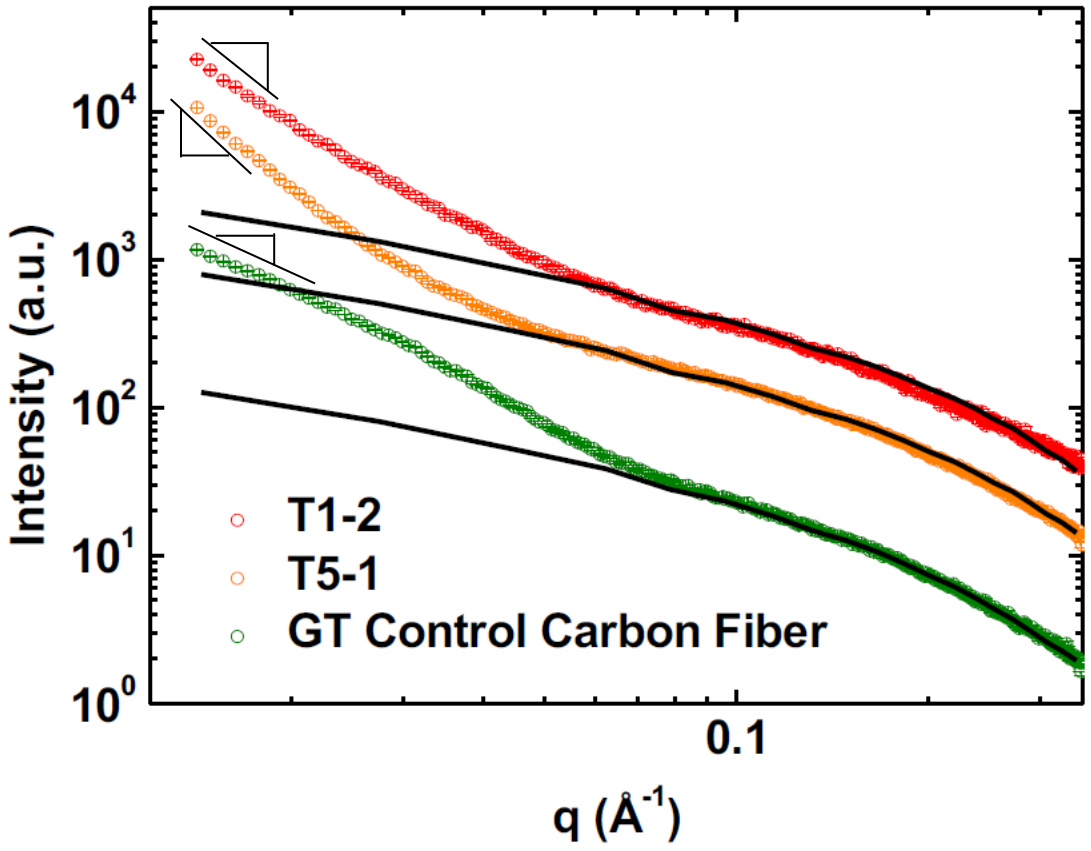

Figure 2.11 SAXS 1D scattering pattern averaged in sector I for sample T1-2 (red), T5-1 (orange) and GT control carbon fiber (green). The definition of the sector is presented in Figure A.6.

The first (low-q) power-law decay stems from the tail of the scattering intensity from large objects whose dimension exceeds $2\pi/q_{min}$ with q_{min} being the attainable minimal q value. The power exponent of the decay reflects the interfacial scattering of the large objects. It is known that smooth and fractal surface (or interface) renders q^{-4} (Porod scattering) and from q^{-3} to q^{-4} intermediate decay, respectively [79]. The samples T5-1 and T1-2 reveal $q^{-3.5}$ and q^{-4} decay, respectively, suggesting that T5-1 may contain more surface defects, yielding fractal surface scattering behavior in comparison with T1-2, consistent with the lower tensile properties observed in T5-1 (more surface defects). It should be noted

that the GT control carbon fibers exhibit a q^{-2} decay, which is likely attributed to the scattering from 2D (layer) objects with the lateral dimension larger than $2\pi/q_{min}$ (> 30 nm).

One of the key differences in manufacturing of hollow carbon fibers and conventional single component carbon fibers, is the presence of PMMA and its subsequent degradation. PMMA is known to degrade in the range of 350 - 500 ºC [28, 80]. However, rapid degradation of PMMA could potentially cause the formation of the larger sized defects that are currently limiting the tensile strength. In the current process, the stabilization step concludes at 250 ºC and the LT carbonization oven is maintained at a temperature between 500-675 ºC. The stabilized fibers after passing through the stabilization process enters the LT carbonization stage with a temperature increase of 250 ºC. PMMA does not degrade during the stabilization step but rapidly degrades as the tow is introduced to the LT carbonization stage at 500 ºC. This may be resulting in rapid degradation of PMMA thus forming the 40-65 nm sized defects in hollow carbon fibers thus limiting the tensile strength. The defect formation could be restricted if the rate of PMMA degradation was controlled. However, this is yet to be verified. At the same time, there could be other stages in the hollow carbon fiber manufacturing process that could be modified to further improve the tensile strength. The sacrificial PMMA component is expected to increase slightly the raw material and precursor fiber spinning costs. However, the rest of the manufacturing process, which includes fiber drawing, continuous stabilization and carbonization equipment does not require any modification, and therefore these processes will not cost more than conventional carbon fiber manufacturing. The nominally higher costs of hollow carbon fiber manufacturing are therefore outweighed by

the immediately realized potential composite weight savings and the long-term reduction in fuel consumption for aerospace vehicles.

Increasing the tensile strength further while maintaining the superior tensile modulus of the hollow carbon fibers remains critical. One way to increase the strength of the hollow carbon fibers would be to reduce the effective diameter of carbon fibers. Currently, the effective diameter of the hollow carbon fibers is in the range of 7.6 - 9.2 μm, higher than T300 carbon fibers and significantly higher than IM7 carbon fibers. However, the current tensile strength falls between the T300 and IM7 carbon fiber values. The tensile strength of carbon fibers is reported to increase with a decrease in the fiber diameter, since the smaller diameters lead to smaller defect size in the fibers [64]. The diameter of the hollow carbon fiber can be reduced by changing the bicomponent precursor spinning conditions such as the spinneret hole diameter, PAN/PMMA ratio in the precursor fiber, draw ratio etc. Therefore, we believe that by reducing the effective diameter of the fiber while maintaining the hollow channel volume fraction, in combination with further optimization of stabilization and carbonization conditions, will lead to tensile strength values higher than the IM7 carbon fiber tensile strength. Further tensile strength increase in hollow carbon fibers will also lead to a higher strain to failure, which is important in manufacturing carbon fiber composites. Additionally, hollow carbon fibers allow for a larger outer diameter while maintaining a smaller effective diameter. The higher outer diameter is expected to lead to higher resistance to buckling under compressive loading in hollow carbon fibers. Therefore, producing hollow carbon fibers with effective diameter comparable to IM7 carbon fibers (~5 μm), is also expected to result in superior compressive strength as compared to IM7 carbon fibers [29]. The mechanical properties of hollow carbon fiber

composites are reported in Chapter 3. The hollow carbon fibers therefore hold significant potential for a paradigm shift in designing lightweight carbon fiber composites for aerospace applications.

2.6 Conclusions

Continuous multifilament hollow carbon fiber tows were successfully manufactured with tow sizes ranging from 100 to 740 filaments. Over 80% improvement in tensile strength has been achieved compared to batch carbonized hollow carbon fibers reported before. The continuous hollow carbon fiber tensile properties are higher than T300 carbon fibers. The specific tensile modulus is higher than IM7 carbon fibers however, the specific tensile strength needs further improvement. TEM images of hollow carbon fibers indicate surface defects, which could be potentially limiting the tensile strength of the fibers. Further characterization using synchrotron-based X-Ray nano-CT will help better characterize the defects at higher resolution. The size of the defects in hollow carbon fibers could be potentially reduced by to controlling the rate of the PMMA degradation by modifying the stabilization and carbonization process parameters. Based on the tensile properties achieved so far, the hollow carbon fibers show promise of being able to replace state of the art aerospace grade carbon fibers to significantly reduce the weight of composite materials.

CHAPTER 3. HOLLOW CARBON FIBER COMPOSITES

3.1 Background

Mechanical properties and advantages of using carbon fibers are realized when the fibers are used in composite materials as a reinforcement [81]. Tensile properties of unidirectional continuous carbon fiber composites are dependent on two key characteristics viz. the tensile strength and moduli of the carbon fibers and the interfacial adhesion between fiber and matrix which enables effective load transfer. Fibers are typically surface treated and sized to improve surface wetting characteristics and ensure interfacial adhesion between the fiber surface and the matrix. Based on the mechanical properties of the fiber, surface treatment and the type of matrix used (epoxy, thermoplastics etc.) there are different ways in which composite failure may occur under tension including but not limited to fiber pullout, fiber cracking and matrix cracking. In case of carbon fiber-epoxy composites, failure is brittle. The strain to failure is typically dictated by the strain taken by the reinforcement and therefore is typically 1-2% for carbon fiber composites.

The most common modes of compressive failure in unidirectional composites are micro-buckling, kinking, fiber failure, and delamination failure [82]. Like tension, compressive properties of the composite are largely determined by the fiber compressive properties. The composite compressive strength is lower than the tensile strength [83]. For IM7 carbon fibers, the unidirectional composite compressive strength was reported to be 1.7 GPa compared to the tensile strength of 2.7 GPa [1]. Thus, compressive strength was 60% of the tensile strength. It has been previously hypothesized that larger diameter carbon

fibers (~ 10 μm) would be more stable under a compressive load and less prone to buckling and therefore the composites have higher compressive strength than the conventional carbon fiber composites (5-7 μm diameter) [29]. It is important to note that buckling behavior is not a strength property but indicates the stability of the material under load. With this thought, multichannel hollow carbon fibers (hollow CF) with diameters between 9-11 μm were manufactured as described in CHAPTER 2. The hollow carbon fiber composites show an improvement in the compressive properties compared to reported IM7 numbers. The compressive strength (0.9 GPa) of the hollow carbon fiber composites is over 80% of the tensile strength (1.1 GPa) compared to 60% for IM7 composites.

3.2 Materials

Continuous hollow carbon fibers were manufactured as described in CHAPTER 2 (Specimen T5) and IM7 fibers were obtained from Hexcel. Gel-spun PAN-based carbon fibers, hereafter referred as GT control carbon fibers, were manufactured at Georgia Tech as described by Chae et al. [6]. The epoxy matrix used was CYCOM 977-3 from Solvay. Fiberglass tabbing material for tension tests was obtained from McMaster Carr Inc. Unidirectional carbon fiber epoxy composite tabs for compression testing were obtained from ACP Composites Inc. Tabs were bonded to the composite test specimen using 3M DP460NS Scotch Weld adhesive.

3.3 Composite Manufacturing

Hollow CF and IM7 prepregs (both 6-ply, unidirectional) were manufactured at the University of Southern Mississippi using a drum winding process. The fibers were pulled from spools over a drum whereupon they were impregnated with resin (via vacuum

bagging) to a specified areal weight to achieve ~60% fiber volume fraction. The laminates were manufactured by using six layers of prepreg followed by autoclave curing using publicly available processing information for CYCOM 977-3 by SOLVAY [84].

GT control fiber composites were manufactured by Vuronyx Inc. Unidirectional prepregs were manufactured using drum winding followed by vacuum bagging. The matrix used was CYCOM 977-3, same as the one for hollow CF composites. The laminates were prepared by individually heating prepreg layers at 80 ºC for 30 min and stacking five layers. This was followed by autoclave curing with a 1-hour pre-cure at 120 ºC followed by overnight curing at 180 ºC.

3.4 Sample Preparation

Composite panels and tabbing materials were cut to dimensions using a waterjet. Specimen and tabbing material dimensions are listed in Table 3.1.

Table 3.1 Summary of composite tension and compression tests

Test	Specimen dimension	Tab dimension
Tension	10” x 0.5” x 0.04”	2.5” x 0.5” x 0.04”
Compression	3.18” x 0.5” x 0.04”	1.496” x 0.5” x 0.04”

For compression tests to be conducted at 180 °F (82 °C), the tabbed (strength tests) and untabbed (modulus tests) specimens were preconditioned in water. First the specimens were dried at 200 °F (94 °C) in an oven for 48 hours. The weight of the untabbed specimen was recorded to the nearest 0.01g. The tabbed and untabbed specimens were then soaked

in deionized water at 160 °F (72 °C) for 336 hours. The weight of the untabbed specimens was recorded post-conditioning and the moisture pickup was calculated.

3.5 Mechanical Testing Methods

Tension and compression tests for hollow CF and IM7 composites were conducted at the Materials Processing Characterization Facility (MPCF) at Georgia Tech. A uniaxial servohydraulic test system was used in conjunction with the MTS 793 multipurpose testware (MPT) software. Tension and compression tests are summarized in Table 3.2. For tension tests conducted at -75 °F (-59 °C) and compression tests conducted at 180 °F (82 °C), an environmental chamber was used. Five specimens were tested for each test and temperature condition.

Table 3.2 Summary of composite tension and compression tests

Composite	Test
Hollow CF and IM7	Tension (ASTM D3039): Room Temperature and -75 °F (-59 °C)
	Compression Strength and Modulus (Modified ASTM D695): Room Temperature (27 °C) and 180 °F (82 °C)

3.5.1 Tension testing

Tension tests were performed at room temperature and -75 °F (-59 °C) per ASTM D3039 [85]. Testing speed was 5.12 mm/min and strain was measured using a an

extensometer as shown in Figure 3.1. For cold temperature tests, specimens were cooled down to -75 °F (-59 °C) over a 20 min period and equilibrated for 3-4 min before starting the test. The tensile strength of the composite specimen was dividing the maximum force before failure by the cross-sectional area of the sample. For each sample the width and thickness were measured to calculate the cross-sectional area. The tensile modulus was calculated over the strain range of 0.1 - 0.3%.

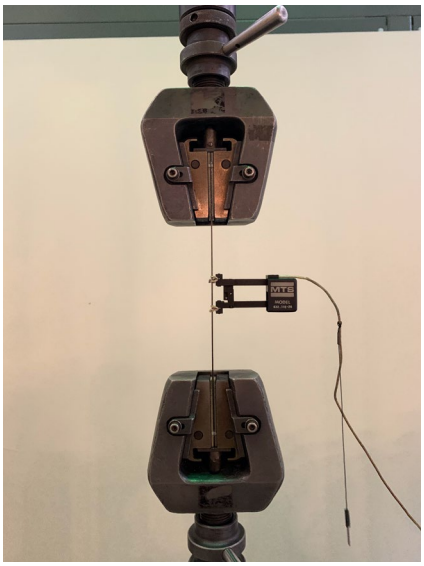

Figure 3.1 Composite specimen with extensometer mounted for ASTM D3039 tension test

3.5.2 Compression testing

Compression tests were performed at room temperature and 180 °F (82 °C) per modified ASTM D695 [86]. Testing speed was 1.3 mm/min. For high-temperature tests, specimens were heated to 180 °F (82 °C) over a 20 min period and equilibrated for 3-4 min

before starting the test. For compression modulus tests, strain gauges were bonded to each specimen to accurately record the strain during compression. The support fixture used for the modified D695 test is shown in Figure 3.2. For each sample the width and thickness were measured to calculate the cross-sectional area. Compressive strength was calculated by dividing the maximum force before failure by the cross-sectional area. Compressive modulus was calculated by calculating the slope of the initial linear portion of the stress-strain curve as described in ASTM D695.

Figure 3.2 Specimen support fixture for modified ASTM D695 compression test

3.6 Composite Characterization

3.6.1 Composite fracture characterization

Composite fracture surfaces after tension and compression testing were characterized using a Hitachi SU8230 scanning electron microscope (SEM) at an

accelerating voltage of 10 kV. For tension specimen, visual failure mode of the composite was also documented as prescribed in ASTM D3039.

3.6.2 Fiber volume fraction

Thermogravimetric analysis (TGA) was conducted to determine the fiber weight fraction in the composites. Composite specimens were heated in air atmosphere to 450ºC with a 10 ºC/min heating ramp and held at 450ºC for 5 hours to ensure complete degradation of the epoxy matrix. The fiber volume fraction was then calculated using the density of carbon fibers (reported in chapter 2) and epoxy [84].

3.6.3 Fiber alignment

Wide-Angle X-ray diffraction (WAXD) was used to measure the alignment of fibers in the composites. WAXD of the fibers was carried out using Rigaku Micromax– 007 (Cu K_α, λ = 1.542 A°, 0.65 mA, 45 kV). X-Ray exposure time was 30 min for each sample. The diffraction patterns were analyzed using AreaMax and MDI Jade 9.1 software. The orientation factor was determined from the (002) azimuthal scans at 2θ=26° for carbon fibers using the procedure previously described by Sreekumar et al. [71].

3.7 Results

Results of the tension and compression tests are summarized Table 3.3 and Table 3.4, respectively.

Table 3.3 Tensile properties of composite specimen

Composite	Room Temperature (27 °C)			-75 °F (-59 °C)		
	Tensile strength (MPa)	Tensile Modulus (GPa)	Strain to failure (%)	Tensile strength (MPa)	Tensile Modulus (GPa)	Strain to failure (%)
Hollow CF	1072 ± 49	99 ± 6	1.1± 0.1	959 ± 93	100 ± 5	1.0 ± 0.1
IM7 (measured)	1905 ± 106	142 ± 10	1.4 ± 0.2	1907 ± 52	159 ± 10	1.1 ± 0.1
IM7 (reported) [1]	2723	164	1.6		N/A	
GT control CF	2950 ± 73	180 ± 5	N/A		N/A	

Table 3.4 Compressive properties of composite specimen

Composite	Room Temperature (27 °C)		180 °F (82 °C)	
	Compressive strength (MPa)	Compressive Modulus (GPa)	Compressive strength (MPa)	Compressive Modulus (GPa)
Hollow CF	867 ± 30	98 ± 4	564 ± 83*	105 ± 2
IM7 (measured)	969 ± 130*	136 ± 5	575 ± 100*	141 ± 4
IM7 (reported) [1]	1689	150	N/A	
GT control CF	1655 ± 100	152 ± 8	N/A	

*Compressive strength of the samples is likely underestimated since the samples experienced end-crushing and did not fail in the intended gauge length region.

The results form TGA analysis combined with the composite moisture pickup are summarized in Table 3.5 Summary of fiber-epoxy composition and composite moisture pickup. The percentage moisture pickup for the hollow CF composite specimen (2.9%) is 1.8% higher compared to IM7 composite (1.1%). The difference in moisture pickup for epoxy could be attributed to the higher percentage of epoxy in the hollow CF specimen compared to IM7 composite. The percentage moisture pick-up difference in the two specimen is due to the difference in the weight of the composite specimen i.e. hollow CF specimen (~1.35 g) are lighter than IM7 specimen (~1.73 g) of the same dimension. However, the 2.2% difference in epoxy moisture pickup is likely insignificant, if the absolute weight gain in the composite is considered, for the following reason: average (over 5 specimen) moisture pickup for both IM7 and Hollow CF composites was same (~ 0.02 - 0.04 g, appendix B - table B1 and B2). This means that even a 0.01g difference in weight reading, well within the range of error of the weighing balance, could change the percentage moisture pickup measurement by ~1%. In other words, a 0.01-0.02g error in the weighing balance leads to a standard deviation of 1-1.5%, which means the percentage moisture pickup by the epoxy matrix in hollow CF and IM7 composite are within the range of one standard deviation. Additionally, hollow channels make up to 36% volume in the hollow CF, translating to ~20% of the total composite volume. If there was any moisture pickup in the hollow channels, the weight gain would have been between 20-25%, significantly higher than the 2.9% weight gain that is currently observed. These facts combined suggest that the hollow channels in hollow CF composites are not picking up moisture.

Table 3.5 Summary of fiber-epoxy composition and composite moisture pickup

Composite	Fiber wt%	Epoxy wt%	Fiber density (g/cm^3)	Epoxy density (g/cm^3)	Fiber volume fraction (%)	Composite moisture pickup (%)	Epoxy moisture pickup (%)
Hollow CF	56	44	1.15	1.29	58.8	2.9	6.7%
IM7	62	38	1.78		54.2	1.1	4.5%

The average tensile strength and moduli of Hollow CF composites at room temperature and -75 °F are nearly the same and within the standard deviation, which indicates that the composite performance under tension was not affected by the change in temperature. The same is observed for IM7 composites, where the tensile properties are not affected by lower temperature.

Hollow CF composite tensile strength is lower than what is expected from the individual fiber tensile strength values and the volume fraction of fiber in the composite, based on the rule of mixtures. The expected tensile strength, based on the hollow carbon fiber strength of 2.3 GPa and 58.8% fiber volume, is ~1.35 GPa. However, the measured tensile strength for the hollow CF composites is 0.95 – 1.1 GPa. This indicates potentially ineffective load transfer between the epoxy and hollow carbon fibers. This likely the reason why the commercially reported value for IM7 unidirectional composite is 2.7 GPa compared to the 1.9 GPa measured in this study, which is ~30% lower.

The low tensile strength of the hollow CF and IM7 composites can be attributed to poor adhesion between fiber and matrix in hollow carbon fiber composites compared to IM7 composites. It is evident from Figure 3.3 and Figure 3.4 that hollow CF composites

have poor adhesion between epoxy and fibers compared to that in the IM7 composites (Figure 3.5 and Figure 3.6), which indicates that the hollow fiber surface treatment and sizing processes need to be further optimized. Even in IM7 composites, the debonding between fiber and epoxy matrix is visible (Figure 6(b)), although it is significantly better compared to hollow CF composites. This is likely because the commercially produced IM7 fibers have optimized surface treatment and sizing processes in place.

The fiber orientation factor in both hollow CF and IM7 composite specimens is also lower than the inherent fiber structural orientation, which is contributing to lower tensile moduli in both hollow CF and IM7 composites. In hollow CF composites, the fiber tow had significantly higher number of broken fiber filaments, and there are significantly higher number of misaligned fibers in these composites compared to IM7 (Figures B.2 and B.3). The fiber orientation in the uniaxial direction could be improved by improving the prepreg manufacturing process. Although drum winding is convenient for small-scale prepreg manufacturing, but it could be potentially causing misalignment in adjacent fibers. Commercial prepreg manufacturing methods are likely to yield better control over fiber alignment in the composite.

At room temperature, hollow CF composite compressive strength is 81% of the tensile strength. For IM7 composites, based on compression and tension values reported in the literature (Table 3.4), the compressive strength is only 60% of the tensile strength of the composite. For GT gel spun carbon fiber composites where the compressive strength was measured to be 55% of the tensile strength. Additionally, the SEM image of fractured surface of the room temperature hollow CF specimen post compression shows no signs of

micro-buckling (Figure 3.7). Therefore, although the compressive strength of the hollow CF composites is currently lower than IM7 composites, it is likely to improve upon further improvement in hollow CF mechanical properties.

It is important to note that the compressive strength values for IM7 composites at both room temperature and 180 °F are likely significantly underestimated because all the samples in these tests experienced end-crushing and did not fail in the intended gauge length. The same was observed for hollow CF composite tested at 180 °F. This is caused due to potential misalignment of the tabs while being bonded to the composite, issues with flatness of the loading surface and the composite misalignment in the support fixture. Due to the limited composite material available, further tests could not be conducted to measure the true compressive strength of these specimen.

Table 3.6 Fiber alignment in composites

Composite	Orientation factor (f)	
	Individual fiber	Composite
Hollow CF	0.82 (Chapter 2)	0.7
IM7	0.83 [6]	0.73

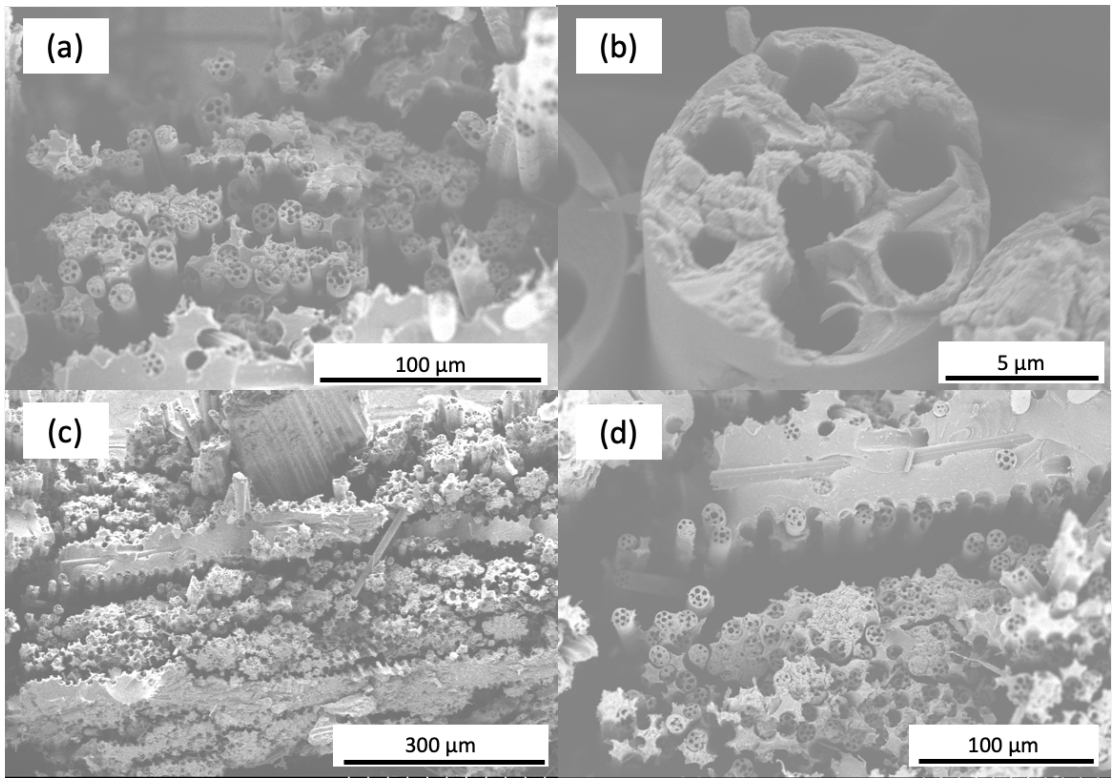

Figure 3.3 SEM of fractured hollow CF composite after tension test at room temperature (27 ºC)

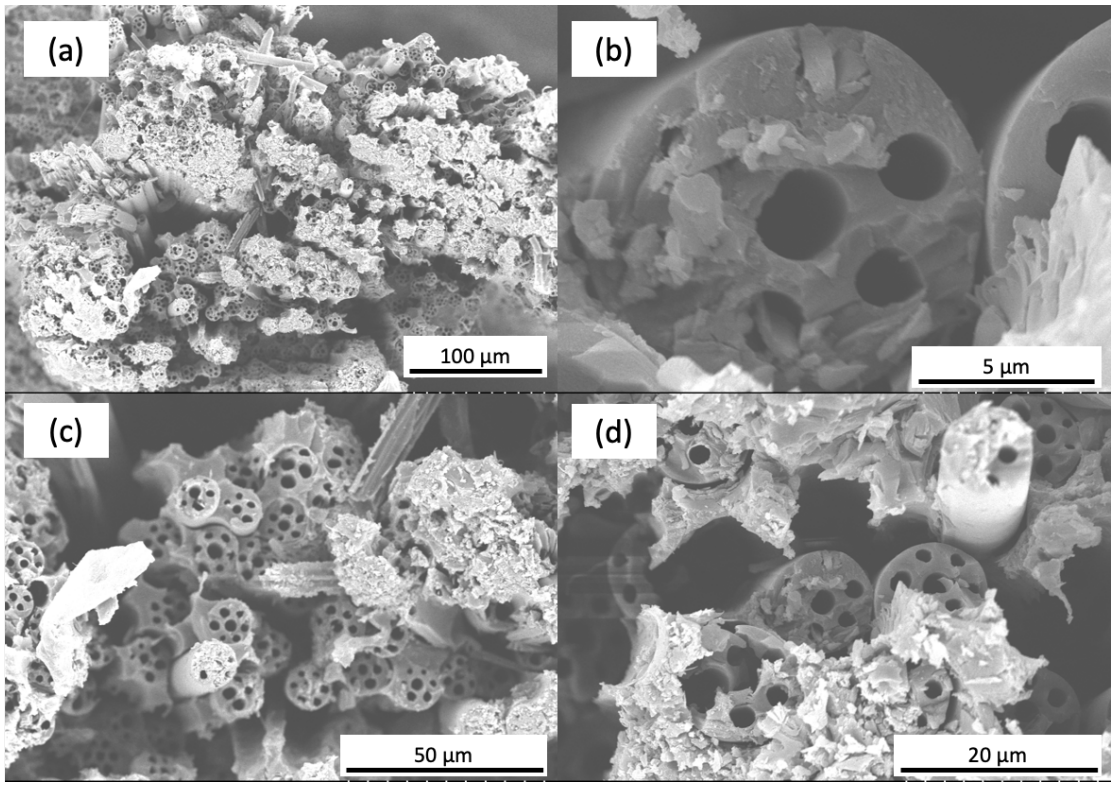

Figure 3.4 SEM of fractured hollow CF specimen after tension test at -75 ºF (-59 ºC)

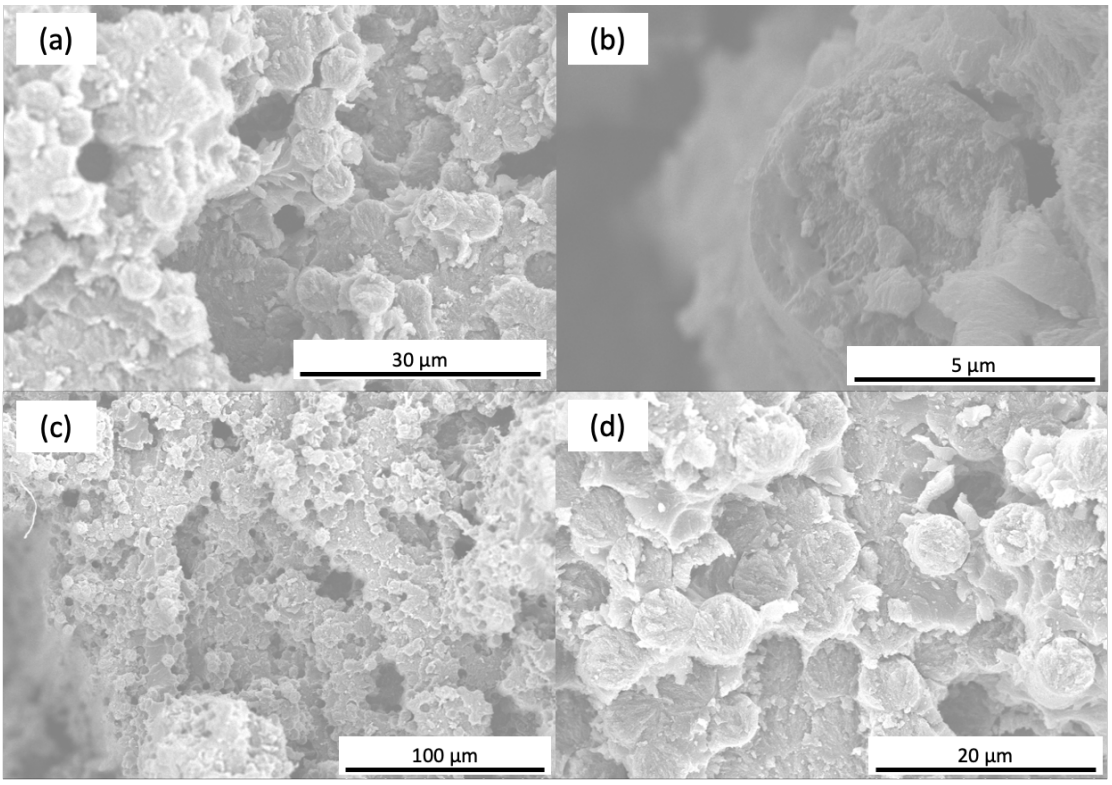

Figure 3.5 SEM of fractured IM7 composite specimen after tension test at room temperature (27 ºC)

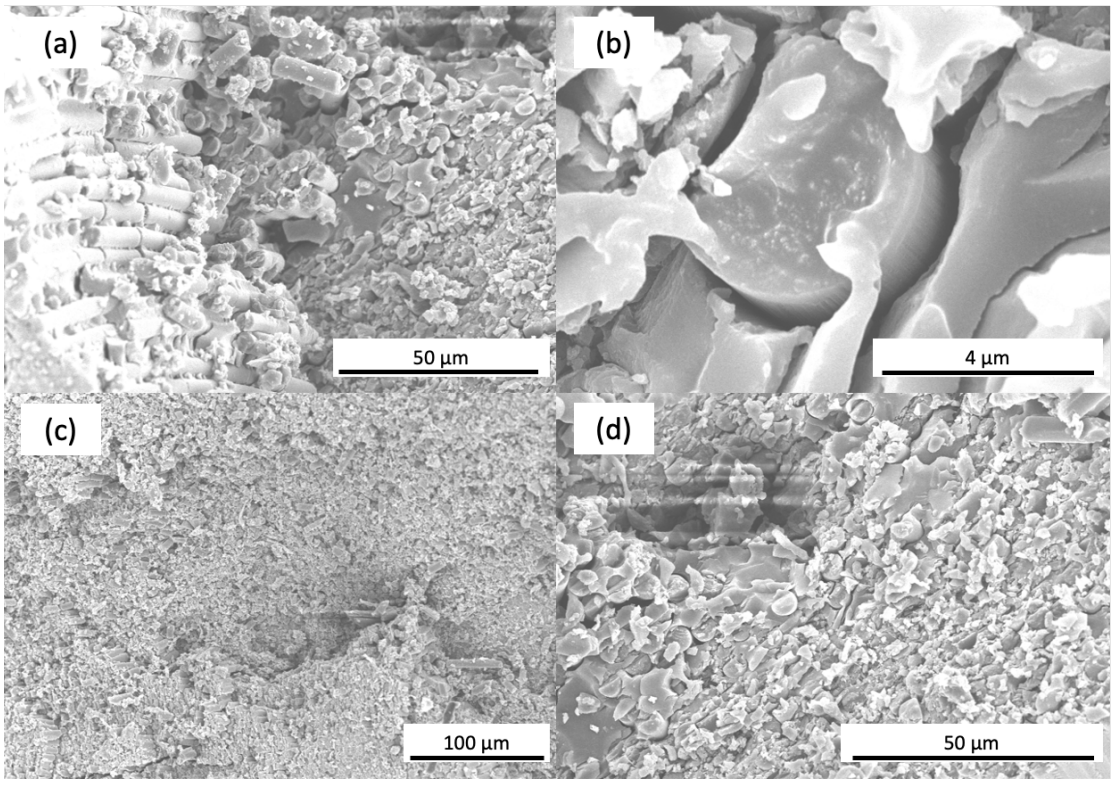

Figure 3.6 SEM of fractured IM7 composite after tension test at -75 ºF (-59 ºC)

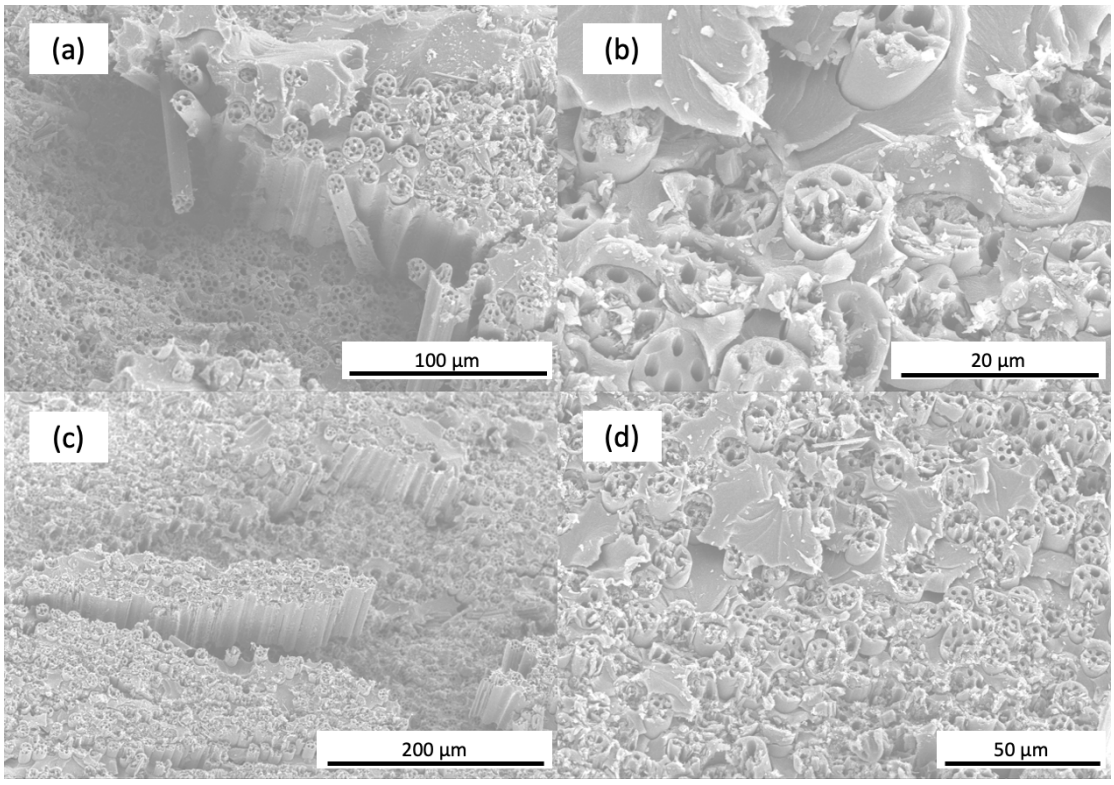

Figure 3.7 SEM of fractured hollow CF specimen after compression at room temperature shows compressive failure with no signs of micro-buckling in the fibers

3.8 Summary

Tension and compression properties of Hollow CF and IM7 composite specimen were measured. The lower tensile properties of the hollow carbon fiber composites compared to IM7 composites are attributed to the difference in fiber tensile properties, poor adhesion between fiber and epoxy matrix and the fiber alignment in the composites. The adhesion between epoxy and fiber is expected to improve upon optimizing the surface treatment and sizing conditions and improve the tensile strength of the composite by facilitating effective load transfer among fibers. Compression strength of the hollow CF composites being 81% of the tensile strength as well as the absence of moisture pickup in the hollow channels is

a very promising step towards advancing the technology readiness level. By comparison, compressive strength of IM7 composite is only 60% of the tensile strength.

CHAPTER 4. SMALL DIAMETER CARBON FIBERS

4.1 Background

Fiber diameter is known to affect the tensile strength and modulus of carbon fibers [46, 65, 87]. There are multiple theories as to the mechanism of this relationship [76, 87-93]. It is generally understood that defects limit the tensile strength of carbon fibers. Reducing the fiber diameter is expected to limit the size and number of defects formed, and as a result improve the tensile strength of the fiber. The formation of a skin-core structure in carbon fibers has been discussed in CHAPTER 1. Carbon fibers with smaller diameters have a higher surface area to volume ratio which helps diminish the skin-core structure effect caused due to oxygen diffusion and heat transfer gradients during the oxidation and stabilization process [93]. It has been hypothesized that the diminishing skin-core effect helps improve the graphitic ordering throughout the cross-section of the fiber and was believed to be the one of the reason behind the improvement in the tensile modulus of hollow carbon fibers by 20-30% compared to commercially produced IM7 carbon fibers [29]. Therefore, reducing the diameter could, potentially, further improve the tensile modulus of carbon fibers.

Commercially produced PAN based carbon fiber diameter is in the range of 5 –7 μm. The PAN precursor fibers are solution spun and the diameter of the as-spun and drawn precursor fiber largely determines the diameter of the carbon fiber. The as-spun PAN fiber diameter is dependent on the spinneret hole size. Although manufacturing spinnerets with hole sizes less than 100 μm with the desired L/D ratio is possible, it requires high level of

precision. Alternatively, small diameter fibers can be produced using a bicomponent islands in a sea system, with small diameter islands of the desired fiber material and a sacrificial sea component that can be eliminated in subsequent processing, producing a multifilament tow of small diameter fibers [94].

Another method of producing small diameter PAN fibers is via electrospinning. Carbon fibers with diameter in the submicron range have been produced from electrospun PAN precursors. Arshad et al. [92] produced electrospun PAN based carbon fibers with diameter between 150-500 nm with a tensile strength of 3.5 GPa and tensile modulus of 172 GPa. The PAN fibers were collected in the form of a unidirectional net and were stabilized and carbonized under tension. However, in the absence of further drawing of the electrospun fibers, and continuous and gradual application of tension as in case of continuous stabilization and carbonization, the tensile modulus of these fibers was limited to 172 GPa. In comparison, the commercially produced T300 fiber has a tensile strength of 3.5 GPa and a tensile modulus of 230 GPa. Therefore, the tensile properties of the small diameter carbon fibers produced from electrospun PAN precursors would need to improve in order to scale up and manufacture aerospace grade carbon fibers using this method. It is also challenging to produce continuous fibers with a uniform diameter using electrospinning, as observed in this case where the carbon fiber diameter was in the range of 150-500 nm.

Bicomponent fiber spinning for manufacturing a variety of fibers has been used since the 1960s. Chae et al. [27] have demonstrated the use of the gel spun, bicomponent, islands in a sea precursor with PAN islands in a polymethylmethacrylate (PMMA) sea.

PMMA acts as the sacrificial component and burns out during carbonization, producing small diameter carbon fibers. The carbon fibers produced using this method had an effective diameter of 1 μm, tensile strength of 3.2 GPa, and tensile modulus of 337 GPa. Stabilization and carbonization was done in a batch process.

Based on the reported tensile properties for PAN based carbon fibers and the corresponding fiber diameters, Chang et al. [65] predicted that reducing the diameter of the gel-spun PAN based carbon fibers to 1 μm could result in tensile strength as high as 12 GPa and tensile modulus of up to 425 GPa. With this thought, multifilament bicomponent PAN:PMMA precursor fibers were produced. These precursor fibers were continuously stabilized and carbonized to produce a continuous 700 filament carbon fiber tow with 2.3 μm carbon fiber diameter. This study focuses on the process, structure and properties of these small diameter carbon fibers and provides insights to further improve the tensile strength.

4.2 Materials

A poly(acrylonitrile-co-methacrylic acid) (PAN-co-MAA) copolymer with a viscosity average molecular weight of approximately 500,000 g/mol was used as the precursor polymer (Japan Exlan Company, Osaka, Japan). PMMA homopolymer with a molecular weight of approximately 350,000 g/mol was obtained from Sigma Aldrich. N,N dimethylformamide (DMF) (HPLC grade), obtained from Sigma Aldrich, was used as the solvent. Methanol used in the coagulation bath was obtained from VWR. SF-LUROL CF-14676 from Goulston Technologies, North Carolina was used as the spin finish.

4.3 Precursor and Carbon Fiber Processing

The fiber spinning equipment, manufactured by Hills Inc, Melbourne, Florida, consisted of two solution tanks, one for the PAN solution that would form the islands component, and the other for the PMMA solution that would form the sea component in the fiber. The PAN solids content in the solution was 11g /100 mL of DMF, and the PMMA content was 29 g/dL. A 20-hole spinneret was used for gel spinning of the bicomponent fibers. Each hole had a diameter of 200 μm and an L/D ratio of 5. The air gap between the spinneret and the coagulation bath was maintained at 19 mm. A single coagulation bath (100% methanol) at -50 °C was used for gelation. A spin draw ratio (SDR) of 2.3 was used to collect the as-spun fiber. Each filament of the as-spun fiber had seven PAN islands in a PMMA sea. Five such as-spun fiber spools were combined during the multistage drawing process to obtain a 100 filament bicomponent precursor tow. Spin finish was applied during the drawing process. The total draw ratio is defined as the total stretch ratio applied during fiber spinning and drawing. In this study, we report on two precursor trials viz. A1 and A2. The precursor fiber spool was then stabilized and carbonized using the continuous stabilization and carbonization line, built by Harper International, to obtain a carbon fiber tow with 700 filaments (7 PAN islands/precursor filament x 100 filament precursor). The stabilization and carbonization conditions are listed in Table 4.4 Summary of continuous stabilization and carbonization processing parameters All the facilities used for precursor and carbon fiber processing are housed in class 1000 clean rooms as depicted in Figure A.2. In total, over 20 carbonization trials were conducted and the results from eight of these trials are discussed in this chapter.

4.4 Characterization

4.4.1 Precursor characterization

Rheological behavior of the solutions was studied using a parallel plate viscometer (ARES, TA Instruments Inc.). Dynamic frequency sweep was carried out using 50 mm plates with a gap of 1 mm at room temperature at a strain of 1%. Tensile strength of the PAN-PMMA bicomponent precursor filaments was tested using a single filament testing machine (FAVIMAT+, Measured Solutions Inc.), using the testing protocol described by Lyon et al [69]. Optical micrographs of the bicomponent precursor fiber tow cross section were captured using a Leica optical microscope. The PAN island fibers were separated from the bicomponent precursor by removing PMMA using methylethylketone (MEK), and tested using the FAVIMAT to measure the tensile strength and modulus of the individual PAN island fibers. The strain rate and gauge length used for precursor tensile testing, for bicomponent as well as PAN island fiber, was 0.01/s and 25.4 mm, respectively.

4.4.2 Carbon fiber characterization

The Scanning electron microscope (SEM) used to capture carbon fiber cross sections was Hitachi SU8230 at an accelerating voltage of 5 kV. Individual fiber cross-section areas were measured using ImageJ for every trial and at least 25 images were used to calculate the average diameter of the fibers. Individual carbon fiber filaments with 12.7 mm gauge length were mounted on paper tabs and were tensile tested using an RSA III solids analyzer at a strain rate of 0.1%/s. The tensile moduli values were compliance corrected as described in 2.4.2, using the correction factor obtained from Figure A.3.

Wide-Angle X-ray diffraction (WAXD) was used to characterize the structure of the bicomponent precursor and carbon fibers. WAXD of the fibers was carried out using Rigaku Micromax– 007 (Cu K_α, λ = 1.542 A°, 0.65 mA, 45 kV). X-Ray exposure time was 30 min for each sample. The diffraction patterns were analyzed using AreaMax and MDI Jade 9.1 software. From the WAXD patterns of carbon fibers, crystallite size L_{002} and L_{100} was calculated using Scherrer equation with K = 0.9 [70]. The orientation factor was determined from the (002) azimuthal scans at 2θ=17° for precursor, and 2θ=26° for carbon fibers using the procedure previously described by Sreekumar et al. [71]. Raman spectra were collected on a Horiba Scientific Xplora confocal micro-Raman system (laser wavelength = 785 nm).

For the transmission electron microscopy (TEM), samples were prepared using dual-beam Thermofisher Scientific Helios G4 UC FIB/SEM. Carbon fibers were fixed with diluted resin on the substrate and a 1μm thick Pt protection layer was deposited perpendicular to the fiber axis. Thin lamellae were in-situ lifted out using a manipulator and mounted on the TEM grid. Additional thinning was performed at 5 kV for TEM observation. High resolution TEM images were taken using the JEOL JEM-ARM200cF with an accelerating voltage of either 80 kV or 200 kV. The 3D internal microstructure of the carbon fiber was resolved using transmission x-ray microscopy (nano-CT) at beamline 18-ID located at National Synchrotron Light Source II in Brookhaven National Laboratory. One fiber each from trial A1 and A2 was imaged at 8 keV to obtain an isotropic voxel size of 20 nm. Tomography scans were done in the fly scan mode in which a sample is continuously rotated, and the sample's X-ray projection images are continuously acquired by a lens-coupled Andor Neo5.5 camera at the same time. The exposure time for a single

projection image was 0.05 sec, and the sample rotation velocity was 6 deg/sec. Sample images were acquired in 180º rotation range.

4.5 Results and Discussion

An optical micrograph of the as-spun bicomponent fiber tow from trial A1 is shown in Figure 4.1. A SEM image of the draw precursor is shown in Figure 4.2. These images show a non-uniform cross section for the PAN islands in the bicomponent precursor. From Figure 4.1, it is evident that the cross-sectional non-uniformity is introduced when the bicomponent fiber is being spun. The shape of the bicomponent solution-spun fiber cross-section is affected by several factors including coagulation bath composition and temperature, the viscosities and composition of sea and island polymer solutions [95, 96]. As shown in CHAPTER 2, the hollow carbon fiber precursors (T1-T5) with PAN sea and PMMA islands had a circular cross-section. It is important to note the differences in the solution spinning parameters between the hollow carbon fiber and small diameter precursors. The solvent used for the hollow carbon fiber precursor was DMAc while the solvent used in the current study is DMF. For the hollow carbon fiber precursor, two coagulation baths were used (Methanol/DMAc and Methanol) and maintained at room temperature. In the current study, only a single methanol bath at -50 °C was used. As described earlier in this thesis, the coagulation conditions also play an important role in determining the fiber geometry. The coagulation bath composition and temperature is known to affect the fiber cross-sectional shape [74]. Let us consider the viscosity of the sea and island solutions in both cases. Solution viscosities of PAN and PMMA are summarized in Table 4.1. In trial A1 and A2, the PAN solution viscosity was 52 and 54 Pa.s,

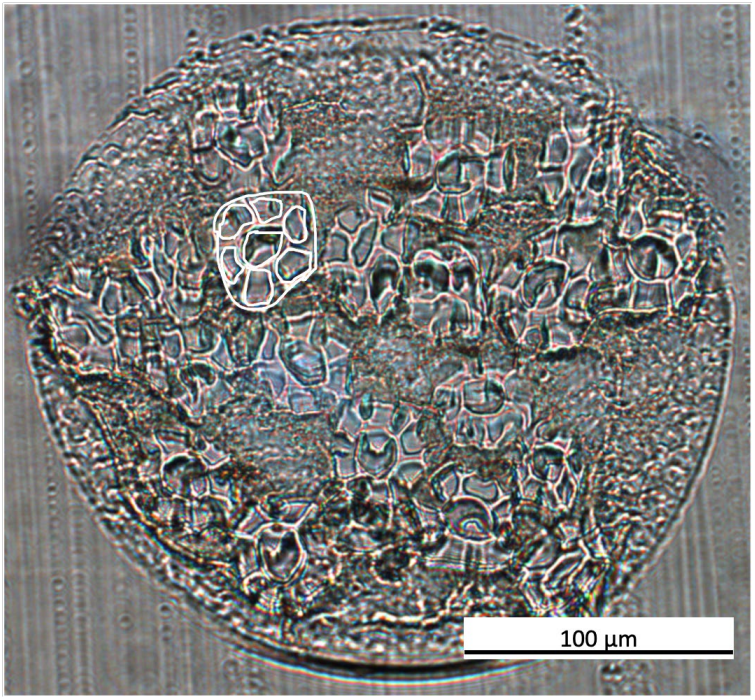

Figure 4.1 Optical micrograph of 20-filament as-spun bicomponent precursor fiber from trial A1. PAN islands in the PMMA sea have a non-uniform cross-section. A representative bicomponent fiber has been highlighted with a white outline to provide readers with a better understanding of the cross-section.

respectively. The PMMA solution viscosity in trial A1 and A2 was 176 and 184 Pa.s, respectively. The PMMA solution viscosity is over three times higher compared to PAN solution viscosity. For the hollow carbon fiber precursors, the PAN solution viscosity was in the range of 50-65 Pa.s for different trials while the PMMA viscosity was between 350-400 Pa.s It has been reported that in bicomponent spinning (both melt and solution spinning), the higher viscosity polymer tends to form the core component and the lower viscosity component tends to form the sheath component [97, 98]. The viscosity of the PAN and PMMA solutions could be changed by changing the solution concentration as well as polymer molecular weight. Overall, this suggests that the effect of PAN and PMMA

solution spinning parameters on the bicomponent fiber geometry needs to be studied further to obtain a uniform circular island diameter.

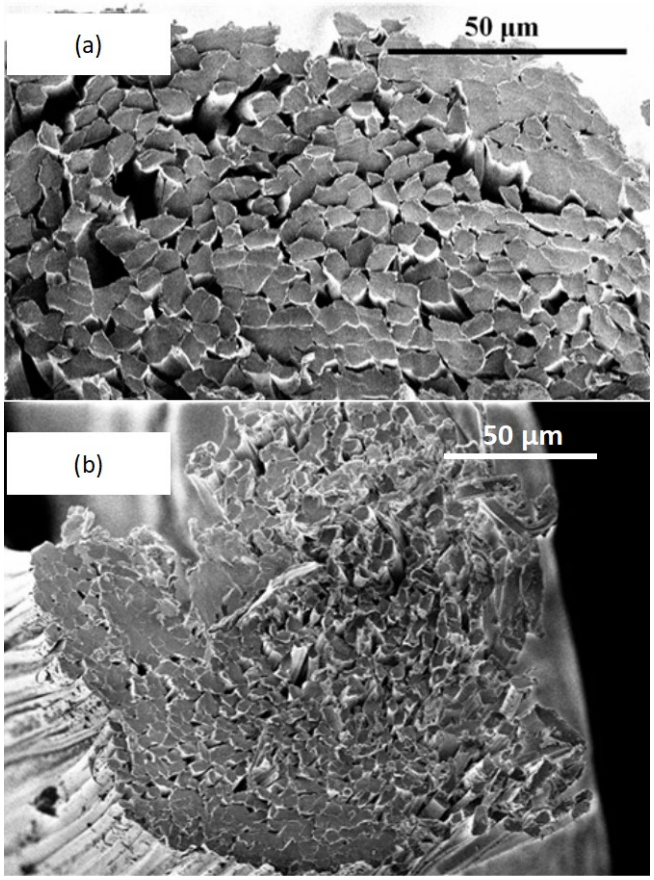

Figure 4.2 SEM images of (a) magnified part of the cross-section of the drawn precursor fiber from trial A1 shows non-uniform PAN island diameters, (b) precursor tow at a lower magnification showing majority of the precursor tow.

Table 4.1 Solution rheology – zero shear viscosity at room temperature

Trial #	Solution viscosity (Pa.s)	
	PAN	PMMA
A1	54	176
A2	52	184

Tensile properties of the drawn precursor and that of a single component gel spun PAN precursor are summarized in Table 4.2. Structural parameters of the bicomponent precursors from WAXD are summarized in Table 4.3. The tensile modulus of the bicomponent precursor is lower than that of the control PAN precursor. This could be attributed to two factors: 1) the tensile modulus of PMMA is lower (2.9 GPa) compared to PAN fiber tensile modulus (10-21 GPa), and 2) the bicomponent precursor had a total draw ratio of 15.9 in trial A1 and 10.8 in trial A2, compared to a draw ratio of 24 for the control PAN precursor. Even the PAN island fibers tested after removing PMMA had a tensile modulus of 14 GPa and 12 GPa in trial A1 and A2, respectively. This means that the PAN fibers in the bicomponent precursor were drawn less compared to the control PAN precursor, resulting in lower polymer chain alignment in the fiber direction, and therefore, have a lower tensile modulus. The tensile modulus of PAN islands is similar to what was observed for hollow carbon fiber precursor in CHAPTER 2. The orientation factor of the precursor A1 (0.83) and A2 (0.82) from WAXD (Table 4.3) is also similar to what was observed for the hollow carbon fiber precursor (0.81-0.83).

Table 4.2 Precursor fiber drawing conditions and tensile properties

Trial #	Spin Draw Ratio (SDR)	Post Spin Draw Ratio (PSDR)	Total Draw Ratio (TDR)	Fiber Diameter (μm)	Tensile Strength (GPa)	Tensile Modulus (GPa)
A1	4.3	3.7	15.9	17.6 ± 1.7	0.4 ± 0.19	9.5 ± 0.2
A2	3.0	3.6	10.8	28.8 ± 4.6	0.4 ± 0.04	9.4 ± 1.1
GT control PAN [6]	3.0	8.2	24.6	11.0 ± 0.8	1 ± 0.1	20.7 ± 1.1

Table 4.3 Precursor PAN fiber structural parameters from WAXD

Trial #	$L_{(200, 110)}$ (nm)	$d_{17°}/d_{30°}$ (equatorial)	$f_{200, Azi}$
A1	11.82	1.74	0.83
A2	11.95	1.73	0.82

The continuous stabilization and carbonization parameters are summarized in Table 4.4. The precursors from trials A1and A2 were each stabilized and carbonized under four different conditions. For A1 precursor, the stabilization temperature profile was in the range of 180-250 ºC, stabilization residence time was 118 min. Low temperature (LT) carbonization temperature profile was 500-675 ºC and the high temperature carbonization temperature was varied between 1200-1400 ºC. The LT carbonization strain was between 10-20%, and the HT carbonization strain was maintained at -5%. For A2 precursor, the stabilization residence times were varied between 60-120 min, stabilization strain between 6-28%. The LT carbonization temperature profile and strain were kept constant at 500-675 ºC and 10%, respectively. The HT carbonization temperature was maintained at 1400 ºC.

Table 4.4 Summary of continuous stabilization and carbonization processing parameters

Trial #	Stabilization			LT carbonization		HT carbonization		Total Carbonization Time (min)
	Residence Time (min)	Strain (%)	Temperature (°C)	Strain (%)	Temperature (°C)	Strain (%)	Temperature (°C)	
A1-1	118	6	180-250	10	500-675	-5.0	1200	13
A1-2	118	6.4	180-250	10	500-675	-5.0	1300	13
A1-3	118	6	180-250	10	500-675	-5.0	1400	13
A1-4	118	6	180-250	20	500-675	-5.0	1400	11
A2-1	118	6.4	180-250	10	500-675	-5.0	1400	12
A2-2	121	15.6	200-260	10	500-675	-4.1	1400	13
A2-3	77	23.0	200-260	10	500-675	-4.1	1400	7
A2-4	94	27.7	200-260	10	500-675	-4.1	1400	9

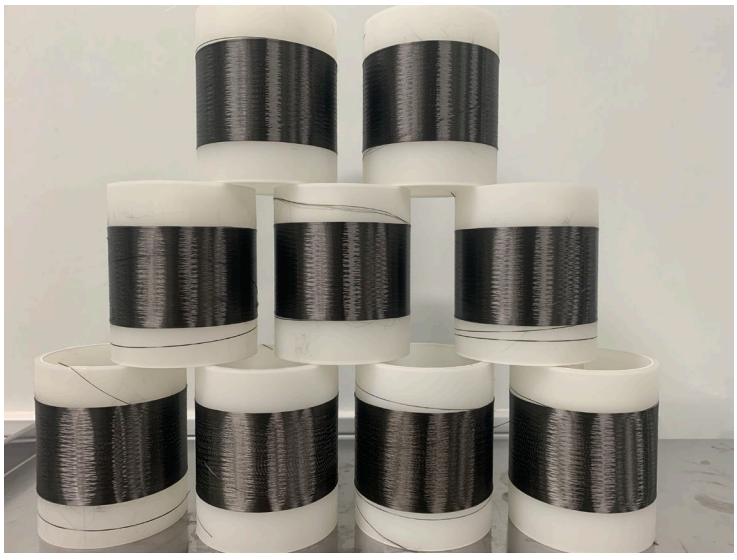

Figure 4.3 Small diameter carbon fiber spools produced in trials A1 and A2. Over 20 carbonization trials were conducted and spools from nine trials are shown in the image.

The 700 filament carbon fiber spools produced in trials A1 and A2 are shown in Figure 4.3. The carbon fiber diameter and tensile properties resulting from these stabilization and carbonization conditions are summarized in Table 4.5. The SEM images of the fiber cross section and fiber surface are shown in Figure 4.4. The carbon fiber diameter is in the range of 2.2-2.6 μm. The highest tensile strength of 5.1 GPa was observed in trial A1-3 and the highest tensile modulus of 434 GPa was observed in trial A2-1. The tensile moduli values are in the range of 358 – 434 GPa for all but one trial. In trial A1-1 the HT carbonization temperature was 1200 ºC. As the temperature was increased to 1300 and 1400 ºC, a significant improvement in the tensile modulus is observed.

Table 4.5 Summary of tensile properties of continuous small diameter carbon fibers

Trial #	Fiber diameter (μm)	Tensile strength (GPa)	Tensile modulus (GPa)	Strain to failure (%)
A1-1	2.2	4.0 ± 1.1	274 ± 34	1.4 ± 0.1
A1-2	2.2	4.8 ± 1.5	383 ± 87	1.3 ± 0.1
A1-3	2.2	5.1 ± 0.7	358 ± 29	1.4 ± 0.1
A1-4	2.2	5.0 ± 0.9	363 ± 47	1.4 ± 0.1
A2-1	2.6	4.2 ± 1.0	434 ± 75	1.1 ± 0.1
A2-2	2.6	3.9 ± 1.0	417 ± 77	1.1 ± 0.1
A2-3	2.5	4.1 ± 0.8	384 ± 59	1.1 ± 0.1
A2-4	2.4	4.0 ± 1.0	376 ± 64	1.1 ± 0.1
GT control CF	5.5	5.5	300-375	1.1-1.4

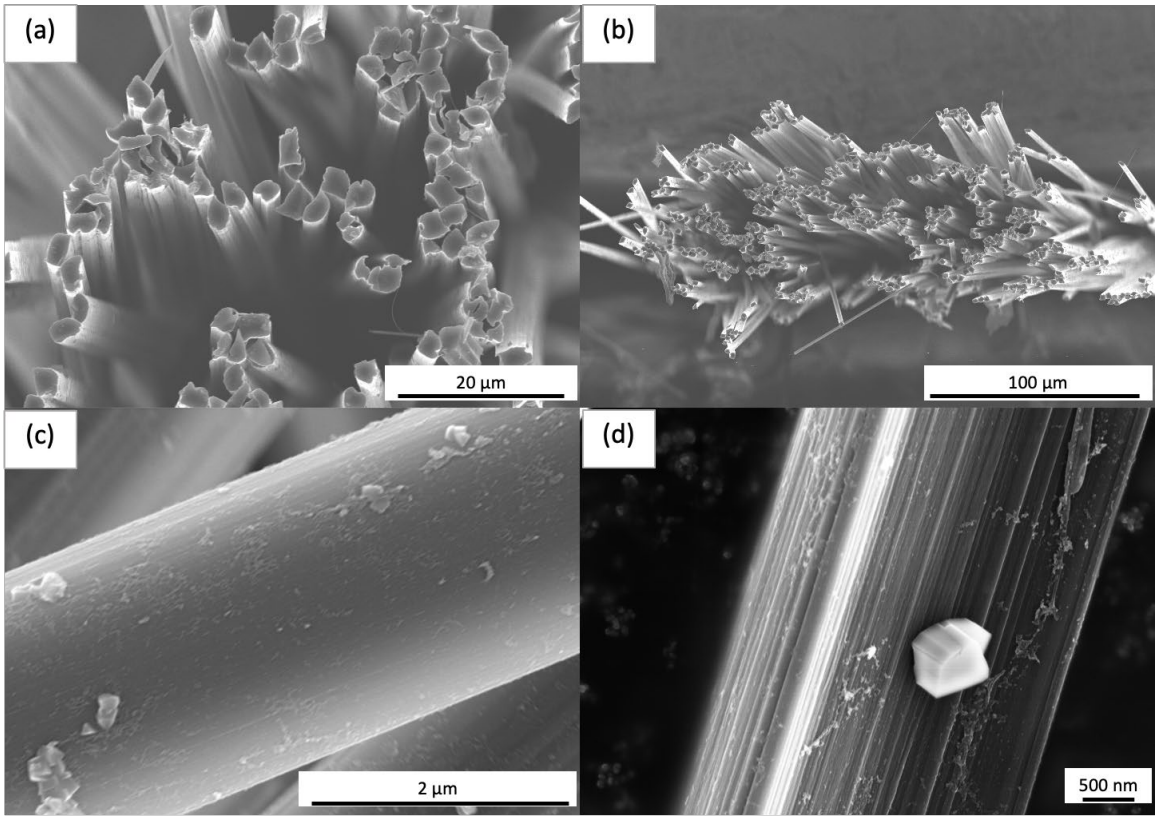

Figure 4.4 SEM image of (a) Representative cross-section of the carbon fiber from trial A2-3 (b) part of the 700 filament carbon fiber tow from A2-3 (c) carbon fiber surface showing flake-like features (d) magnified image of a surface feature larger than 500 nm in size.

The tensile moduli values are 29-57% higher compared to the IM7 carbon fiber which has a tensile modulus of 276 GPa. It is important to note that the tensile modulus of the carbon fiber is comparable or higher than that reported for the control gel spun PAN based carbon fibers (300-375 GPa) despite having a precursor with lower tensile modulus than the control PAN precursor. This is attributed to the smaller diameter of the carbon fibers (2.2-2.6 µm) compared to the control carbon fibers (5.5 µm). It is important to note that PMMA does not degrade during the stabilization stage as shown in CHAPTER 2. However, the PAN island fibers have a smaller diameter compared to the control PAN precursor. The smaller diameter leads to a higher surface area to volume ratio. This likely

results in a diminishing skin-core effect due to better oxygen diffusion and heat transfer during stabilization. This could result in a more homogeneous structure throughout the fiber during stabilization and carbonization. The structural parameters of the carbon fibers are summarized in Table 4.6. Raman spectroscopy measurements show significantly higher I_G/I_D ratio in these small diameter carbon fibers (0.72) compared to the control carbon fibers (0.46) and IM7 carbon fiber (0.43) and hollow carbon fibers (0.49-0.53). Recent studies on characterizing carbon fibers using Raman spectroscopy have shown a correlation between a high I_G/I_D ratio and high tensile modulus of the carbon fibers [99, 100]. WAXD analysis of the carbon fibers show that the FWHM for the continuous small diameter carbon fibers is lower than the batch processed carbon fibers and is higher than the control and IM7 carbon fibers. The fiber orientation factor for the small diameter carbon fibers is comparable to that of IM7 fibers but is higher than the batch processed carbon fibers. This is likely due to the fact that continuous processing allows better control over the application of strain during carbonization, leading to higher alignment of the graphitic planes in the carbon fiber. These factors could be contributing to the higher tensile modulus of the small diameter carbon fibers.

The tensile strength of 5.1 GPa shows a 57% improvement compared to the batch processed small diameter carbon fiber strength of 3.2 GPa reported by Chae et al. [27]. The tensile strength of the carbon fibers is limited by the defect size. Using Griffith's equation for brittle fracture, the defect size has been calculated for the corresponding tensile strength and moduli values, as shown in Table 4.7.

Table 4.6 Summary of structural parameters of continuous small diameter carbon fibers

Trial #	L_{002} (nm)	L_{10} (nm)	$d_{(002)}$ (Å)	$FWHM_{Azi, 002}$ (°)	$f_{(002), azi}$	Raman I_G/I_D
Trial A1-3	1.6	2.1	3.42	31.9	0.81	0.72
Trial A2-1	1.7	2.1	3.46	31.1	0.82	0.72
Batch carbonized small diameter fiber [27]	1.3	1.8	3.57	37.3	0.73	N/A
GT control carbon fibers [6]	1.9	2.5	3.44	23.1	N/A	0.46
IM7 [6]	1.6	2.1	3.48	30.3	0.83	0.43

Table 4.7 Carbon fiber defect size calculation from Griffith's equation

Trial #	Tensile strength (GPa)	Tensile modulus (GPa)	Size of largest defect (nm)
A1-1	4.0	274	45
A1-2	4.8	383	44
A1-3	5.1	358	37
A1-4	5.0	363	39
A2-1	4.2	434	66
A2-2	3.9	417	73
A2-3	4.1	384	61
A2-4	4.0	376	63

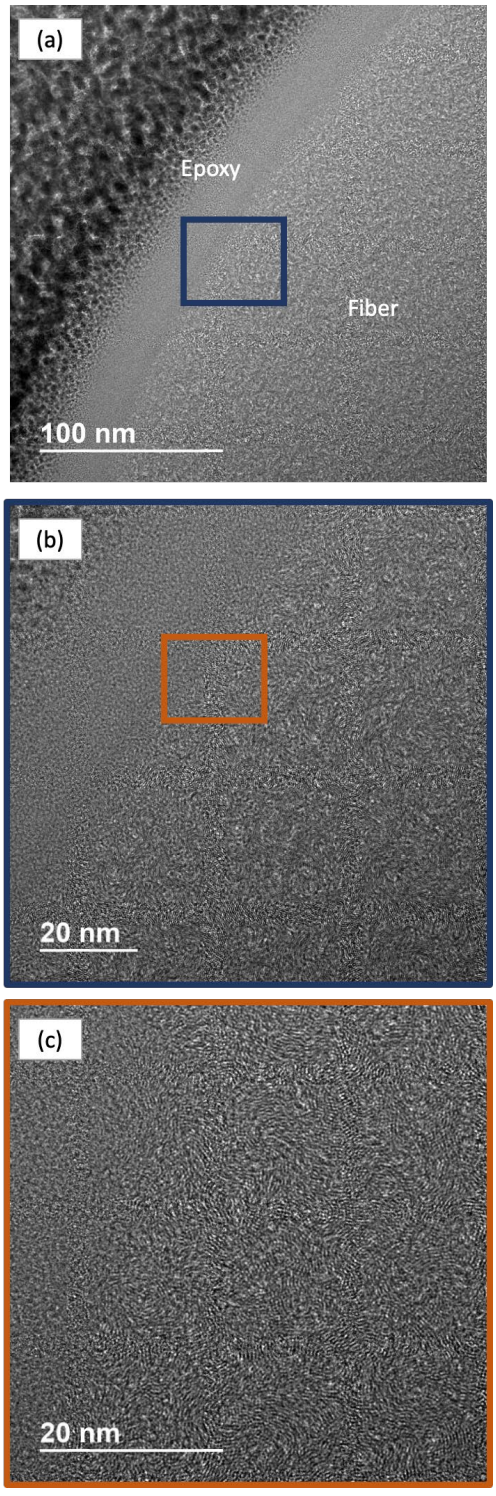

Figure 4.5 TEM image of the carbon fiber cross-section near the fiber surface. There are no defects near the surface of the fiber.

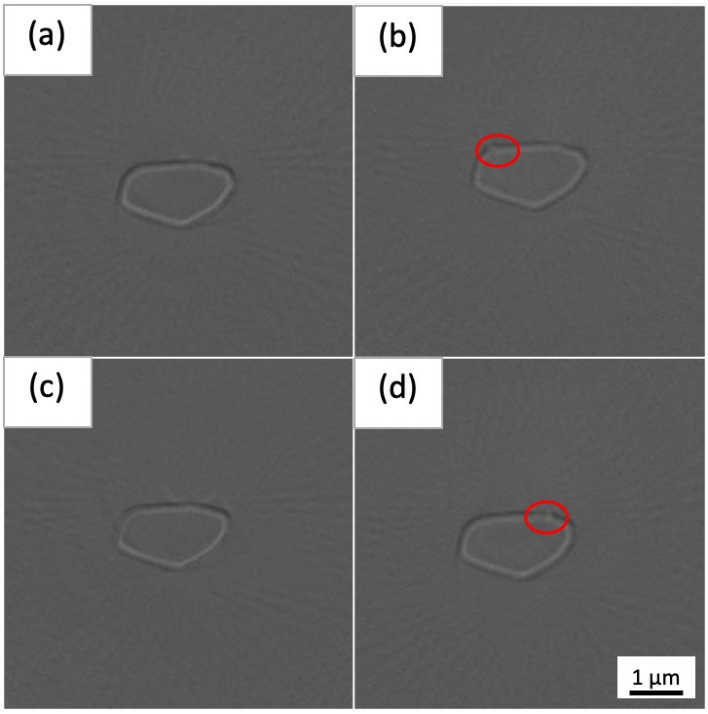

Figure 4.6 Carbon fiber cross-sections imaged using nano-CT at four different locations along the length of a 10 µm carbon filament, each 1 µm apart. Minor changes in the cross-sectional shape near the surface (circled red) are observed and need to be resolved further.

The size of the largest defect is estimated to be in the range of 37-66 nm for these carbon fibers. Figure 2.9 shows the presence of defects 10-20 nm defects near the surface of the control carbon fibers. These defects are seen in the 40 nm region from the surface of the fiber into the cross section. In contrast, TEM images of the carbon fiber cross-section from trial A2-3, shown in Figure 4.5, do not show any defects near the surface of the fibers that were imaged. The nano-CT images shown in Figure 4.6, of fiber cross-sections at different points along the length of the fiber, with a 20 nm voxel size do not resolve any larger defects in the fiber. The minor shape changes near the surface of the fibers could be due to a non-uniform cross-section along the length of the fiber, however, this needs to be investigated further. SEM images of the surface of the carbon fiber (Figure 4.4c and 4.4d), reveal flake like features on the fiber surface. Some of these features are larger than 200

nm. However, these features were not observed in the nano-CT images. Further investigation using the combination of TEM and nano-CT is necessary to develop a better understanding of the defect size and shape in these small diameter fibers.

4.6 Conclusion

Continuous 700-filament carbon fiber tows were successfully manufactured using a bicomponent PAN:PMMA precursor. The diameter of the carbon fiber was in the range of 2.2-2.6 μm. The cross section of the PAN islands could be made circular and more uniform by further studying the effect of PAN and PMMA solution spinning parameters, however, this is yet to be demonstrated. Tensile strength of the carbon fibers is up to 5.1 GPa, a 57% improvement compared to the corresponding batch processed carbon fibers. The tensile modulus of the carbon fibers is 29-57% higher compared to the IM7 carbon fibers. The higher tensile modulus is likely due to higher level of graphitic ordering throughout the fiber, evidenced by the higher I_G/I_D ratio in the small diameter fibers compared to IM7 and control carbon fibers. Limited carbon fiber TEM images do not show any defects near the surface of the fibers, however, larger surface features observed in the SEM images could be limiting the tensile strength of these fibers. Optimization of precursor processing and stabilization and carbonization parameters will likely improve the tensile strength further. The successful manufacturing of continuous small diameter carbon fiber tows is a promising step towards increasing the carbon fiber tensile strength beyond 7 GPa.

CHAPTER 5. MACHINE LEARNING IN CARBON FIBER MANUFACTURING

This chapter is adapted from a publication in Carbon.

Shirolkar et al., *Investigating the efficacy of machine learning tools in modeling the continuous stabilization and carbonization process and predicting carbon fiber properties.* Carbon, 174 (2021): 605-616.

5.1 Background

The full extent of mechanical performance, and hence implementation and potential weight savings, achieved by using carbon fiber composites is yet to be realized. Carbon fiber manufacturing is a time- and cost-intensive process with more than 70 processing variables at play. Machine learning (ML) techniques can be employed to understand the effect of manufacturing processing parameters on the structure and, in turn, the mechanical properties of the carbon fibers. The integration of these approaches with experimental trials can lead to significant time and cost savings while accelerating the development of next generation carbon fibers.

ML based approaches have been demonstrated to be effective in accelerating materials design. For example, Liu et al. [101] proposed the use of ML to find optimal microstructures in Fe-Ga alloys to achieve target magnetoelastic properties. A dataset of 145,000 samples was generated randomly. ML techniques were shown to provide a balance between accuracy, time efficiency, and solution completeness while outperforming the

traditional optimization algorithms and generalized pattern search methods. Fujimura et al. [102] used ML to predict the high temperature conductivity of Lithium superionic conductors with a wide range of compositions, by combining experimental and theoretical datasets. Wen et al. [103] successfully employed ML to search for optimal compositions for high entropy alloys with high hardness. The results from the ML models were successfully verified by synthesizing new alloys. The new alloys exhibited higher hardness than the best values in the training dataset. ML techniques also have been employed in both manufacturing of carbon fibers and carbon fiber reinforced composites. Qi et al. [104] created a data set of 500 samples for single layer and multi-layer carbon fiber reinforced plastics (CFRP) using finite element method. These data were used to create a correlation model between CFRP, carbon fiber, and matrix properties. The four elastic properties of the carbon fibers were analyzed using a regression tree model. Xiao et al. [105, 106] employed a support vector machine (SVM) in conjunction with improved particle swarm optimization to create a model capable of predicting the carbon fiber properties based on the processing parameters and vice versa. The model was tested with PAN precursor spinning and drawing parameters with a total of 50 data points. Khayyam et al. [107, 108] and Golkarnarenji et al. [109-112] have studied different steps of carbon fiber manufacturing, viz. stabilization and high-temperature carbonization, using a multitude of techniques. These studies have focused on stabilization energy optimization, stabilized PAN fiber property prediction, and establishing a model connecting the processing parameters to the molecular and macroscale physical properties. The techniques used in these studies include support vector regression, artificial neural networks (ANN), genetic algorithms (GA), and traditional Design of Experiment (DOE) approaches. In one study,

support vector regression and ANN models were employed to predict the stabilized fiber tensile properties based on the stabilization parameters and the Fourier Transform Infrared (FTIR) spectra of the stabilized fibers. A total of 37 different conditions were used in the data set. In another study, a 16-sample data set was used to study just one zone of the stabilization process. The goal was to study the energy usage for different stabilization conditions and the resultant density of the oxidized PAN fiber. In another study, 50 samples with different high temperature (HT) carbonization conditions were analyzed using ML. Pruksawan et al. [113] studied the epoxy adhesive strength as a function of resin molecular weight, curing agent molecular weight, curing temperature, and the amine:epoxide ratio. A total of 32 samples were prepared under different conditions. Three supervised algorithms were employed, viz. random forests, elastic net, and gradient boosting. Bayesian optimization was used to determine the maximum adhesive strength for the epoxy from the ML predictions and was achieved experimentally as well. Zhao et al. [114] have employed an ANN and SVM to classify carbon fiber epoxy fabrics made with different fiber tow sizes as well as grams per square meter (gsm) values. A total of 229 experimental data samples were tested for tenacity, and breaking load. The ML algorithms were used to predict the mechanical properties based on the aforementioned parameters. These studies have not addressed the efficacy of ML in 1) modeling the entire carbon fiber manufacturing process, from precursor manufacturing to stabilization and carbonization, and 2) accurately predicting the tensile properties of the carbon fibers based on the process parameters.

The motivation behind the current study is discussed in this paragraph. Chae et al. [6] conducted over 600 continuous stabilization and carbonization trials, and carbon fiber tensile strength and tensile modulus as high as 5.75GPa and 375 GPa, respectively, was

achieved during these trials. The tensile properties improved as modifications were made to the processing parameters in these trials. However, given the large number of processing parameters and the costs associated with manufacturing experiments, the processing parameter changes were driven by the goal of improving the tensile properties of the carbon fibers. The tensile strength is limited by the size of nano-scale defects present in the carbon fibers. These defects can occur due to the inherent polymer entanglements in the PAN precursor, and during manufacturing process. It was hypothesized that if the defects introduced during the fiber manufacturing process were to be eliminated, tensile strength of up to 20 GPa could be achieved for gel-spun PAN based carbon fibers. We, therefore, believe that there is further scope to optimize the processing parameters to close the gap between the current state of the art and the theoretical limit for the tensile properties of PAN based carbon fibers. A non-trivial step toward optimizing process parameters, however, is to construct some kind of mathematical model relating the process parameters to the mechanical properties.

As stated earlier, the entire carbon fiber manufacturing process, starting from PAN precursor fiber manufacturing to stabilization and carbonization, consists of over 70 processing variables. It is extremely time- and cost-intensive to optimize these variables solely using experimental results. In the present study, we leverage existing experimental data on carbon fiber processing and properties and assess the efficacy of different ML models in terms of tensile property prediction. The experimental data set consists of tensile strength and tensile modulus values collected from 600 carbon fiber manufacturing trials, and the 31 manufacturing processing parameters for each of these trials, presenting a unique opportunity to assess ML models using a relatively large and extensive set of data

from experiments. The current study assesses four different ML models in their efficacy in predicting the tensile strength and moduli of carbon fibers. The four types of models (viz., support vector regression, gradient boosted regression tree, multilayer perceptron and recurrent neural network) are commonly used supervised learning tools. As discussed earlier in this section, these models have also been employed for materials design and property prediction problems, and therefore, were chosen for this exploratory study.

5.2 Experimental Methods and Data Acquisition

5.2.1 Carbon Fiber Manufacturing

PAN is the predominantly used precursor for the production of high strength and high modulus carbon fibers. There are two main steps in PAN based carbon fiber manufacturing: 1) PAN precursor fiber manufacturing, and 2) stabilization and carbonization. In the present study, the PAN and PAN-carbon nanotube (CNT) precursor fibers were produced at Georgia Tech using a gel-spinning process as described by Newcomb et al. [74]. The as-spun fibers were then drawn using a multistage drawing process. The PAN precursor fibers were stabilized and carbonized in a continuous process using the carbon fiber line at Georgia Tech. The schematic of the continuous stabilization and carbonization line is depicted in Figure 5.1.

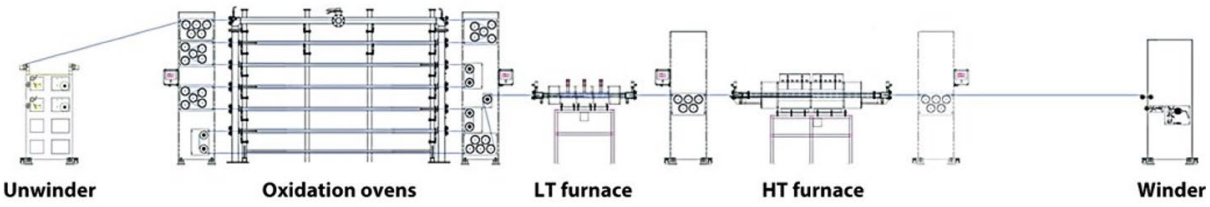

Figure 5.1 Schematic of the continuous stabilization and carbonization line at Georgia Tech

The setup involves six oxidation and stabilization ovens, followed by the low temperature (LT) and high temperature (HT) carbonization furnaces. In each oven or zone, there are three key processing variables: temperature, strain (%), and the residence time (RT). Stabilization takes place in air while the LT and HT carbonization furnace has a nitrogen atmosphere. The gas flow rates can be varied in each furnace. Being a continuous process, the residence times in different zones are not independent of each other and are largely dictated by the unwinding speed. The applied strain can be varied for each stage by changing the motor speed between different zones. The temperature in each furnace can be controlled independently.

5.2.2 Data Acquisition

In this study, the data set consists of 600 distinct carbonization trials that were conducted at Georgia Tech. For each trial, the data consist of the following PAN precursor processing parameters: PAN molecular weight, CNT content, spinning geometry, solution concentration, the number of coagulation baths used during fiber spinning, and the total draw ratio (i.e. the stretch ratio applied during spinning and fiber drawing). The stabilization and carbonization data include the RT, temperature, and applied strain for

each zone. The output properties that were measured for the resultant carbon fibers were the tensile strength and the tensile modulus.

Each carbon fiber tow consisted of 100 filaments, and at least 50 filaments from each trial were individually tested using a FAVIMAT+ single fiber tester, and the average values of tensile strength and modulus were recorded. The data on carbonization processing parameters and resultant carbon fiber tensile properties have been reported by Chae et al. [6]. Tensile strength and modulus as high as 5.75 GPa and 375 GPa, respectively, were achieved during these trials. Over the 600 trials, tensile strength varies in the range of 2.0-5.75 GPa, and the tensile modulus varies from 240-375 GPa. A snapshot of the experimental data is provided in Table 5.2. It is important to note that there are over 70 processing variables that may have an impact on the resultant carbon fiber tensile properties. However, for the purpose of this exploratory study, we have limited the number of input processing parameters to the 31 listed in Table 5.1. The goal of this study is to explore whether ML techniques could be used to establish an underlying mathematical function that could relate the processing-property relationship for carbon fiber manufacturing.

Table 5.1 Experimental data set - processing parameters

Precursor Manufacturing	**Stabilization (6 zones)**	**Carbonization (LT, HT)**
Pan Mol. Wt. CNT content Solution concentration Spinning geometry Coagulation bath configuration Draw ratio	Residence time (6) Temperature (6) Strain (6) Total stabilization time	Residence time (2) Temperature (2) Strain (2)
6 parameters	19 parameters	6 parameters
Total processing parameters = 31 **Output:** Tensile strength, Tensile modulus		

Table 5.2 Snapshot of the carbon fiber manufacturing data, and range of values of the features used for the study. Feature values were varied within the stated range over 600 experimental trials for which the tensile strength and modulus were values were measured

Feature	Range
PAN molecular weight	400 kg/mol – 550 kg/mol
CNT content	0 wt% – 2 wt%
Spinning geometry	Single component or core sheath (bicomponent)
Coagulation bath	1 or 2 baths
Draw ratio	15 - 28
Cumulative oxidation strain	4% - 18%
Oxidation residence time in each zone (Z1-Z6)	30 – 60 min
Oxidation temperatures in zone Z1-Z6	150 – 350 °C
LT carbonization temperature in zone 1 – zone 3	500 – 1000 °C
LT carbonization strain	4% - 20%
LT carbonization residence time	10 min – 25 min
HT carbonization temperature	1300 – 1600 °C
HT carbonization strain	0% to -6%
HT carbonization residence time	10 min – 25 min
Tensile Strength (output)	2.0 – 5.75 GPa
Tensile modulus (output)	240 – 375 GPa

5.3 Machine Learning Models

5.3.1 Feature Engineering

5.3.1.1 Feature Pre-processing

- Oxidation strain

  In the experimental data, there is a feature associated with the oxidation strain in each of the zones. This was replaced with the cumulative oxidation strain across all six zones using Equation 2.

$$cumulative\ oxidation\ strain = \prod individual\ oxidation\ strain \qquad (2)$$

- Low Temperature Furnace

  The low temperature furnace (Temp LT) consists of three temperature zones. It was observed that there was a pattern in the values of Temp LT; there were only a few distinct values of the temperature values. Therefore, the features are transformed into a categorical variable with three values (1, 2 or 3) representing three temperature patterns. When feeding these values to the model, based on the numeric values assigned to each of the patterns, the model could assume that a particular pattern is thrice as important as another one. To avoid this, one-hot encoding was employed. In one-hot encoding, the numeric value assigned earlier is removed, and it is replaced with a new binary feature column for each numeric value. Thus, in this case, three new feature columns corresponding to each distinct pattern of Temp LT were created.

- High Temperature Furnace

  The high temperature furnace (Temp HT) either had one or two temperatures throughout the furnace. For consistency, we replaced these values with the mean temperature value.

5.3.1.2 Dimensionality Reduction

As the number of features in the dataset is increased, it leads to an exponential increase in the volume associated with the data in Euclidean space. The original data become sparse in this new, higher-dimensional space. For example, consider the case when the data lie completely within a unit square. When another feature is added, the dimension increases by 1. The data are now represented in a unit cube. These data that seemed adequate in the original space now seem sparse in the new dimensions. For the current model to achieve a similar performance with ML models, significant amount of data must be added (which is not always possible). This phenomenon is referred to as the curse of dimensionality [115]. In problems such as this study, where adding many more data points may not be feasible, the dimensionality of the data must be reduced by reducing the number of features. This process relies on both domain knowledge and mathematical analysis of the features. There are two main methods of dimensionality reduction - feature selection and feature transformation, detailed in the following sections.

5.3.1.3 Feature Selection

At the end of feature pre-processing, the dataset had approximately 600 data points with 26 features. The number of features were reduced from 31 to 26 by replacing the oxidation strains in each zone by the cumulative oxidation strain as described in section

3.1.1. To reduce the number of features further, the features to be kept were selected based on the Pearson correlation coefficient (PCC) [116] of each of the features. PCC is defined as the normalized covariance between two variables (Equation 3).

$$\rho(X,Y) = \frac{cov\ (X,Y))}{\sigma_X \sigma_Y} \tag{3}$$

The value of PCC ranges between -1 and +1. Values close to +1 and -1 indicate a strong linear correlation between the two variables; whereas, values around 0 indicate low correlation. PCC of each of the features was calculated with the target value. The features were then ordered according to the absolute values of their PCC and those above a certain threshold were selected. The PCC values of all 26 features for tensile strength and tensile modulus are shown in Figure 5.2(a) and 5.2(b), respectively. The top five features with the highest PCC for tensile strength and tensile modulus, are listed in Table 5.3. Based on the PCCs, it seems that furnace temperature in LT carbonization furnace, and certain zones in the stabilization process, as well as the strain applied during LT carbonization have the highest correlation with tensile strength and modulus. One limitation of this approach is that it assumes a linear relationship between the feature and the target value, which may not be the case. However, this approach of dimensionality reduction was found to work well with certain models.

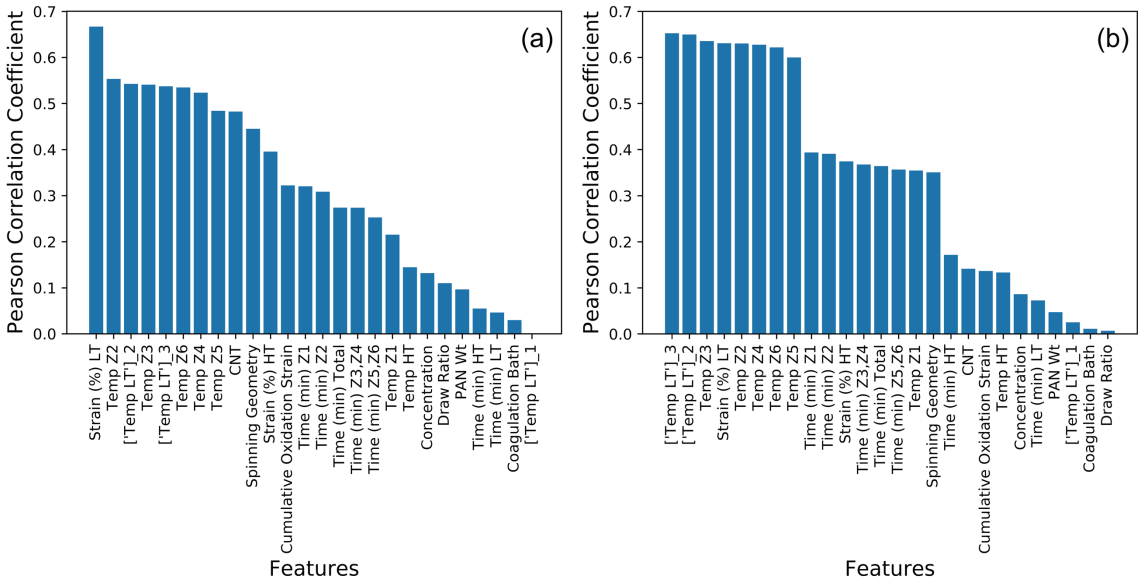

Figure 5.2 PCC values of features for (a) tensile strength, and (b) tensile modulus

Table 5.3 Top five features with the highest Pearson correlation coefficients for tensile strength and tensile modulus

Tensile Strength	**Tensile Modulus**
LT carbonization strain	LT furnace zone 3 temperature
Stabilization zone 2 temperature	LT furnace zone 2 temperature
LT furnace zone 2 temperature	Stabilization zone 3 temperature
Stabilization zone 3 temperature	LT carbonization strain
LT furnace zone 3 temperature	Stabilization zone 2 temperature

5.3.1.4 Feature Transformation

Feature transformation is a method that reduces dimensionality by transforming existing features, to set of new, lower-dimensional features. For this study, Principal

Component Analysis (PCA) [117] was used. PCA uses Singular Value Decomposition (SVD) to transform the features into orthogonal space (based on their eigen-vectors) represented by principal components. Based the variance explained by each of the components, a threshold can be set and the number of components to retain can be chosen.

5.3.2 Details of Machine Learning Models Employed

In the following sections, a brief overview of the theoretical aspects of each ML model is provided, followed by details of its implementation in this work.

5.3.2.1 Support Vector Regression (SVR)

1. SVR Overview

SVMs were first introduced by Vapnik in [118] as models to solve binary classification problems. Since then, they have been expanded to handle both classification and regression problems. SVMs classify datasets by maximizing the margin between the target hyperplane and the training data points, while classifying as many training examples correctly as possible. SVRs [119, 120] expand on this by introducing an ϵ-tube. An ϵ-tube is the numerical range within which the value predicted by the model is allowed to deviate from the actual value. While training, the model is not penalized for any values that fall within ϵ of the actual value (ϵ-intensive). To represent the non-linearity of the data, the data are mapped into higher-dimensional space using kernel functions (represented by gram function G). SVR finds coefficients (α_i, α_i^*) that minimize Equation 4:

$$L(\alpha) = \sum_{i=1}^{N}\sum_{j=1}^{N}(\alpha_i - \alpha_i^*)(\alpha_j - \alpha_j^*)G(x_i, x_j) + \epsilon\sum_{i=1}^{N}(\alpha_i + \alpha_i^*) - \sum_{i=1}^{N}(\alpha_i - \alpha_i^*) \quad (4)$$

with the constraints:

$$\sum_{i=1}^{N}(\alpha_i - \alpha_i^*) = 0$$

$$\forall i, 0 \leq \alpha_i \ , \alpha_i^* \ \leq C$$

where C a positive numeric constraint that controls the penalty assigned to a prediction outside the ϵ margin. In other words, by minimizing this equation, the error in prediction is being reduced. Once these optimal coefficients are found, the values for new points are calculated using Equation 5:

$$f(x) = \sum_{i=1}^{N}(\alpha_i - \alpha_i^*)\, G(x_i, x) + b \quad (5)$$

2. Implementation

For this study, the SVR function from the python package scikit-learn [121] was utilized. Rectified Linear Unit (ReLU) activation function was used. For the SVR model, various hyper-parameters such as the kernel function and the values of C, ϵ were varied

via exhaustive grid searches. The final tuned values of all relevant hyperparameters are reported in section 4.1.1.

5.3.2.2 Gradient Boosted Regression Trees (GBRT)

1. GBRT overview

Regression trees are based on recursive partitioning of the dataset according to its features. They contain a prediction score on every leaf. To improve scalability and robustness, multiple trees (ensemble) are used instead of a single one. The final prediction will be the sum of the scores of all the leaves of each of the trees. While training an ensemble of trees, a method such as stochastic gradient descent cannot be applied since a continuous function is not being approximated. Instead, boosting is used for training and optimization. Initially, a constant value is predicted for the examples. At each iteration, the prediction of one tree is added and the ensemble is iteratively improved. At step *t* of training,

$$\hat{y}_i^{\,t} = \sum_{k=1}^{t} f_k(x_i) = y_i^{t-1} + f_t(x_i) \tag{6}$$

where:

$\hat{y}_i^{\,0} = 0$

$\hat{y}_i^{\,t}$: refers to the prediction of the i^{th} example during the t^{th} step of training

$\mathrm{f_t}$ is chosen as the tree that minimizes the objective function described in Equation 7:

$$obj^t = \sum_{i=1}^{n} L\left(y_i, \hat{y}_i^{t-1} + f_t(x_i)\right) + \Omega(f_t) \quad (7)$$

where:

L: is the loss function of the model

Ω: is the regularization function that penalizes complexity in the model

Once training is complete, the predictions of all the trees in the ensemble are used to obtain the final prediction.

2. Implementation

To implement GBRTs, we have used XGBoost [122]. XGBoost is a widely recognized open-source implementation of GBRTs. It has shown to achieve state of the art results for problems ranging from predicting store sales to motion detection. Part of its success is its scalability in distributed and memory-limited environments. Hyperparameters such as learning rate, maximum depth of the trees, number of trees, regularization term, and ratio of columns to use for each tree were varied via exhaustive grid searches. The final tuned values of all relevant hyperparameters are reported in section 5.4.1.1.

5.3.2.3 Multi Layer Perceptron (MLP)

1. MLP Overview

MLPs are a type of feedforward artificial neural networks (ANN) [123]. They are widely used in computer science, engineering, and other applications to predict/estimate

non-linear functions. An MLP consists of three types of layers - one input layer, any number of hidden layers and a single output layer. Since a regression problem is being predicted, the output will be a single, continuous value.

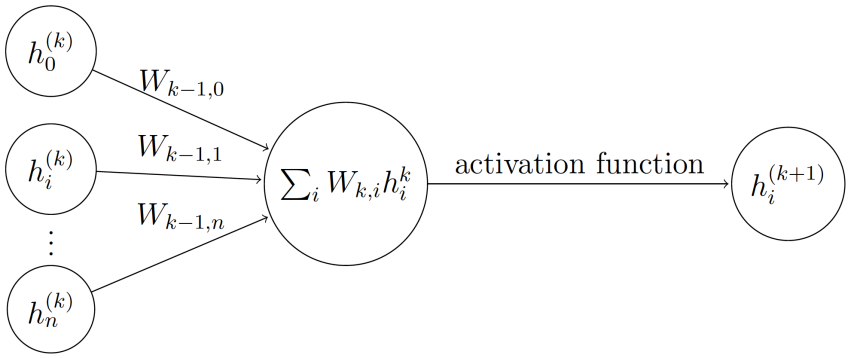

Figure 5.3 Structure of a single perceptron belonging to the (k+1)th layer of the MLP

Figure 5.3 represents the structure of a single perceptron belonging to the $(\mathrm{k}+1)^{\mathrm{th}}$ layer of the MLP. The value of the perceptron is obtained by applying a function (called the activation function) to the weighted sum of the nodes in the previous layer $\left(\mathrm{k}^{\mathrm{th}}\mathrm{layer}\right)$ represented by the Equation 8.

$$h_i^{k+1} = f_{activation}\left(\sum_i W_{k,i}\, h_i^k\right) \tag{8}$$

The final output of the model is calculated by applying this equation to the final hidden layer. The activation function is useful in adding non-linearity to the model. Some commonly used activation functions are sigmoid, ReLU, and tanh. ReLU has been used as the activation function in the current study.

The accuracy of the MLP is measured using a loss function that measures the difference between the predicted and the actual value. Typically, mean squared error is used for regression problems.

$$MSE = \frac{1}{N}\sum_{i=1}^{N}(f_i - y_i)^2 \tag{9}$$

where:

N: number of training examples

f_i: output of the MLP at example *i*

y_i: actual value of example *i*

The objective of training an MLP is to obtain the weights, W, that minimize this loss function and improve prediction accuracy. This is done by applying backpropagation to the MLP. Backpropagation [124] evaluates the derivative of the loss function as a product of the derivatives of each of the layers. It calculates the error of each layer in a backwards manner as described in Equation 10.

$$\delta^{k-1} = (f^{k-1})'(W_k)^T\delta^k \tag{10}$$

The weights are then updated using these values. When the model finishes training, the weights are fixed, and these fixed weights are used to evaluate new examples.

2. Implementation

The MLP was implemented using Keras [125], a deep learning library for Python. For this study, due to the size of the dataset, an MLP with two hidden layers has been used. Different numbers of hidden units in each of the layers, optimizers, activation functions, and batch sizes were varied during training by doing exhaustive grid searches. The final tuned values of all relevant hyperparameters are reported in section 5.4.1.1.

5.3.2.4 Recurrent Neural Network (RNN)

1. RNN overview

Recurrent neural networks (RNNs) are neural networks that can accommodate temporal dependencies in data that are inherently transient or sequential, such as the carbon fiber manufacturing process where the stabilization process is followed by carbonization. RNNs achieve this by using feedback connections to `remember' information in previous time steps. In a typical RNN, the activation can be expressed as:

$$h^m(t) = w_1\phi[h^{m-1}(t)] + w_2\phi[h^m(t-1)] \quad (11)$$

In equation 10, $h^m(t)$ denotes the activation vector in layer m at timestep t, $h^{m-1}(t)$, denotes the activation in the layer below (i.e. layer m - 1) at the current timestep t and $h^m(t - 1)$, likewise corresponds to the previous timestep at layer m. $\emptyset$ is a non-linear function applied elementwise, and w_1 and w_2 are trainable weights. A key limitation of the basic RNN described above is that it cannot relay temporal information over an extended number of time steps, due to the vanishing gradient problem (as mathematically shown by Hochreiter and Schmidhuber [126]). Solutions such as long short-term memory (LSTM)

units and Gated Recurrent Units (GRUs) have been proposed to store and propagate information over a longer time interval. In this work, the GRU was used to model the activation $h^m(t)$, as it has fewer parameters compared to an LSTM. Details of the GRU and how it allows for modeling longer-term temporal dependencies are provided in other literature [127].

2. Proposed RNN model

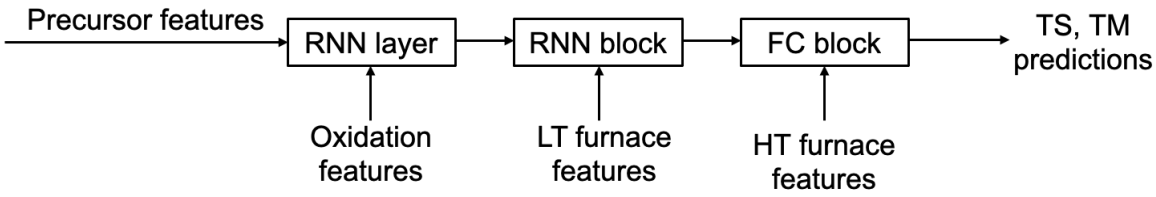

Figure 5.4 Schematic representation of the RNN model to predict tensile strength (TS) and tensile modulus (TM) of carbon fibers

Figure 5.4 shows the schematic of a proposed RNN model. The underlying hypothesis behind the development of this RNN model in particular is that the RNN architecture can be potentially leveraged to mimic the manufacturing operations. The central idea is that each of the three processes (i.e. oxidation oven, LT furnace, and HT furnace) can be represented as layers in an RNN model. The oxidation oven and the LT furnace are represented as RNN layers (as these have multiple zones or “time steps"); whereas layer 3, which corresponds to the HT furnace, is simply a concatenation and input to the fully connected/dense layer. Each RNN layer shown in Figure 5.4 is a GRU activation generating an output of a fixed length, where the length of the output is a hyper-parameter.

Gated Recurrent Units (GRU) with a small number of units (10 units in the RNN layers) have been used, as the dataset is relatively small in the context of a machine learning model. As mentioned previously in this section, GRU units have fewer parameters to fit compared to LSTM units, and using a small number of units ensures that the RNN model is not prone to overfitting. ReLU activation has been employed within the GRU units, as ReLU (and ReLU variants) have, in general, showed improved performance compared to other activation functions. ADAM has been used as the optimization algorithm, which is a state-of-the-art optimizer that has been shown to perform well compared to other algorithms.

The implicit assumption here is that the set of operations in a given process can be represented as a sequence, such that weight parameters can be shared across multiple operations within a given process. In other words, RNN attempts to imitate the sequential nature of the carbon fiber manufacturing process where stabilization is followed by LT and HT carbonization. As such, due to the nature of the RNN model, feature selection or dimensionality reduction cannot be applied, and the RNN model is applied on the original set of features.

5.4 Results and Discussion

5.4.1 Results

For each of the models, we tuned the hyper-parameters to obtain the optimal values. The optimal parameters for predicting tensile strength and tensile modulus are described in Table 5.4 and Table 5.5, respectively.

5.4.1.1 Optimal Hyper-parameters

Table 5.4 Optimal hyper-parameters per model based on predictions of tensile strength

Model	Hyper-parameters
SVR	RBF kernel, C = 2, epsilon = 0.1
GBRT	Colsample = 1, learning rate = 0.97, max depth = 5, alpha = 3, num of estimators = 15
MLP	Architecture = 26-32-8-1, epochs = 1000, loss = mean squared error, val split = 0.1, optimizer = Adam
RNN	Architecture: described in Figure 5.4 epochs = 100 Number of GRU units in RNN layer 1 = 10 Number of GRU units in RNN layer 2 = 10 Number of units in dense/fully connected layer = 10 optimizer = Adam Activation function in the RNN layer = ReLU Activation function in the fully connected layer = ReLU

Table 5.5 Optimal hyper-parameters per model based on predictions of tensile modulus

Model	Hyper-parameters
SVR	RBF kernel, C = 2, epsilon = 0.03
GBRT	Colsample = 0.8, learning rate = 0.99, max depth = 7, alpha = 0.5, num of estimators = 13
MLP	Architecture = 26-32-8-1, epochs = 1000, loss = mean squared error, val split = 0.1 optimizer = Adam
RNN	Architecture: described in Figure 5.4 epochs = 100 Number of GRU units in RNN layer 1 = 10 Number of GRU units in RNN layer 2 = 10 Number of units in dense/fully connected layer = 10 optimizer = Adam Activation function in the RNN layer = ReLU Activation function in the fully connected layer = ReLU

5.4.1.2 Variation of R^2 Score - Feature Selection and Feature Transformation

Using the hyper-parameters given in Table 5.4 and Table 5.5 for each model, we investigated the effect of number of features on the model using feature selection or feature transformation. For tensile strength, the variation in the validation R^2 score when using feature selection and feature transformation is given in Figure 5.5(a) and 5(b), respectively. For tensile modulus, the variation in the validation R^2 score when using feature selection and feature transformation is given in Figure 5.6(a) and 6(b), respectively. These results

were used to guide the decision on whether to use feature selection or feature transformation to reduce dimensionality of the data while using the three ML models.

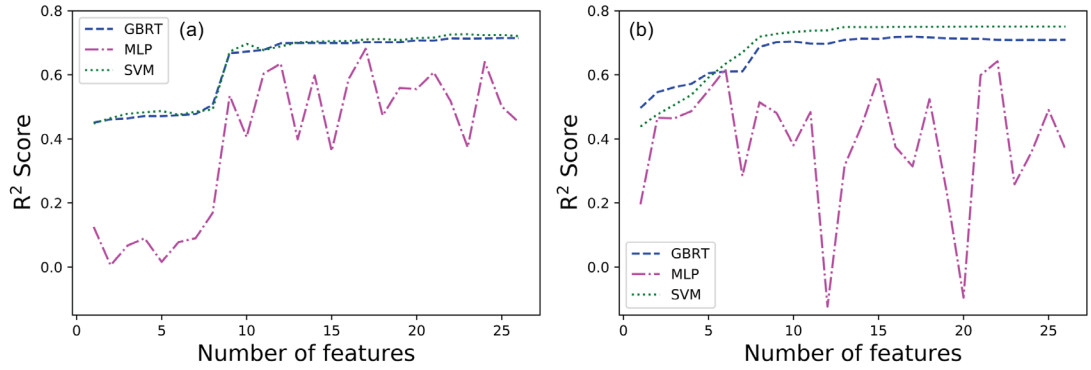

Figure 5.5 Effect of number of features based on (a) feature selection, and (b) feature transformation, on ML model performance for predicting tensile strength

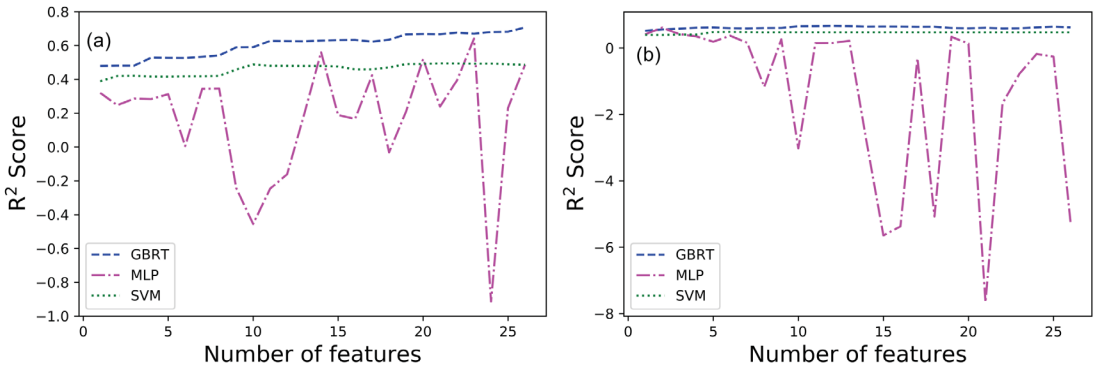

Figure 5.6 Effect of number of features based on (a) feature selection, and (b) feature transformation, on ML model performance for predicting tensile modulus

5.4.1.3 Final R^2 Scores

We use the feature selection and transformation graphs to determine the optimal number of features and method of dimensionality reduction to use and to obtain the R^2 scores over our dataset, as shown in Table 5.6 and Table 5.7. The 600 data points were split using a train-test data split of 90-10, and a five-fold cross-validation was performed using 10% of the training dataset. The results were averaged over five runs. The train-validation-test split was consistent across all models.

The R^2 scores depict the relationship between the actual tensile strength and tensile modulus values and the predicted values. This relationship is highlighted by Figure 5.7 and Figure 5.8. The regression plots shown in these figures are for the test data, and the R^2 scores have been averaged over 5 runs. In a perfect model, all of the points would lie on the x=y line and correspond to an R^2 value of 1. While optimizing the model, we try to minimize the maximum distance between a point and the x=y line.

Table 5.6 R^2 Scores (Averaged over 5 runs) - Tensile Strength

Model	**Train R^2 score**	**Validation R^2 score**	**Test R^2 score**
SVR	0.819	0.748	0.581
GBRT	0.769	0.692	0.586
MLP	0.945	0.804	0.532
RNN	0.858	0.782	0.843

Table 5.7 R^2 Scores (Averaged over 5 runs) - Tensile Modulus

Model	Train R^2 score	Validation R^2 score	Test R^2 score
SVR	0.512	0.490	0.352
GBRT	0.833	0.707	0.370
MLP	0.633	0.367	0.288
RNN	0.699	0.665	0.670

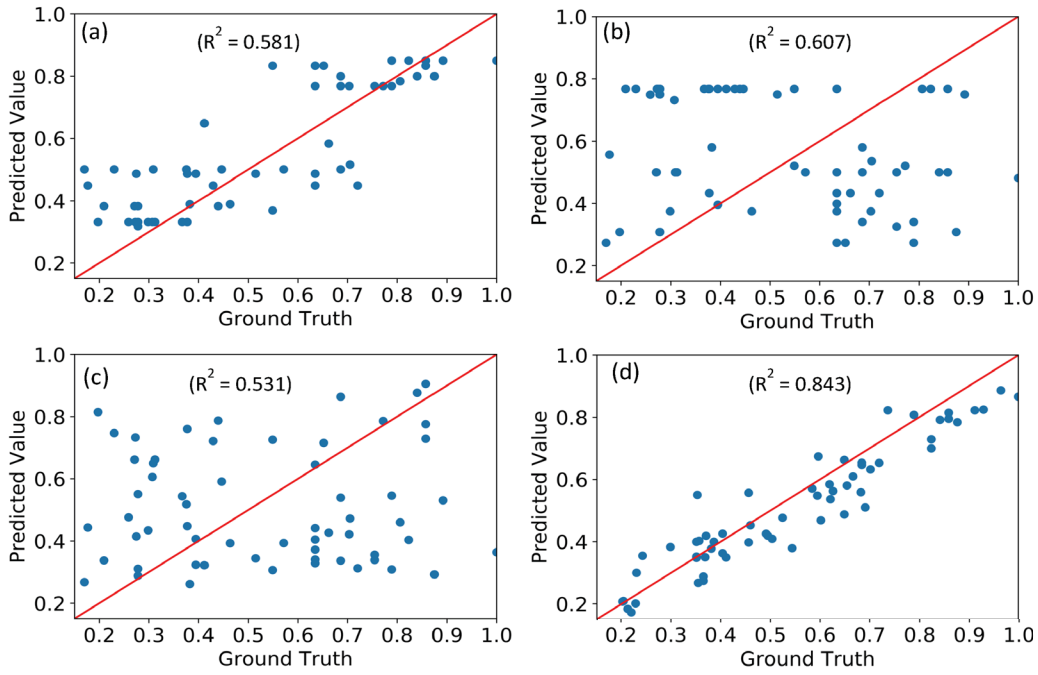

Figure 5.7 Regression plots showing the performance of (a) SVR, (b) GBRT, (c) MLP, and (d) RNN in predicting the tensile strength of the test data. The data were split using a train-test data split of 90-10, and a five-fold cross-validation was performed using 10% of the training dataset. The results were averaged over five runs. The train-validation-test split was consistent across all models.

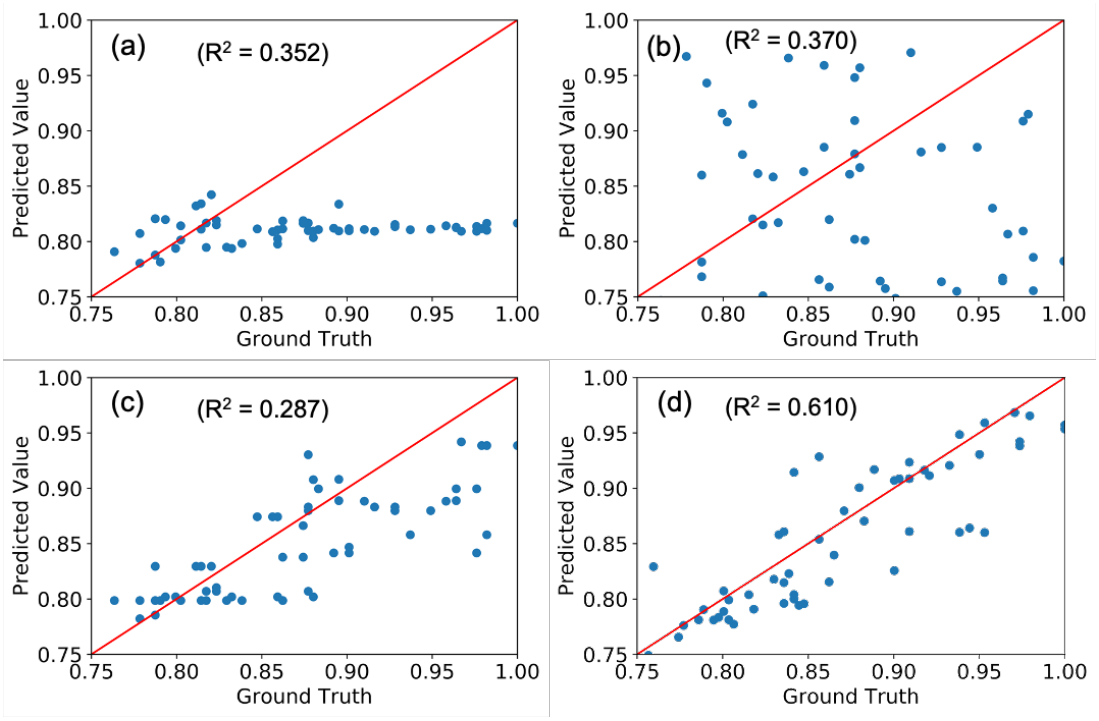

Figure 5.8 Regression plots showing the performance of (a) SVR, (b) GBRT, (c) MLP, and (d) RNN in predicting the tensile modulus of the test data. The data were split using a train-test data split of 90-10, and a five-fold cross-validation was performed using 10% of the training dataset. The results were averaged over five runs. The train-validation-test split was consistent across all models.

5.4.2 Discussion

5.4.2.1 Pearson Correlation Coefficients

The absolute values of PCCs of the 26 features for the tensile strength and tensile modulus are shown in Figure 5.2. The five features with the highest correlation are listed in Table 5.3. For tensile strength, the PCCs of 0.5 or above belong to the LT carbonization strain, temperature, and stabilization zone temperatures. For tensile modulus, the PCCs of 0.5 or above belong to the stabilization and LT carbonization features as well. It is interesting, that the same five features have the highest PCCs for both tensile strength and

tensile modulus. This could be explained by the structural transitions that occur during the processes that these features belong to. The stabilization process involves conversion of PAN into stabilized PAN, through a combination of cyclization, oxidation, and cross-linking reactions. The next major structural and chemical change occurs when the stabilized PAN fiber enters the LT carbonization furnace, where the stabilized PAN fiber is converted into carbon fiber. However, we acknowledge that the PCC approach assumes a linear relationship between the features and the tensile properties, which may not be the case. As correlation does not imply causation, these results solely should not be used to definitively narrow down the focus of experimental investigations to only the specific features with the highest correlation. Rather, the PCCs should be used to investigate the overall processing stage to which these top features belong to, which in this case are stabilization and LT carbonization.

5.4.2.2 Feature Selection vs. Feature Transformation for Reducing Dimensionality

We see in Figure 5.5 and Figure 5.6 that the effect of feature selection and transformation are different based on the model. We see that GBRT performs better with feature selection; whereas, the other models perform better using feature transformation. We can attribute this to the difference in the model structures. SVRs and MLPs try to find the best coefficients that represent the data in a mathematical function - thus, the orthogonal transformation of the features is helpful. On the other hand, GBRTs work by splitting the data on certain features. By transforming the features, we lose the insight given by the feature values. Therefore, feature selection is more useful than feature transformation when we are using GBRTs.

5.4.2.3 MLP Performance

As compared to the other models, we observe that the performance of the MLP is inconsistent, attributed to the fact that even as we keep the hyper-parameters constant, each time we train the model the initial weights of the model have different results. Thus, the results will not remain consistent with every run. We can reduce this uncertainty by considering an ensemble of MLPs. The severe ups and downs seen in Figures 5.5 and 5.6 could be because the structure of the network is not conducive to estimate a function for certain numbers of features. Overall, the fluctuating nature of the graphs for MLPs indicates that they may not be a reliable model to solve this problem.

5.4.2.4 GBRT and SVR Performance

GBRT seems to perform relatively better than MLP on the data. This can be attributed to the size and structure of the data. Since the amount of data is small, it becomes harder to approximate a mathematical function to model the data (due to high dimensionality). On the other hand, GBRTs function well with smaller data sets as they allow to limit the depth of the tree. While collecting the data, it is possible that certain features were modified more than others, or were only varied within a certain range. GBRTs have more flexibility to accommodate such factors within their branching conditions as compared to the other models tested.

5.4.2.5 Success of RNN

Table 5.6 and Table 5.7 show that the RNN model, in general, performs comparatively better than the other ML models, consistently across data splits. In predicting tensile

strength (Table 5.6), the RNN model achieves an R^2 of 0.843 on the test data, corresponding to a relative error 14.6% with respect to the mean squared average of tensile strength in test data. In predicting tensile modulus (Table 5.7), the RNN model achieves an R^2 of 0.670 with a relative error of 4.4%. While we cannot infer decisively why the RNN performs better than the other ML models, two possible reasons are described below:

- As mentioned in Section 3.2.4, the proposed RNN attempts to closely model the manufacturing process workflow, which means that the RNN might be a better representation of the actual manufacturing process.
- Since the RNN models account for the entire process as a sequence, the weights associated with each GRU unit are shared across timesteps. This means that the RNN model has considerably fewer parameters or weights, compared to, for instance, an MLP model which treats each operation in a process as a distinct feature. Therefore, the RNN model is less prone to overfitting.

5.5 Conclusions

In this study, we investigated the efficacy of four ML techniques, viz. SVR, MLP, GBRT, and RNN, in predicting the carbon fiber tensile properties based on input processing parameters. The data consisted of 600 distinct points with 31 features. We investigated feature selection and feature transformation as the dimensionality reduction techniques and their efficacy on the performance of SVR, MLP, and GBRT models. Based on the predictions of tensile strength and tensile modulus from these ML techniques, we draw the following conclusions:

- The features with the highest Pearson correlation coefficients for tensile strength and tensile modulus are associated with the LT carbonization temperature and strain, as well as the stabilization temperatures in certain zones. It is worth exploring the effect of the features associated with the stabilization and LT carbonization process, on the tensile strength and modulus of carbon fibers while performing future experiments.
- Based on the results generated herein, RNNs seem to outperform, consistently across data splits, the other models, for the available dataset. The success of RNNs can be attributed to two factors - the RNN better represents the actual manufacturing process flow, and the model is less prone to overfitting as compared to other models in this case.
- Results from this study demonstrate that machine learning models can serve as surrogates to map processing parameters to carbon fiber properties.

CHAPTER 6. CONCLUSIONS AND RECOMMENDATIONS FOR FUTURE WORK

6.1 Conclusions

This work details the development of three technological pathways to accelerate paradigm shifts in the way carbon fibers are developed and manufactured. The first two, hollow carbon fibers and small diameter carbon fibers, provide a comprehensive understanding of the process, structure and property relationship of these continuous carbon fibers. The third pathway provides insights into the challenges and opportunities to employ machine learning models to predict the carbon fiber properties by leveraging experimental data and accelerate the improvement in tensile properties in a cost-efficient manner.

CHAPTER 2 detailed the development of continuous hollow carbon fibers. An 80% improvement in tensile strength was achieved for these fibers compared to the previously reported batch processed hollow carbon fibers. The specific tensile properties of these fibers are superior to the T300 fibers, and the specific tensile modulus is 20% higher compared to the IM7 fibers. The tensile strength is limited by defects with size ranging from 40-70 nm. These defects could be caused due to the degradation of PMMA during the low temperature carbonization stage; however, this is yet to be verified.

The surface treated and sized hollow carbon fibers from CHAPTER 2 were used to manufacture six-ply unidirectional composites in an epoxy matrix. The mechanical properties of these composites were tested and compared with IM7 composites. The lower

tensile strength in the hollow carbon fiber composites compared to IM7 composites is attributed to the lower strength of hollow carbon fibers, poor adhesion between the epoxy and matrix, as well as lower fiber alignment in the epoxy matrix. The poor fiber-matrix adhesion indicates need to optimize the surface treatment and sizing of the hollow carbon fibers. The compressive strength of the hollow carbon fibers is 81% of the tensile strength at room temperature. This is significantly higher compared to the compressive strength of IM7 composites, which is reported to be 60% of the tensile strength. The moisture pickup in hollow carbon fiber composites compared to IM7 composites suggests that the hollow channels are likely not picking up any significant moisture. Overall, the properties of hollow carbon fibers and their composites show great promise to replace conventional aerospace grade carbon fibers in the foreseeable future.

In CHAPTER 4, the development of continuous carbon fibers with 2-3μm diameter has been described. These small diameter carbon fibers have tensile strengths as high as 5.1 GPa and tensile moduli as high as 434 GPa in different trials. The tensile strength was improved by 57% compared to the previously reported 3.2 GPa for batch processed small diameter fibers. The size of the defects in these fibers is estimated to be in the range of 35-70 nm. Compared to the hollow carbon fibers and IM7 fibers, no surface defects were observed in the TEM images, which could be attribute to the smaller diameter of the fiber suppressing the formation of these defects. The tensile strength could be limited due to non-uniformity of the fiber cross section, which may lead to larger defects that were not observed in the surface regions that were imaged using TEM. The non-uniformity in the PAN island cross-section is introduced during precursor manufacturing and this process needs to be further modified to obtain a uniform fiber cross section. The high tensile

modulus can be attributed to the higher level of graphitic ordering observed in these fibers compared to the IM7 and control carbon fibers. The higher graphitic ordering is likely due to the smaller diameter of the PAN island fibers which resulted in a diminishing skin-core effect due to better oxygen diffusion and heat transfer during stabilization.

In CHAPTER 5, the efficacy of four ML techniques, SVR, MLP, GBRT, and RNN, in predicting the carbon fiber tensile properties based on input processing parameters was investigated. The data set consisted of 600 data points with 31 features each. The features with the highest Pearson correlation coefficients for tensile strength and tensile modulus are associated with the LT carbonization temperature and strain, as well as the stabilization temperatures in certain zones. RNNs seem to outperform, consistently across data splits, the other models, for the available dataset. The success of RNNs can be attributed to two factors: the RNN better represents the actual manufacturing process flow, and the model is less prone to overfitting as compared to other models in this case. This study demonstrates that the carbon fiber processing parameters can be mapped to fiber tensile properties using ML models.

6.2 Recommendations for future work

As a next step in bringing hollow carbon fibers closer to replacing conventional carbon fibers, the tensile strength of the hollow carbon fibers needs to be improved. Further modification and optimization of the carbon fiber manufacturing process – the effect of PMMA degradation on the formation of defects in hollow carbon fibers needs to be studied. This could be done by adding an additional furnace between the stabilization and low temperature carbonization furnace, which would allow control over PMMA degradation.

Currently the stabilization process takes place in air while carbonization takes place in an inert atmosphere. To better understand and control PMMA degradation the effect of temperature and atmosphere needs to be studied. The furnace used for this purpose should therefore have the ability to control both temperature and atmosphere. Reducing the effective diameter of the hollow carbon fiber to 5-6 μm, comparable to IM7 fiber diameter, will likely improve the tensile strength of the fiber even further and potentially even surpass the IM7 tensile strength. The effect of these processing changes in terms of the size of defects in the fiber needs to be further analyzed. A combination of TEM, TEM tomography, and synchrotron X-Ray CT needs to be employed to develop a comprehensive understanding of the size and shape of the defects with high confidence and over large length scales. In the current study, only one fiber from a single trial was characterized. A future study could focus on 3D characterization of the defects in the hollow carbon fibers and establishing a relationship between the processing parameters, observed defect size and the tensile properties of the hollow carbon fibers.

Further characterization of mechanical properties of hollow carbon fiber composites is recommended. Due to the limited quantity of hollow carbon fibers produced to date, a limited number of composite panels have so far been manufactured. Manufacturing additional composite panels will allow further mechanical tests such as flexural strength, transverse property tests. Additionally, bidirectional or multidirectional laminates should be tested and the properties could be compared to IM7 composites. This would require production of hollow carbon fibers at a scale higher than what was achieved in the current study (740 filament tow). The eventual goal for advancing this technology should be to produce hollow carbon fibers in large enough quantity to test scale models of aircraft

components in a wind tunnel facility to assess the performance of these fibers in relevant environments, thereby advancing the technology readiness level to TRL 5 and beyond.

To advance the small diameter carbon fiber technology, the future work could explore the optimization of the bicomponent precursor manufacturing to achieve a uniform, circular cross-section of the PAN islands. This could involve modifying process parameters including, but not limited to, polymer solids content in the solutions, polymer molecular weight, coagulation bath composition and temperature. Additionally, one could explore alternatives to PMMA as the sacrificial sea component. It might be worth exploring the use of a sacrificial polymer that could be removed during or after the drawing process and prior to stabilization and carbonization. Similar to hollow carbon fibers, further characterization of defects using TEM and other tomography tools is of great interest to improve the tensile strength of these fibers.

The experiments proposed in the work are expected to produce large experimental datasets which could be further incorporated into the ML models. Future work can focus on incorporating ML models as part of an optimization process that can suggest a more "informed" set of processing variables to maximize tensile strength or tensile modulus. Future work can also focus on developing methods to incorporate multimodal data (e.g. image data, X-Ray diffraction, and any other structural data) as part of the ML framework. Developing an ML model that can take into consideration the entire carbon fiber manufacturing process, and reasonably predict the tensile properties of the resultant carbon fibers, is expected to lead to significant time and cost savings, as well as accelerate the development of next-generation carbon fibers.

This thesis develops a comprehensive understanding of the three technologies that can each accelerate the development high performance structural carbon fibers. Pursuing these studies separately or in conjunction with each other will likely bring about a paradigm shift in the way high performance carbon fibers and composites are developed.

APPENDIX A SUPPORTING INFORMATION FOR CHAPTER 2

Figure A.1 Multifilament fiber spinning (left) and multistage drawing facility (right).

Figure A.2 Continuous stabilization and carbonization facility.

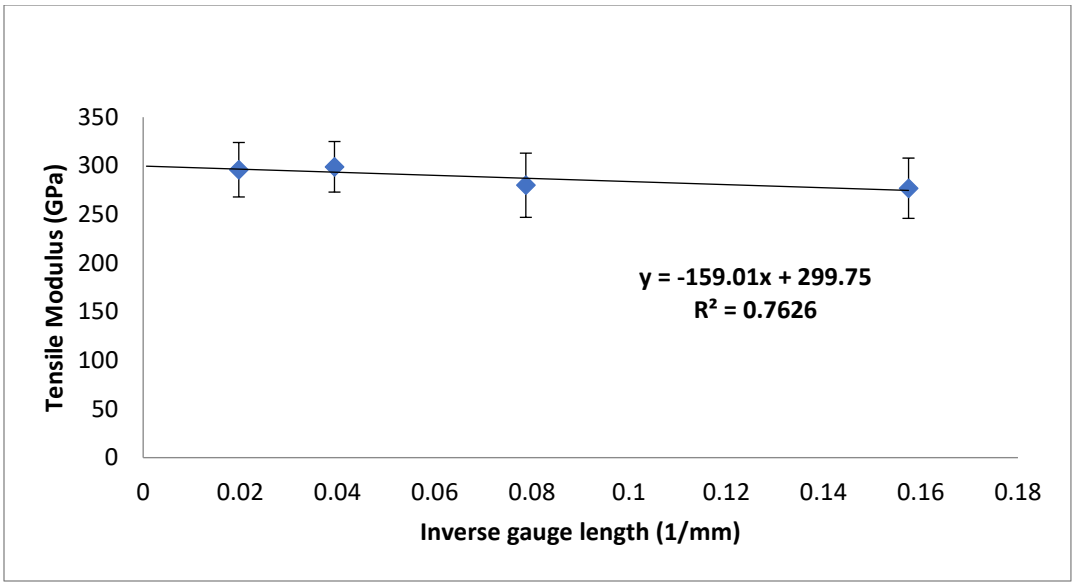

Figure A.3 Plot of tensile modulus vs. inverse gauge length. Extrapolation of the tensile modulus of the hollow carbon fibers from trial T5 for infinite gauge length marks an intercept at 300 GPa. The tensile modulus at a 12.7 mm gauge length was measured to be 280 GPa. This gives a compliance correction factor of 7% which was applied to all the tensile moduli values reported in table 3.

Figure A.4 740 filament tow hollow carbon fiber spools.

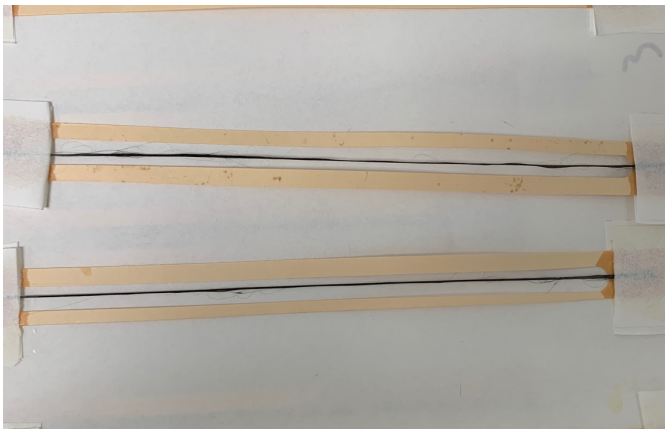

Figure A.5 Hollow carbon fiber epoxy composite strands mounted on paper tabs for tensile testing.

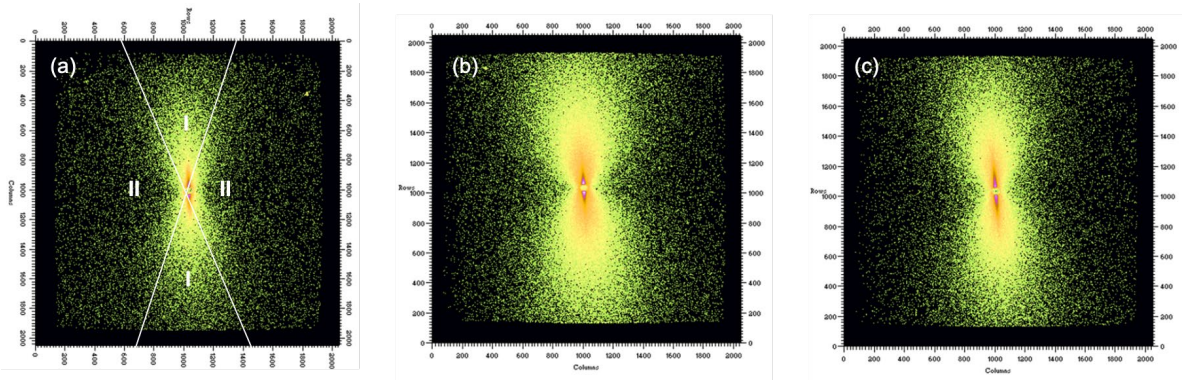

Figure A.6 SAXS 2D scattering pattern from T1-2 (a), T5-1 (b) and GT control carbon fiber (c). The solid white line in (a) represent the sector average.

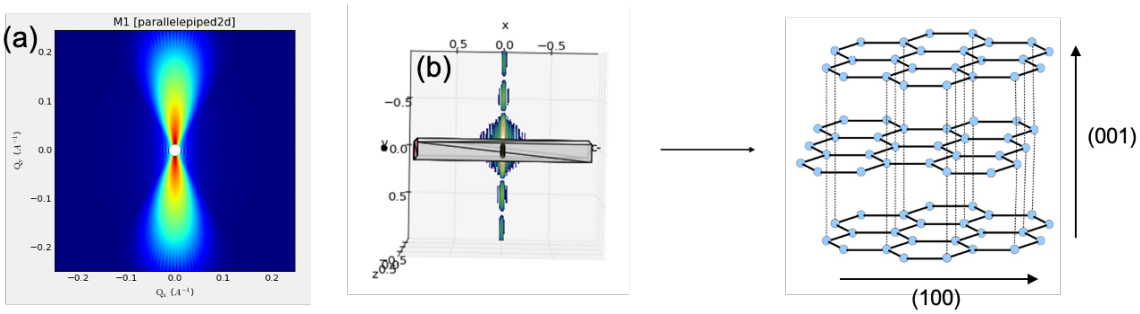

Figure A.7 SAXS Simulated 2D scattering pattern for T5-1 (a), with the length A = B = 2 nm and C = 100 nm. (b) The orientation of the graphite in the fiber.

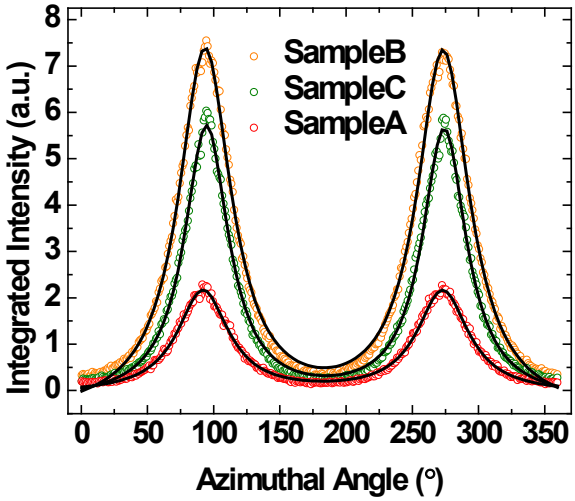

Figure A.8 Experimental (open symbols) and best fitted (solid lines) SAXS azimuthal scattering intensity. Red, orange and green circles represent T1-2, T5-1 and GT control carbon fiber, respectively.

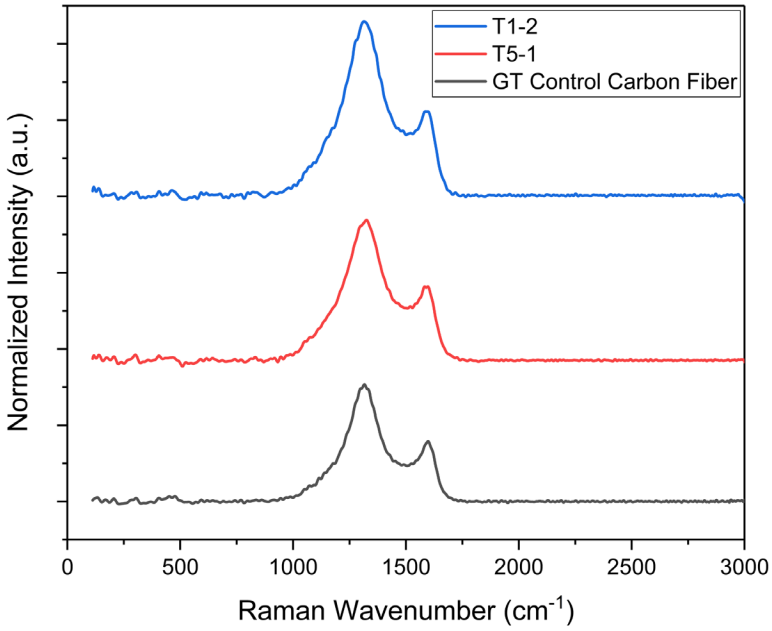

Figure A.9 Raman spectra for hollow carbon fibers (T1-2 and T5-1) and GT control carbon fiber.

Table A.1 Comparison of tensile properties of hollow carbon fibers from trial T5-1 from single filament test and composite strand tests.

Trial T5-1	**Gauge Length (mm)**	**Tensile strength (GPa)**	
		Based on effective diameter	Based on outer diameter
Single filament test (25 test average)	12.7	3.5 ± 0.6	2.3
Composite strand test (ASTM D4018)	152.4	3.5 ± 0.1	2.3

Table A.2 Fitting parameters extracted from the SAXS azimuthal analysis

	Area 1	**FWHM**	**Peak 1**	**Area 2**	**Peak 2**	**BKG**
T1-2	1229 ± 23	47.2 ± 0.42	91.9 ± 0.12	1228 ± 23	273 ± 0.12	-0.08 ± 0.01
T5-1	4637 ± 72	48.6 ± 0.36	93.4 ± 0.11	4614 ± 72	273 ± 0.11	-0.58 ± 0.02
GT Control Carbon Fiber	2433 ± 34	40.6 ± 0.29	94.6 ± 0.09	2406 ± 34	274 ± 0.09	-0.25 ± 0.01

An azimuthal analysis is shown in Figure X. The data can be fitted by a double Lorentzian function as given in the following equation:

$$I(\chi) = \frac{Area1}{w^2 + (\chi - \chi_0)^2} + \frac{Area2}{w^2 + (\chi - \chi_1)^2} + C,$$

where χ, χ_0 and χ_1 are the azimuthal angle and peak positions, respectively. *Area1* and *Area2* are constants related to peak areas, *C* is background, *w* is half of the peak width.

The form factor of a rectangular slab is expressed as the following equation:

$$\mathrm{I}(q_x, q_y) = \Phi_{slab} \times V_{slab} \times \Delta\rho^2 \times \mathrm{P}(q_x, q_y) + bkg$$

$$\mathrm{P}(q_x, q_y) = \left[\frac{\sin(\frac{1}{2}qA\cos\alpha)}{\frac{1}{2}qA\cos\alpha}\right]^2 \times \left[\frac{\sin(\frac{1}{2}qB\cos\beta)}{\frac{1}{2}qB\cos\beta}\right]^2 \times \left[\frac{\sin(\frac{1}{2}qC\cos\gamma)}{\frac{1}{2}qC\cos\gamma}\right]^2$$

$$\cos\alpha = \hat{A}\cdot\hat{q}, \cos\beta = \hat{B}\cdot\hat{q}\ and\ \cos\gamma = \hat{C}\cdot\hat{q}$$

The orientation of the particle is described using angles θ, φ and Ψ where θ and φ define the orientation of the director in the laboratory reference frame of the beam direction (*z* axis) and detector plane (*x*-*y* plane), while the angle Ψ is effectively the rotational angle around the particle C axis.

APPENDIX B SUPPORTING INFORMATION FOR CHAPTER 3

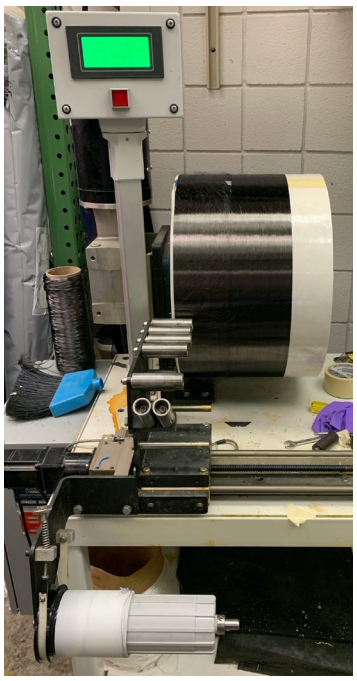

Figure B.1 Drum winding apparatus used to transfer and align hollow CF and IM7 fibers on the epoxy impregnated sheet.

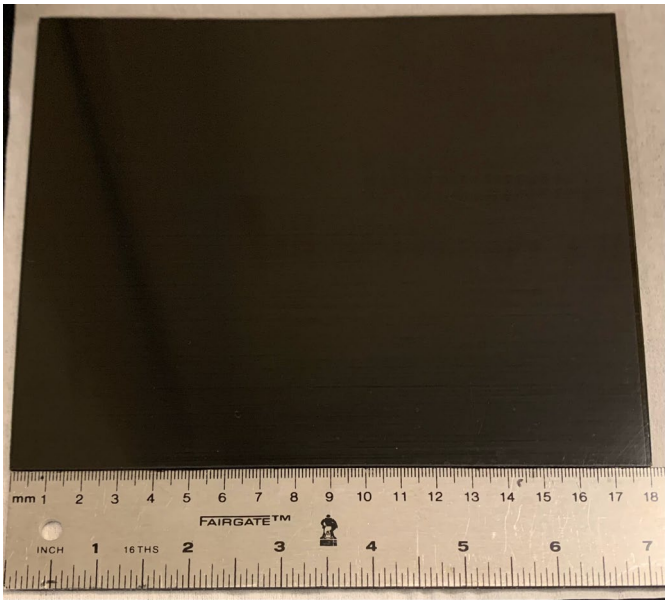

Figure B.2 6-ply unidirectional IM7 composite panel manufactured at University of Southern Mississippi.

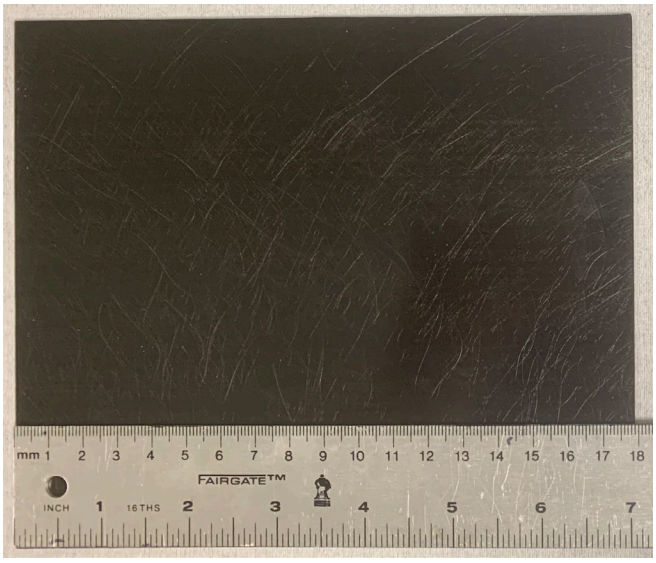

Figure B.3 6-ply unidirectional hollow CF composite panel manufactured at University of Southern Mississippi. The panel shows significantly higher number of misaligned fibers compared to the IM7 composite panel. This is due to the higher number of broken fibers in the hollow CF tow compares to the commercially produced IM7 fiber tow.

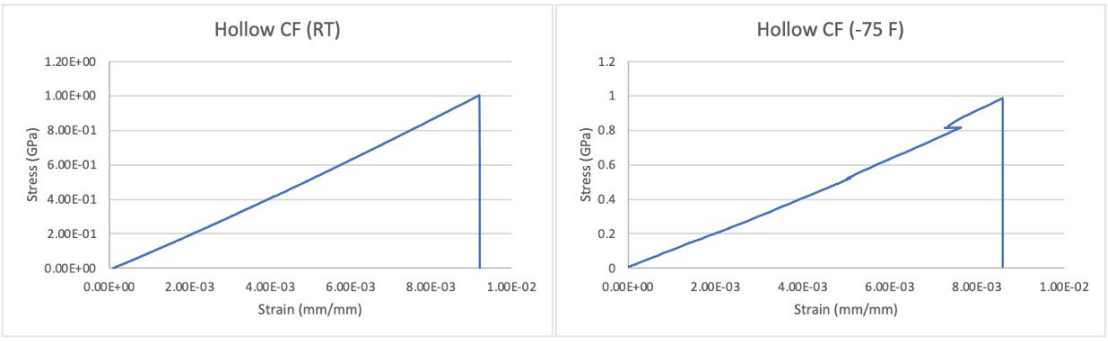

Figure B.4 Representative stress-strain plots for hollow CF specimen tension test at room temperature (left) and -75ºF.

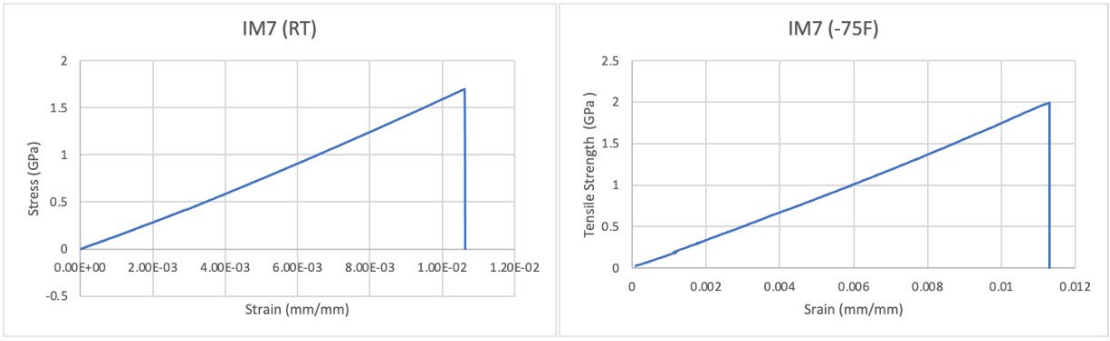

Figure B.5 Representative stress-strain plots for IM7 specimen tension test at room temperature (left) and -75ºF.

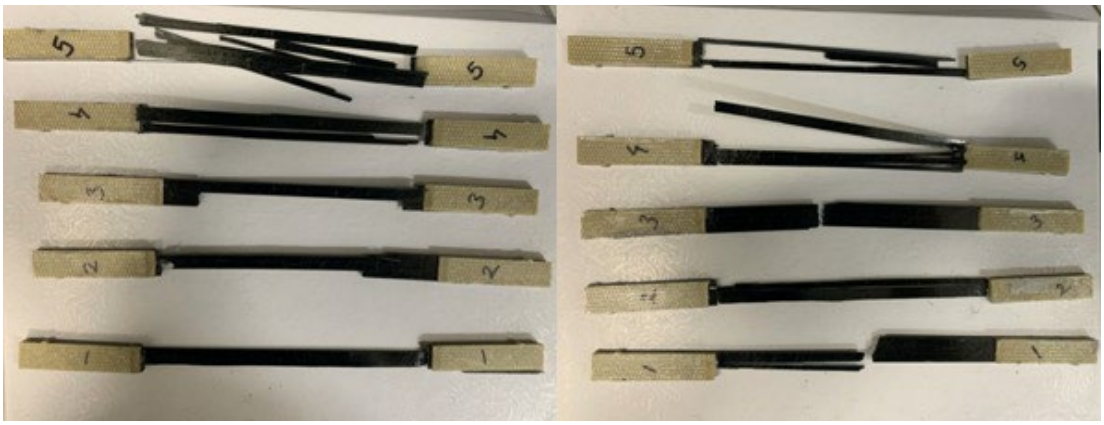

Figure B.6 Failed hollow CF composite specimen under tension at room temperature (left) and -75ºF (right). The failure mode per ASTM D3039 can be characterized as split-gauge length – middle (SGM) for both temperatures.

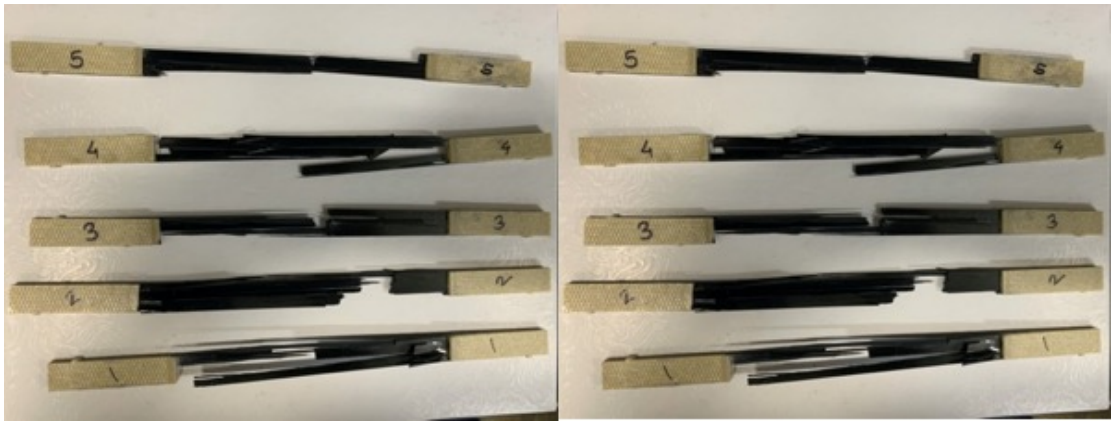

Figure B.7 Failed IM7 composite specimen under tension at room temperature (left) and -75ºF (right). The failure mode per ASTM D3039 can be characterized as split-gauge length – middle (SGM) for both temperatures.

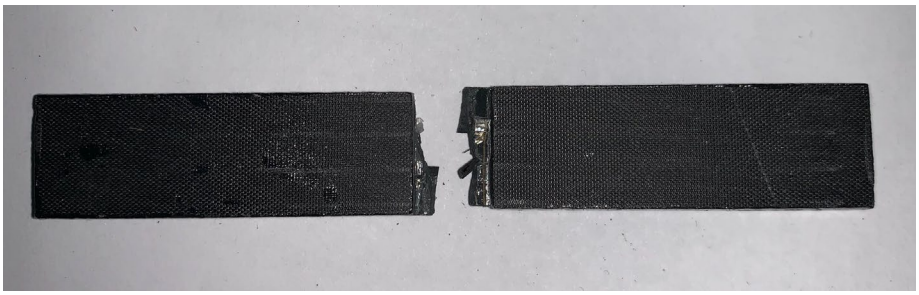

Figure B.8 Representative image of a failed hollow CF specimen under compression at room temperature. The specimen exhibits failure in the central gauge length region which is desirable.

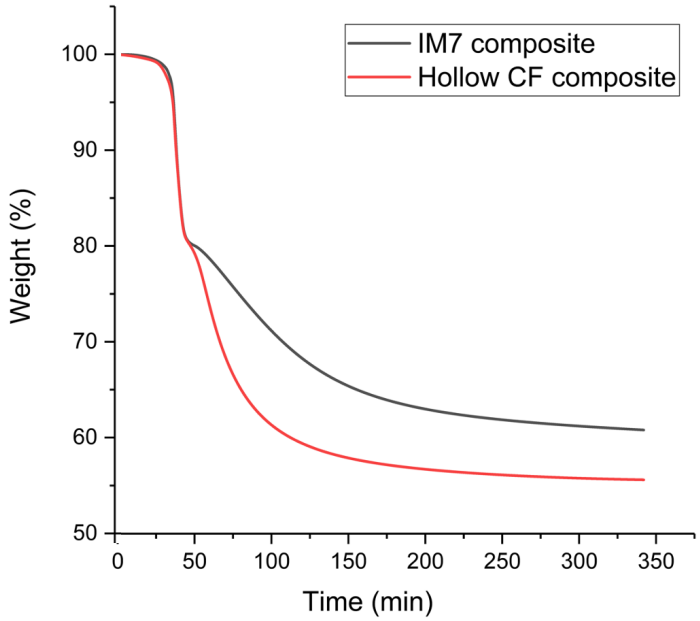

Figure B.9 TGA plots for fiber weight fraction measurement in hollow CF and IM7 composites.

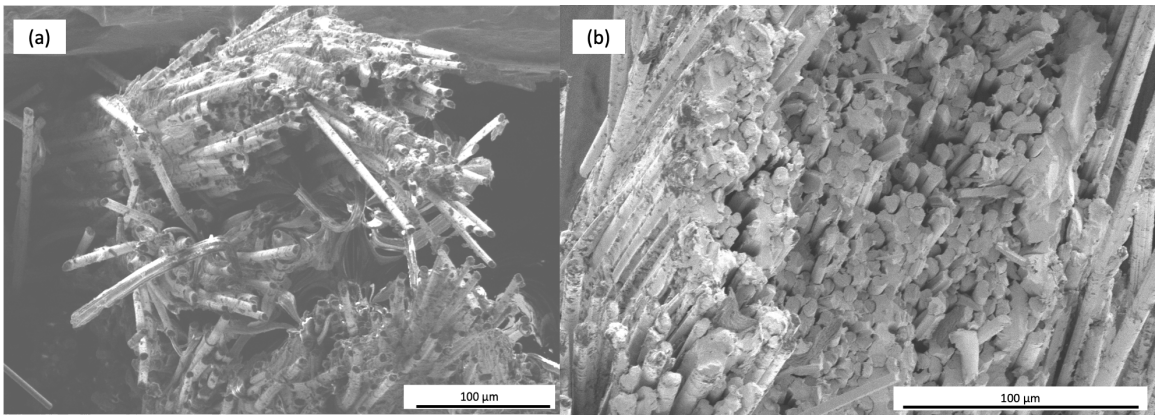

Figure B.10 SEM image of GT control carbon fiber composite fractured specimen after tension testing (a) The fracture can be characterized as explosive-gauge-middle (XGM) per ASTM D3039 (b) adhesion between the fibers and epoxy is better compared to the fiber-epoxy adhesion in hollow CF composites.

Table B.1 Weight-gain due to moisture pickup in IM7 composite specimen for compression testing after 14 days of hot-wet conditioning at 160 ºF.

Specimen	Weight before (g)	Weight after (g)	Gain (%)
1	1.73	1.75	1.2
2	1.72	1.74	1.2
3	1.73	1.75	1.2
4	1.73	1.75	1.2
5	1.72	1.74	1.2

Table B.2 Weight gain due to moisture pickup in hollow CF composite specimen for compression testing after 14 days of hot-wet conditioning at 160 ºF.

Specimen	Weight before (g)	Weight after (g)	Gain (%)
1	1.36	1.4	2.9
2	1.33	1.37	3.0
3	1.36	1.4	2.9
4	1.37	1.41	2.9
5	1.39	1.43	2.9

APPENDIX C SUPPORTING INFORMATION FOR CHAPTER 5

Table C.1 Carbon fiber manufacturing feature abbreviations

Abbreviation	Feature details
PAN wt	PAN molecular weight
CNT	CNT content in PAN fibers (wt%)
Spinning Geometry	Bicomponent or Single component geometry used for precursor fiber spinning
Coagulation bath	Number of coagulation baths used
Draw ratio	Total stretch ratio during precursor fiber manufacturing
Z1, Z2, Z3, Z4, Z5, Z6	Oxidation oven zones
LT	Low temperature carbonization furnace
HT	High temperature carbonization furnace
Time	Residence time
Temp	Temperature
Temp LT_1, Temp LT_2, Temp LT_3	Temperatures in LT carbonization furnace zone 1, zone 2, and zone 3
Cumulative oxidation Strain	Total applied strain in oxidation oven Z1 through Z6

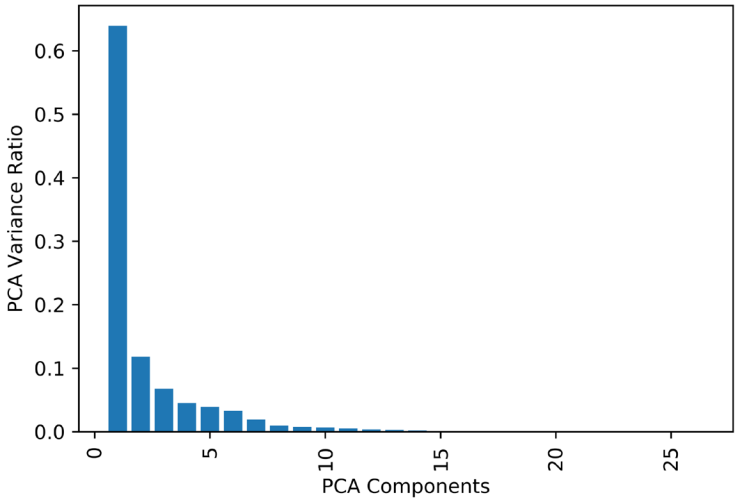

Figure C.1 Results of principal component analysis. Number of principal components n=14.

REFERENCES

1. www.hexcel.com/user_area/content_media/raw/IM7_HexTow_DataSheet.pdf.

2. Morgan P. Carbon Fibers and their Composites CRC Press. 2005.

3. https://www.torayca.com/en/download/pdf/torayca_t1100g.pdf

4. Kelly A, Macmillan NH. Strong Solids. Oxford University Press, Walton Street, Oxford OX 2 6 DP, UK, 1986. 1986.

5. Dumitrica T, Hua M, Yakobson BI. Symmetry-, time-, and temperature-dependent strength of carbon nanotubes. Proceedings of the National Academy of Sciences. 2006;103(16):6105.

6. Chae HG, Newcomb BA, Gulgunje PV, Liu Y, Gupta KK, Kamath MG, et al. High strength and high modulus carbon fibers. Carbon. 2015;93:81-7.

7. Boeing. http://www.boeing.com/commercial/aeromagazine/articles/qtr_4_06/article_04_2.html.

8. Airbus. http://www.airbus.com/aircraftfamilies/passengeraircraft/a350xwbfamily/a350-800/.

9. https://www.icao.int/environmental-protection/Carbonoffset/Pages/default.aspx.

10. Lee DS, Fahey DW, Skowron A, Allen MR, Burkhardt U, Chen Q, et al. The contribution of global aviation to anthropogenic climate forcing for 2000 to 2018. Atmospheric Environment. 2021;244:117834.

11. www.acs.org/content/acs/en/education/whatischemistry/landmarks/carbonfibers.html

12. Rahaman MSA, Ismail AF, Mustafa A. A review of heat treatment on polyacrylonitrile fiber. Polymer Degradation and Stability. 2007;92(8):1421-32.

13. Gupta AK, Paliwal DK, Bajaj P. Melting behavior of acrylonitrile polymers. Journal of Applied Polymer Science. 1998;70(13):2703-9.

14. Houtz RC. "Orlon" Acrylic Fiber: Chemistry and Properties. Textile Research Journal. 1950;20(11):786-801.

15. Chae HG. Polyacrylonitrile/carbon nanotube composite fibers: reinforcement efficiency and carbonization studies. 2008.

16. Bashir Z. A critical review of the stabilisation of polyacrylonitrile. Carbon. 1991;29(8):1081-90.

17. Smith P, Lemstra PJ. Ultra-high-strength polyethylene filaments by solution spinning/drawing. Journal of Materials Science. 1980;15(2):505-14.

18. Atureliya SK, Bashir Z. Continuous plasticized melt-extrusion of polyacrylonitrile homopolymer. Polymer. 1993;34(24):5116-22.

19. East GC, McIntyre JE, Patel GC. 20—THE DRY-JET WET-SPINNING OF AN ACRYLIC-FIBRE YARN. The Journal of The Textile Institute. 1984;75(3):196-200.

20. Capone GJ. Wet-spinning technology1995. 69-103 p.

21. Chae HG, Sreekumar TV, Uchida T, Kumar S. A comparison of reinforcement efficiency of various types of carbon nanotubes in polyacrylonitrile fiber. Polymer. 2005;46(24):10925-35.

22. Chae HG, Kumar S. Making Strong Fibers. Science. 2008;319(5865):908.

23. Huang J, Baird DG, Loos AC, Rangarajan P, Powell A. Filament winding of bicomponent fibers consisting of polypropylene and a liquid crystalline polymer. Composites Part A: Applied Science and Manufacturing. 2001;32(8):1013-20.

24. Cho HH, Kim KH, Kang YA, Ito H, Kikutani T. Fine structure and physical properties of polyethylene/poly(ethylene terephthalate) bicomponent fibers in high-speed spinning. I. Polyethylene sheath/poly(ethylene terephthalate) core fibers. Journal of Applied Polymer Science. 2000;77(10):2254-66.

25. Godshall D, White C, Wilkes GL. Effect of compatibilizer molecular weight and maleic anhydride content on interfacial adhesion of polypropylene–PA6 bicomponent fibers. Journal of Applied Polymer Science. 2001;80(2):130-41.

26. Chien A-T, Gulgunje PV, Chae HG, Joshi AS, Moon J, Feng B, et al. Functional polymer–polymer/carbon nanotube bi-component fibers. Polymer. 2013;54(22):6210-7.

27. Chae HG, Choi YH, Minus ML, Kumar S. Carbon nanotube reinforced small diameter polyacrylonitrile based carbon fiber. Composites Science and Technology. 2009;69(3):406-13.

28. Korobeinichev OP, Paletsky AA, Gonchikzhapov MB, Glaznev RK, Gerasimov IE, Naganovsky YK, et al. Kinetics of thermal decomposition of PMMA at different heating rates and in a wide temperature range. Thermochimica Acta. 2019;671:17-25.

29. Gulgunje P, Newcomb B, Gupta K, Chae H, Tsotsis T, Kumar S. Low-density and high-modulus carbon fibers from polyacrylonitrile with honeycomb structure2015.

30. Qin Sun C, Zhang D, Liu Y, Xiao R. Preliminary study on fiber splitting of bicomponent meltblown fibers2004. 2090-4 p.

31. Thunwall M, Kuthanová V, Boldizar A, Rigdahl M. Film blowing of thermoplastic starch. Carbohydrate Polymers. 2008;71(4):583-90.

32. Han CD, Park JY. Studies on blown film extrusion. II. Analysis of the deformation and heat transfer processes. Journal of Applied Polymer Science. 1975;19(12):3277-90.

33. Kanai T, White JL. Kinematics, dynamics and stability of the tubular film extrusion of various polyethylenes. Polymer Engineering & Science. 1984;24(15):1185-201.

34. Frank CW, Rao V, Despotopoulou MM, Pease RFW, Hinsberg WD, Miller RD, et al. Structure in thin and ultrathin spin-cast polymer films. Science. 1996;273(5277):912-5.

35. Guo H, Minus ML, Jagannathan S, Kumar S. Polyacrylonitrile/carbon nanotube composite films. ACS applied materials & interfaces. 2010;2(5):1331-42.

36. Koganemaru A, Bin Y, Tohora H, Okino F, Komiyama S, Zhu J, et al. Carbonization of oriented polyacrylonitrile and multiwalled carbon nanotube composite films. Asia-Pacific Journal of Chemical Engineering. 2008;3(5):521-6.

37. Luo J, Chang H, Wang P-H, Moon RJ, Kumar S. Cellulose nanocrystals effect on the stabilization of polyacrylonitrile composite films. Carbon. 2018;134:92-102.

38. Yabu H, Shimomura M. Single-step fabrication of transparent superhydrophobic porous polymer films. Chemistry of materials. 2005;17(21):5231-4.

39. Xu J, Liu C, Hsu P-C, Liu K, Zhang R, Liu Y, et al. Roll-to-Roll Transfer of Electrospun Nanofiber Film for High-Efficiency Transparent Air Filter. Nano Letters. 2016;16(2):1270-5.

40. Pang J, Kong H, He J-H. PVA-based nanographene film by electrospinning. Thermal Science. 2013;17(5):1449-52.

41. Wang Y, Yang Q, Shan G, Wang C, Du J, Wang S, et al. Preparation of silver nanoparticles dispersed in polyacrylonitrile nanofiber film spun by electrospinning. Materials Letters. 2005;59(24-25):3046-9.

42. Hungerford GP. Method of making polymeric acrylonitrile films. 1976(US4066731A).

43. Edison TA. 1879(U.S. Patent 223,898).

44. Bacon R. Growth, Structure, and Properties of Graphite Whiskers. Journal of Applied Physics. 1960;31(2):283-90.

45. Shindo A. Tanso sen'i no kenkyu—netsu shori ni tomonau kesshoshi no seicho (Study of carbon fiber—Growth of crytallite in heat treatment). Osaka Kogyo Gijutsu Shikenjo Kiho (GIRIO Seasonal Report). 1961;12(2):110-8.

46. Minus M, Kumar S. The processing, properties, and structure of carbon fibers. JOM. 2005;57(2):52-8.

47. Ouyang Q, Cheng L, Wang H, Li K. DSC study of stabilization reactions in poly (acrylonitrile-co-itaconic acid) with peak-resolving method. Journal of Thermal Analysis and Calorimetry. 2008;94(1):85-8.

48. Gupta AK, Paliwal DK, Bajaj P. Effect of the nature and mole fraction of acidic comonomer on the stabilization of polyacrylonitrile. Journal of applied polymer science. 1996;59(12):1819-26.

49. Gupta AK, Paliwal DK, Bajaj P. Effect of an acidic comonomer on thermooxidative stabilization of polyacrylonitrile. Journal of applied polymer science. 1995;58(7):1161-74.

50. Shimada I, Takahagi T, Fukuhara M, Morita K, Ishitani A. FT-IR study of the stabilization reaction of polyacrylonitrile in the production of carbon fibers. Journal of Polymer Science Part A: Polymer Chemistry. 1986;24(8):1989-95.

51. Godshall D, Rangarajan P, Baird DG, Wilkes GL, Bhanu VA, McGrath JE. Incorporation of methyl acrylate in acrylonitrile based copolymers: effects on melting behavior. Polymer. 2003;44(15):4221-8.

52. Morris EA, Weisenberger MC, Bradley SB, Abdallah MG, Mecham SJ, Pisipati P, et al. Synthesis, spinning, and properties of very high molecular weight poly (acrylonitrile-co-methyl acrylate) for high performance precursors for carbon fiber. Polymer. 2014;55(25):6471-82.

53. Singcharoen K, Sirimongkol W, Khuntong S, Rangkupan R, editors. Fabrication and Stabilization of Poly (Acrylonitrile-co-Methyl Acrylate) Nanofibers2018: Trans Tech Publ.

54. Kakida H, Tashiro K. Mechanism and Kinetics of Stabilization Reaction of Polyacrylonitrile and Related Copolymers II. Relationships between Isothermal DSC Thermograms and FT-IR Spectral Changes of Polyacrylonitrile in Comparison with the Case of Acrylonitrile/Methacrylic Acid Copolymer. Polymer journal. 1997;29(4):353.

55. Kakida H, Tashiro K, Kobayashi M. Mechanism and kinetics of stabilization reaction of polyacrylonitrile and related copolymers I. Relationship between isothermal DSC thermogram and FT/IR spectral change of an acrylonitrile/methacrylic acid copolymer. Polymer journal. 1996;28(1):30.

56. Liu Y, Chae HG, Kumar S. Gel-spun carbon nanotubes/polyacrylonitrile composite fibers. Part II: Stabilization reaction kinetics and effect of gas environment. Carbon. 2011;49(13):4477-86.

57. Gupta AK, Paliwal DK, Bajaj P. Acrylic Precursors for Carbon Fibers. Journal of Macromolecular Science, Part C. 1991;31(1):1-89.

58. Lu M, Xu J, Arias-Monje PJ, Gulgunje PV, Gupta K, Shirolkar N, et al. Continuous stabilization of polyacrylonitrile (PAN) - carbon nanotube (CNT) fibers by Joule heating. Chemical Engineering Science. 2021;236:116495.

59. Liu J, Xiao S, Shen Z, Xu L, Zhang L, Peng J. Study on the oxidative stabilization of polyacrylonitrile fibers by microwave heating. Polymer Degradation and Stability. 2018;150:86-91.

60. Park S, Kil H-S, Choi D, Song S-K, Lee S. Rapid stabilization of polyacrylonitrile fibers achieved by plasma-assisted thermal treatment on electron-beam irradiated fibers. Journal of Industrial and Engineering Chemistry. 2019;69:449-54.

61. Paulauskas FL, Bigelow TS, Yarborough KD, Meek TT. Manufacturing of carbon fibers using microwave-assisted plasma technology. SAE transactions. 2000:799-811.

62. White TL, Paulauskas FL, Bigelow TS. System to continuously produce carbon fiber via microwave assisted plasma processing. Google Patents; 2010.

63. Fitzer E, Frohs W, Heine M. Optimization of stabilization and carbonization treatment of PAN fibres and structural characterization of the resulting carbon fibres. Carbon. 1986;24(4):387-95.

64. Chang H, Lu M, Luo J, Park JG, Liang R, Park C, et al. Polyacrylonitrile/boron nitride nanotubes composite precursor and carbon fibers. Carbon. 2019;147:419-26.

65. Chang H, Luo J, Gulgunje PV, Kumar S. Structural and Functional Fibers. Annual Review of Materials Research. 2017;47(1):331-59.

66. Kinloch IA, Suhr J, Lou J, Young RJ, Ajayan PM. Composites with carbon nanotubes and graphene: An outlook. Science. 2018;362(6414):547.

67. Liu Y, Kumar S. Polymer/Carbon Nanotube Nano Composite Fibers–A Review. ACS Applied Materials & Interfaces. 2014;6(9):6069-87.

68. Thomas Tsotsis JH. Process of making a continuous, multicellular, hollow carbon fiber. 2009(8337730B2).

69. Lyons KM, Newcomb BA, McDonald KJ, Chae HG, Kumar S. Development of single filament testing procedure for polyacrylonitrile precursor and polyacrylonitrile-based carbon fibers. Journal of Composite Materials. 2014;49(18):2231-40.

70. Cullity BD. Elements of X-ray Diffraction. Addison-Wesley Publishing; 1956.

71. Sreekumar TV, Liu T, Min BG, Guo H, Kumar S, Hauge RH, et al. Polyacrylonitrile Single-Walled Carbon Nanotube Composite Fibers. Advanced Materials. 2004;16(1):58-61.

72. ASTM International. D4018-17 Standard Test Methods for Properties of Continuous Filament Carbon and Graphite Fiber Tows. West Conshohocken, PA; ASTM International, 2017.

73. Doucet M, Cho JH, Alina G, Bakker J, Bouwman W, Butler P. SasView version 4.2.2. Zenodo. 2019.

74. Newcomb BA, Gulgunje PV, Gupta K, Kamath MG, Liu Y, Giannuzzi LA, et al. Processing, structure, and properties of gel spun PAN and PAN/CNT fibers and gel spun PAN based carbon fibers. Polymer Engineering & Science. 2015;55(11):2603-14.

75. T300 T. https://www.toraycma.com/file_viewer.php?id=5106

76. Whitney W, Kimmel RM. Griffith Equation and Carbon Fibre Strength. Nature Physical Science. 1972;237:93.

77. Thünemann AF, Ruland W. Microvoids in Polyacrylonitrile Fibers: A Small-Angle X-ray Scattering Study. Macromolecules. 2000;33(5):1848-52.

78. Takaku A, Shioya M. Characterization of microvoids in polyacrylonitrile-based carbon fibres. Journal of Materials Science. 1986;21(12):4443-50.

79. Higgins JS, Benoit HC. Polymers and neutron scattering. 1994.

80. Ferriol M, Gentilhomme A, Cochez M, Oget N, Mieloszynski JL. Thermal degradation of poly(methyl methacrylate) (PMMA): modelling of DTG and TG curves. Polymer Degradation and Stability. 2003;79(2):271-81.

81. Copyright. In: Mallick PK, editor. Materials, Design and Manufacturing for Lightweight Vehicles: Woodhead Publishing; 2010. p. iv.

82. Lee SH, Waas AM. Compressive response and failure of fiber reinforced unidirectional composites. International Journal of Fracture. 1999;100(3):275-306.

83. Ohsawa T, Miwa M, Kawade M, Tsushima E. Axial compressive strength of carbon fiber. Journal of Applied Polymer Science. 1990;39(8):1733-43.

84. https://www.solvay.com/en/product/cycom-977-3.

85. ASTM D3039. Standard Test Method for Tensile Properties of Polymer Matrix Composite Materials. ASTM International. 2017.

86. ASTM D695-15, Standard Test Method for Compressive Properties of Rigid Plastics. ASTM International. 2015.

87. Naraghi M, Chawla S. Carbonized Micro- and Nanostructures: Can Downsizing Really Help? Materials. 2014;7(5).

88. Ozkan T, Naraghi M, Chasiotis I. Mechanical properties of vapor grown carbon nanofibers. Carbon. 2010;48(1):239-44.

89. Papkov D, Zou Y, Andalib MN, Goponenko A, Cheng SZD, Dzenis YA. Simultaneously Strong and Tough Ultrafine Continuous Nanofibers. ACS Nano. 2013;7(4):3324-31.

90. Morris EA, Weisenberger MC, Abdallah MG, Vautard F, Grappe H, Ozcan S, et al. High performance carbon fibers from very high molecular weight polyacrylonitrile precursors. Carbon. 2016;101:245-52.

91. Naito K. Stress analysis and fracture toughness of notched polyacrylonitrile (PAN)-based and pitch-based single carbon fibers. Carbon. 2018;126:346-59.

92. Arshad SN, Naraghi M, Chasiotis I. Strong carbon nanofibers from electrospun polyacrylonitrile. Carbon. 2011;49(5):1710-9.

93. Kong LQ, Liu H, Cao WY, Xu LH. PAN fiber diameter effect on the structure of PAN-based carbon fibers. Fiber Polym. 2014;15(12):2480-8.

94. http://www.hillsinc.net/assets/pdfs/production-submicron.pdf.

95. Wei M, Kang B, Sung C, Mead J. Core-Sheath Structure in Electrospun Nanofibers from Polymer Blends. Macromolecular Materials and Engineering. 2006;291(11):1307-14.

96. Naeimirad M, Zadhoush A, Kotek R, Esmaeely Neisiany R, Nouri Khorasani S, Ramakrishna S. Recent advances in core/shell bicomponent fibers and nanofibers: A review. Journal of Applied Polymer Science. 2018;135(21):46265.

97. https://www.toraycma.com/file_viewer.php?id=5126.

98. Ayad E, Cayla A, Rault F, Gonthier A, Campagne C, Devaux E. Effect of Viscosity Ratio of Two Immiscible Polymers on Morphology in Bicomponent Melt Spinning Fibers. Advances in Polymer Technology. 2018;37(4):1134-41.

99. Shirasu K, Nagai C, Naito K. Mechanical anisotropy of PAN-based and pitch-based carbon fibers. Mechanical Engineering Journal. 2020;7(4):19-00599-19-.

100. Qian X, Wang X, Zhong J, Zhi J, Heng F, Zhang Y, et al. Effect of fiber microstructure studied by Raman spectroscopy upon the mechanical properties of carbon fibers. Journal of Raman Spectroscopy. 2019;50(5):665-73.

101. Liu R, Kumar A, Chen Z, Agrawal A, Sundararaghavan V, Choudhary A. A predictive machine learning approach for microstructure optimization and materials design. Scientific Reports. 2015;5(1):11551.

102. Fujimura K, Seko A, Koyama Y, Kuwabara A, Kishida I, Shitara K, et al. Accelerated Materials Design of Lithium Superionic Conductors Based on First-Principles Calculations and Machine Learning Algorithms. Advanced Energy Materials. 2013;3(8):980-5.

103. Wen C, Zhang Y, Wang C, Xue D, Bai Y, Antonov S, et al. Machine learning assisted design of high entropy alloys with desired property. Acta Materialia. 2019;170:109-17.

104. Qi Z, Zhang N, Liu Y, Chen W. Prediction of mechanical properties of carbon fiber based on cross-scale FEM and machine learning. Composite Structures. 2019;212:199-206.

105. Xiao C, Hao K, Ding Y. The Bi-Directional Prediction of Carbon Fiber Production Using a Combination of Improved Particle Swarm Optimization and Support Vector Machine. Materials. 2015;8(1):117-36.

106. Chen J, Ding Y, Hao K. The Bidirectional Optimization of Carbon Fiber Production by Neural Network with a GA-IPSO Hybrid Algorithm. Mathematical Problems in Engineering. 2013;2013:16.

107. Khayyam H, Fakhrhoseini SM, Church JS, Milani AS, Bab-Hadiashar A, Jazar RN, et al. Predictive modelling and optimization of carbon fiber mechanical properties through high temperature furnace. Applied Thermal Engineering. 2017;125:1539-54.

108. Khayyam H, Naebe M, Zabihi O, Zamani R, Atkiss S, Fox B. Dynamic Prediction Models and Optimization of Polyacrylonitrile (PAN) Stabilization Processes for Production of Carbon Fiber. IEEE Transactions on Industrial Informatics. 2015;11(4):887-96.

109. Golkarnarenji G, Naebe M, Badii K, Milani AS, Jazar RN, Khayyam H. A machine learning case study with limited data for prediction of carbon fiber mechanical properties. Computers in Industry. 2019;105:123-32.

110. Golkarnarenji G, Naebe M, Badii K, Milani AS, Jazar RN, Khayyam H. Production of Low Cost Carbon-Fiber through Energy Optimization of Stabilization Process. Materials. 2018;11(3):385.

111. Golkarnarenji G, Naebe M, Badii K, Milani AS, Jazar RN, Khayyam H. Support vector regression modelling and optimization of energy consumption in carbon fiber production line. Comput Chem Eng. 2018;109:276-88.

112. Golkarnarenji G, Naebe M, Badii K, Milani AS, Jamali A, Bab-hadiashar A, et al. Multi-Objective Optimization of Manufacturing Process in Carbon Fiber Industry Using Artificial Intelligence Techniques. IEEE Access. 2019;7:67576-88.

113. Pruksawan S, Lambard G, Samitsu S, Sodeyama K, Naito M. Prediction and optimization of epoxy adhesive strength from a small dataset through active learning. Science and Technology of Advanced Materials. 2019;20(1):1010-21.

114. Zhao M, Li Z, He W. Classifying Four Carbon Fiber Fabrics via Machine Learning: A Comparative Study Using ANNs and SVM. Applied Sciences. 2016;6(8):209.

115. Keogh E, Mueen A. Curse of Dimensionality. In: Sammut C, Webb GI, editors. Encyclopedia of Machine Learning and Data Mining. Boston, MA: Springer US; 2017. p. 314-5.

116. Dubitzky W, Wolkenhauer, Olaf, Yokota, Hiroki, Cho, Kwang-Hyun. Encyclopedia of systems biology: Springer Publishing Company; 2013.

117. Pedregosa F, Varoquaux G, Gramfort A, Michel V, Thirion B, Grisel O, et al. Scikit-learn: Machine learning in Python. Journal of Machine Learning Research. 2011;12:2825-30.

118. Cortes C, Vapnik V. Support-vector networks. Machine Learning. 1995;20(3):273-97.

119. Awad M, Khanna R. Support Vector Regression. In: Awad M, Khanna R, editors. Efficient Learning Machines: Theories, Concepts, and Applications for Engineers and System Designers. Berkeley, CA: Apress; 2015. p. 67-80.

120. https://www.mathworks.com/help/stats/understanding-support-vector-machine-regression.html.

121. https://scikit-learn.org/stable/modules/generated/sklearn.svm.svr.html.

122. Chen T, Guestrin C. XGBoost: A Scalable Tree Boosting System. Proceedings of the 22nd ACM SIGKDD International Conference on Knowledge Discovery and Data Mining; San Francisco, California, USA: Association for Computing Machinery; 2016. p. 785–94.

123. Aitkin M, Foxall R. Statistical modelling of artificial neural networks using the multi-layer perceptron. Statistics and Computing. 2003;13(3):227-39.

124. Nielsen MA. Neural networks and deep learning: Determination press San Francisco, CA; 2015.

125. https://keras.io.

126. Hochreiter S, Schmidhuber J. Long Short-Term Memory. Neural Computation. 1997;9(8):1735-80.

127. Chung J, Gulcehre C, Cho K, Bengio Y. Empirical evaluation of gated recurrent neural networks on sequence modeling. arXiv preprint arXiv:14123555. 2014.